Microglia dysfunction caused by the loss of Rhoa disrupts neuronal physiology and leads to neurodegeneration

Renato Socodato[1,*], Camila C. Portugal[1,*], Teresa Canedo[2,11], Artur Rodrigues[1], Joana F. Henriques[2], Sandra H. Vaz[8,9], João Magalhães[2], Cátia M. Silva[1], Filipa I. Baptista[3], Renata L. Alves[2,6], Vanessa Coelho-Santos[4], Ana Paula Silva[4], Roberto Paes-de-Carvalho[5], Ana Magalhães[2], Cord Brakebusch[7], Ana M. Sebastião[8,9], Teresa Summavielle[2,10,11], António F. Ambrósio[3] and João B. Relvas[1,11, 12 #]

[1]Glial Cell Biology Lab, Instituto de Investigação e Inovação em Saúde and Instituto de Biologia Molecular e Celular, Universidade do Porto, Porto, Portugal.

[2]Addiction Biology Lab, Instituto de Investigação e Inovação em Saúde and Instituto de Biologia Molecular e Celular, Universidade do Porto, Porto, Portugal.

[3]Retinal Dysfunction and Neuroinflammation Lab, Coimbra Institute for Clinical and Biomedical Research (iCBR), Faculty of Medicine, University of Coimbra, Coimbra, Portugal.

[4]Institute of Pharmacology and Experimental Therapeutics, Faculty of Medicine, University of Coimbra, Coimbra, Portugal.

[5]Department of Neurobiology and Program of Neurosciences, Institute of Biology, Fluminense Federal University, Niterói, Brazil.

[6]Faculty of Psychology and Education Sciences, University of Porto, Porto, Portugal.

[7]Molecular Pathology Section, BRIC, Københavns Biocenter, Copenhagen, Denmark.

[8]Instituto de Farmacologia e Neurociências, Faculdade de Medicina, Universidade de Lisboa, Lisboa, Portugal.

[9]Instituto de Medicina Molecular, Faculdade de Medicina, Universidade de Lisboa, Lisboa, Portugal.

[10]Escola Superior de Saúde, Politécnico do Porto, Porto, Portugal

[11]The Discoveries Centre for Regeneration and Precision Medicine, Porto Campus, Porto, Portugal

[12]Faculdade de Medicina, Universidade do Porto (FMUP), Porto, Portugal

#Corresponding author: João Bettencourt Relvas (jbrelvas@ibmc.up.pt)

*Renato Socodato and Camila C. Portugal contributed equally to this manuscript.

Abstract

Nervous tissue homeostasis requires regulation of microglia activity. Using conditional gene targeting in mice, we demonstrate that genetic ablation of the small GTPase Rhoa in adult microglia is sufficient to trigger spontaneous microglia activation causing synapse and neuron loss, impairment of long-term synaptic plasticity, deficits in recognition memory and the formation of beta-amyloid plaques. We found that Rhoa function sustains Csk negative regulation of Src activity, and that its loss elicited microglia activation via Src-mediated Tnf production, leading to excitotoxic glutamate release. Inhibiting Src in microglia Rhoa-deficient mice attenuates microglia activity and the ensuing neurological phenotype. Attesting the importance of Rhoa/Csk/Src signaling in restraining microglia activity, we found that this pathway was affected in microglia of the APP/PS1 mouse model of Alzheimer´s disease. Inhibiting Src in these mice limited microglia dysregulation, decreasing amyloid burden and synapse loss. Our results indicate that disturbing RhoGTPase signaling in microglia can directly cause neurodegeneration.

Keywords: Microglia, RhoGTPase, LTP, memory, Src, Alzheimer´s disease

Introduction

Microglia are yolk sack-derived myeloid cells that populate the early-developing nervous system (Ginhoux et al., 2010, Kierdorf et al., 2013, Schulz et al., 2012). These cells constitute a cell autonomous population, ontologically and transcriptomically distinct from other tissue-resident myeloid cells and circulating monocytes (Ginhoux and Guilliams, 2016). Under physiological conditions, microglia continuously extend and retract their cellular processes, monitoring the central nervous system (CNS) parenchyma for tissue damage or infections and checking the functional status of brain synapses (Crotti and Ransohoff, 2016). Following CNS tissue damage or infection, microglia change their morphology into a more amoeboid shape and function as innate immune cells clearing cell debris and restoring tissue homeostasis (Crotti and Ransohoff, 2016).

Although attempting to repair injuries to the parenchyma, exacerbation or prolonged microglial activation may trigger/accelerate neuronal damage in neurogenerative conditions or delay CNS recovery after insults (Gomez-Nicola et al., 2013, Rice et al., 2015, Spangenberg et al., 2016). Such detrimental role for microglia can be attributed to the loss/disruption of microglia immune restrain mechanisms (Deczkowska et al., 2018), which leads to sustained deregulation of their activation and consequent overproduction of proinflammatory cytokines (IL-1β and Tnf), nitric oxide (NO), reactive oxygen species (ROS) and increased release of glutamate (Block et al., 2007).

Dynamic reorganization of the cytoskeleton is likely to underlie microglial function(s) in steady state and during activation. In line with this, proinflammatory microglial activation is associated with profound changes in microglia morphology requiring cytoskeleton reorganization (abd-el-Basset and Fedoroff, 1995, Kaur, 1997). The GTPases of the Rho family, from which Rhoa, Rac1 and Cdc42 are the founding members, are key orchestrators of cytoskeleton dynamics (Bustelo et al., 2007) and are

therefore well positioned to govern microglia activation. Typical GTPases function as binary switches by cycling between a GDP-bound inactive, “off” state, and a GTP-bound active, “on” state, in which they can directly interact with downstream effectors to regulate different cell functions (Hodge and Ridley, 2016, Bustelo et al., 2007, Ridley, 2015). Although the molecular design of the RhoGTPase switch is relatively simple, its spatiotemporal activity is tightly controlled by regulatory proteins (Hodge and Ridley, 2016). RhoGTPases play important roles during CNS development and dysregulation of their expression and/or activity is associated with different neurological disorders (DeGeer and Lamarche-Vane, 2013, Govek et al., 2005, Stankiewicz and Linseman, 2014). Indeed, changes in Rhoa activity or in the activities of its effectors are implicated in several neurodegenerative conditions, including stroke, Alzheimer´s and Parkinson´s Disease and amyotrophic lateral sclerosis (DeGeer and Lamarche-Vane, 2013, Droppelmann et al., 2014). Here, using tamoxifen-inducible conditional gene inactivation in mice, we investigated for the first time the *bona fide* function of Rhoa in microglia. Our data reveal novel and critical roles for Rhoa signaling in regulating microglia immune activity and microglial regulation of synaptic integrity.

Results

Conditional ablation of Rhoa in adult microglia

To study the role of Rhoa in adult microglia, we generated conditional mice by crossing Cx3cr1$^{CreER\text{-}IRES\text{-}EYFP}$ mice (Parkhurst et al., 2013, Goldmann et al., 2013, Yona et al., 2013) with mice carrying Rhoa conditional alleles (Herzog et al., 2011, Jackson et al., 2011) (**Suppl. Fig. 1A**). In Cx3cr1^{CreER} mice, the CreER-IRES-EYFP transgene is transcriptionally active in Iba1-positive brain myeloid cells (Goldmann et al., 2016) (**Suppl. Fig. 1B**), and in microglia (**Suppl. Fig. 1C**).

Following tamoxifen administration Cre translocates to the nucleus inducing Rhoa gene inactivation in Rhoa$^{fl/fl}$:Cx3cr1^{CreER+} mice. Thus, to investigate the *bona fide* function of Rhoa in adult microglia, we administered tamoxifen by oral gavage to control Rhoa$^{fl/fl}$ and to Rhoa$^{fl/fl}$:Cx3cr1^{CreER+} mice between P28-P30 and analyzed their brains 35-45 (P65-75; young adult) or 150-160 (P180-190; mature adult) days later. Analysis by flow cytometry and Western blotting on MACS-separated microglia revealed substantial decrease of Rhoa protein in microglia obtained from Rhoa$^{fl/fl}$:Cx3cr1^{CreER+} mice compared with that in microglia obtained from control Rhoa$^{fl/fl}$ littermates (**Fig. 1A and Suppl. Fig. 1D**).

Because Rhoa$^{fl/fl}$:Cx3cr1^{CreER+} mice have only one intact copy of Cx3cr1, and decreased Cx3cr1 protein levels could *per se* disrupt microglia homeostasis and be a confounding factor affecting the conclusions of our study, we confirmed that the number of microglia expressing Cxc3r1 as well as microglial number did not vary significantly between Rhoa$^{fl/fl}$ and Cx3cr1^{CreER+}(**Suppl. Fig 2A**). These observations were in line with previously published work using Cx3cr1^{GFP+} mice (Jung et al., 2000). We also included other controls to further validate our experimental set up (**Suppl. Fig 2B-D**).

Rhoa is required for microglial survival and its deficiency triggers spontaneous microglia activation

We then evaluated the requirement of Rhoa for microglia physiology in the adult brain at the steady state. Using Iba1 immunohistochemistry we observed a decrease in the number of Iba1^{+} cells in different brain regions, including the neocortex, hippocampus and striatum, comparing Rhoa$^{fl/fl}$ with Rhoa$^{fl/fl}$:Cx3cr1^{CreER+} littermates (**Fig. 1B**). Confirming the immunohistochemistry data, we observed, using flow cytometry, a decrease in the numbers and in the frequency of microglia in the brains of Rhoa$^{fl/fl}$:Cx3cr1^{CreER+} mice relative to Rhoa$^{fl/fl}$ littermates (**Fig. 1C**). Such decrease in microglial numbers persisted in brains of mature adult Rhoa$^{fl/fl}$:Cx3cr1^{CreER+} mice (**Suppl. Fig. 3A**). The decrease on microglial numbers following Rhoa ablation could be caused by increased microglial cell death. To address this possibility, we evaluated microglia necrosis and apoptosis, using the viability dye Zombie and the apoptotic marker Annexin V (AnV), by flow cytometry. We found increased necrosis (Zombie^{+}Anv^{-}) in microglia from Rhoa$^{fl/fl}$:Cx3cr1^{CreER+} mice compared with microglia from Rhoa$^{fl/fl}$ littermates (**Fig. 1D**) and also in microglia from mature Rhoa$^{fl/fl}$:Cx3cr1^{CreER+} mice. However, the total numbers of microglia obtained from Rhoa$^{fl/fl}$:Cx3cr1^{CreER+} mice 40 days post-TAM (**Fig. 1C**) and 150 days post-TAM (**Suppl. Fig. 3A**) were not significantly different. This suggested that proliferation could be counterbalancing cell death to stabilize microglial numbers. Accordingly, we found increased microglial proliferation in mature Rhoa$^{fl/fl}$:Cx3cr1^{CreER+} mice compared with Rhoa$^{fl/fl}$ littermates (**Suppl. Fig. 3B**). Collectively, these data suggest that the decreased microglial numbers found in Rhoa$^{fl/fl}$:Cx3cr1^{CreER+} brain was a consequence of increased microglial cell death.

Changes in microglial cell morphology are usually concurrent with alterations in microglial function in the adult brain. Morphological analysis with Iba1

immunohistochemistry on tissue sections obtained from the neocortex of control Rhoa$^{fl/fl}$ and Rhoa$^{fl/fl}$:Cx3cr1^{CreER+} littermate mice revealed that Rhoa mutant Iba1^{+} microglia were less ramified than Rhoa$^{fl/fl}$ microglia (**Fig. 1E and Suppl. Fig. 3C**). Modifications in actin cytoskeleton organization and dynamics most likely underlie the changes found in microglia morphology. Accordingly, inhibiting Rhoa activation in microglial cultures by means of expressing a dominant negative Rhoa mutant (Rhoa^{T19N}; **Suppl. Fig. 3D),** resulted in loss of actin stress fibers (**Suppl. Fig. 3E)** and decreased the speed of microglia protrusion extension, which like in cell migration, is regulated by actin cytoskeleton dynamics (**Suppl. Fig. 3F)**.

Disrupting microglia homeostasis may lead to loss of immune restrain mechanisms (Deczkowska et al., 2018) resulting in spontaneous and/or exacerbation of microglia activation. Thus, we evaluated whether production of inflammatory cytokines was increased in Rhoa$^{fl/fl}$:Cx3cr1^{CreER+} microglia. Indeed, qRT-PCR analysis of microglia sorted from the brains of Rhoa$^{fl/fl}$:Cx3cr1^{CreER+} mice and Rhoa$^{fl/fl}$ littermates revealed that Rhoa$^{fl/fl}$:Cx3cr1^{CreER+} microglia contained higher amounts of mRNA transcripts coding for the classical proinflammatory cytokines Tnf and IL-1β, but not for IL-6, compared with Rhoa$^{fl/fl}$ microglia (**Fig. 1F**). The increased production of Tnf in microglia following Rhoa ablation resulted in increased Tnf amounts in the brains of Rhoa$^{fl/fl}$:Cx3cr1^{CreER+} mutants (**Fig. 1G**).

In addition to microglia, long-lived non-parenchymal macrophages residing on brain interfaces are potentially targeted using Cx3cr1^{CreER+} mice (Goldmann et al., 2016). However, and in contrast to microglia, Rhoa expression in brain macrophages (CD11b^{+}CD45^{high} cells; gated as shown in **Suppl. Fig. 4A**) as well as their numbers, viability and reactivity were comparable between Rhoa$^{fl/fl}$:Cx3cr1^{CreER+} mice and aged-matched Rhoa$^{fl/fl}$ littermates (**Suppl. Fig. 4A and B**). Because Cx3cr1 is also expressed

on peripheral organs (Jung et al., 2000), some degree of Cre-mediated recombination was expected to occur outside the CNS of Rhoa$^{fl/fl}$:Cx3cr1^{CreER+} mice after tamoxifen administration (Parkhurst et al., 2013, Goldmann et al., 2013, Yona et al., 2013). However, monocyte fast turnover rate determines that after tamoxifen clearance, non-recombined monocytes will rapidly replace the recombined ones. Accordingly, and differently from microglia, qRT-PCR analysis on flow cytometry-sorted blood monocytes or spleen macrophages 35 days post-tamoxifen (**Suppl. Fig. 4C**) showed similar abundance of Rhoa mRNA transcripts in Rhoa$^{fl/fl}$:Cx3cr1^{CreER+} mice and Rhoa$^{fl/fl}$ littermates (**Suppl. Fig. 4D**). Likewise, flow cytometry on blood and spleen revealed similar percentage of different CD11b^{+} myeloid populations between Rhoa$^{fl/fl}$:Cx3cr1^{CreER+} mice and Rhoa$^{fl/fl}$ littermates (**Suppl. Fig. 4E and F**), indicating that the Rhoa$^{fl/fl}$:Cx3cr1^{CreER+} phenotype relates predominantly to microglia and not to macrophages.

To further establish that the loss of Rhoa in microglia would be sufficient to trigger their activation spontaneously in a cell autonomous manner, we depleted Rhoa in different microglia cell culture experimental setups (primary mouse cortical microglial cultures, and N9 or CHME3 microglial cell lines) and evaluated microglia activation. We found that (i) loss of Rhoa in primary cortical microglial cultures obtained from Rhoa floxed mice (**Suppl. Fig. 5A**) led to increased expression and secretion of Tnf (**Suppl. Fig. 5B and C**), and that (ii) knocking down (KD) Rhoa in microglial cell lines (**Suppl. Fig. 5D**) also increased Tnf expression (**Suppl. Fig. 5E**) and secretion (**Suppl. Fig. 5F**), (iii) increased NFκB activation, as shown by nuclear accumulation of p65 subunit of the NFκB complex (**Suppl. Fig.** 5G **and H**), and (iv) led to the degradation of the inhibitor of κB (**Suppl. Fig. 5I**) (Shcherbakova et al., 2016). We concluded that besides regulating microglial survival, Rhoa deficiency triggers spontaneous microglia activation.

Rhoa deficiency in adult microglia leads to synapse loss and neurodegeneration

Increased secretion of Tnf by microglia can be detrimental to neurons because Tnf autocrinally increases the release of glutamate (Socodato et al., 2015a, Takeuchi et al., 2006) thus causing excitotoxic damage to neurites and neurons (Jin et al., 2015, Maezawa and Jin, 2010). We investigated whether this was also the case in Rhoa KD microglia. Using the glutamate release FRET biosensor FLIPE600n^{Surface}, which specifically discriminates glutamate release over its uptake or its intracellular mobilization via cell metabolism (Okumoto et al., 2005), we showed that Rhoa KD increased glutamate release from living primary cortical microglia (**Fig. 2A**). This release led to an increase in extracellular content of glutamate relative to control microglia (**Fig. 2B**). Incubation of primary hippocampal neurons with conditioned media (CM) collected from primary cortical microglia knocked down for Rhoa (Rhoa KD MCM) induced a large increase in neurite beading (**Fig. 2C**), a characteristic of neuronal damage caused by glutamate excitotoxicity (Maezawa and Jin, 2010). To confirm that microglia-secreted glutamate was driving neurite damage, we pharmacologically inhibited the NMDA-type of glutamate receptors on hippocampal neurons and found that it abrogated the effect of Rhoa KD MCM in inducing neurite beading (**Fig. 2C**). We concluded that microglia lacking Rhoa become neurotoxic and can damage neurons via increased secretion of glutamate.

We then evaluated the impact of microglia-dependent neurotoxicity in Rhoa$^{fl/fl}$:Cx3cr1^{CreER+} mice. Here we focused our analyses primarily on the hippocampus because this brain region is vulnerable to Tnf-induced glutamate excitotoxicity (Yu et al., 2002). We first investigated whether loss of Rhoa in adult microglia would lead to changes on hippocampal synapses. By double-labeling immunohistochemistry against vGlut-1 and

PSD-95 we found less excitatory synaptic puncta on hippocampal tissue sections obtained from Rhoa$^{fl/fl}$:Cx3cr1^{CreER+} mice (evaluated by the number of vGlut-1^{+}/PDS-95^{+} colocalization puncta) compared with Rhoa$^{fl/fl}$ littermates (**Fig. 2D**). Whereas the amounts of hippocampal vGlut-1 protein were comparable between Rhoa$^{fl/fl}$:Cx3cr1^{CreER+} and the Rhoa$^{fl/fl}$ mice, the amounts of PSD-95 were significantly reduced in the hippocampus of Rhoa$^{fl/fl}$:Cx3cr1^{CreER+} mice (**Fig. 2E**). Together, these data indicate that besides damaging neurons, microglia-specific ablation of Rhoa leads to synapse loss.

Because synapse loss can adversely affect neuronal plasticity and behavior (Di Filippo et al., 2008, Brown and Neher, 2014), we assessed long-term potentiation (LTP) of hippocampal synapses in Rhoa$^{fl/fl}$:Cx3cr1^{CreER+} animals. We studied LTP by delivering θ-burst stimulation to the Schaffer collateral fibers, and recording field excitatory post-synaptic potentials (fEPSP) in the *stratum radiatum* of hippocampal CA1 region. θ-burst stimulation of hippocampal slices from Rhoa$^{fl/fl}$ mice led to an initial enhancement of fEPSP slope followed by a decrease and stabilization period, but at the end of recording period, fEPSP slope values remained higher than before θ-burst stimulation (**Fig. 2F blue circles**). In Rhoa$^{fl/fl}$:Cx3cr1^{CreER+} slices, however, the same θ-burst stimulation caused only an initial transient increase in fEPSPs slope values, which decreased progressively towards pre-θ-burst levels at the end of LTP recording (**Fig. 2F red circles**). As expected, LTP magnitude was significantly lower on hippocampal slices from Rhoa$^{fl/fl}$:Cx3cr1^{CreER+} mice than on hippocampal slices from control littermates (**Fig. 2G**), indicating a marked impairment of LTP in Rhoa$^{fl/fl}$:Cx3cr1^{CreER+} hippocampi.

Changes in synapse number/function may be associated with neuronal cell death (Palop et al., 2006). Indeed, we found an increase in TUNEL positive cells in hippocampi of Rhoa$^{fl/fl}$:Cx3cr1^{CreER+} mice compared with hippocampi from Rhoa$^{fl/fl}$ littermates (**Fig. 2H**), indicating neuronal apoptosis. In line with this, Rhoa$^{fl/fl}$:Cx3cr1^{CreER+} hippocampi contained

less NeuN positive neurons than hippocampi from Rhoa$^{fl/fl}$ littermates (**Fig. 2H**).

Synapse loss and LTP impairment can result in behavioral deficits. To address this possibility, we compared the performance of Rhoa$^{fl/fl}$:Cx3cr1^{CreER+} and Rhoa$^{fl/fl}$ mice in different behavioral paradigms, including elevated plus-maze (EPM) to evaluate anxiety-related behavior; open field (OF) to test general activity levels and gross motor function; and novel object recognition (NOR) to test recognition memory. Both EPM (**Suppl. Fig. 6A**) and OF (**Suppl. Fig. 6B-G**) tests did not show significant differences between Rhoa$^{fl/fl}$:Cx3cr1^{CreER+} and Rhoa$^{fl/fl}$ littermates. In the NOR test, however, Rhoa$^{fl/fl}$:Cx3cr1^{CreER+} mice spent less time exploring the novel object (**Fig. 2I**) and their capacity to discriminate the novel object over the familiar object was reduced compared with Rhoa$^{fl/fl}$ mice, indicating deficits in recognition memory (**Fig. 2I**). Total object exploration time was similar between the genotypes (**Fig. 2I**). Collectively, these data indicate that microglial Rhoa signaling is critical for neuronal function in the brain at the steady state.

Given that Rhoa, Rhob and Rhoc belong to the same Rho GTPase subclass and share high degree of similarity (Wheeler and Ridley, 2004), we asked whether depleting Rhob or Rhoc would also lead to spontaneous microglial activation. Contrasting to Rhoa KD, the KD of Rhob or Rhoc (**validations in Suppl. Fig. 7A**), did not alter microglia morphology (**Suppl. Fig. 7B**), ROS production (**Suppl. Fig. 7C**), glutamate release (**Suppl. Fig. 7D**), NFkB nuclear translocation (**Suppl. Fig. 7E**) or Tnf release (**Suppl. Fig. 7F**). Furthermore, CM from Rhob KD or Rhoc KD microglial cultures did not induce neurite beading on hippocampal neurons (**Suppl. Fig. 7G**). To check whether a compensatory Rhoc upregulation could explain the microglia activation triggered by Rhoa KD, we measured, by FRET, Rhoc activity in living Rhoa KD microglia and detected no overt difference in basal Rhoc activation relative to control microglia (**Suppl. Fig. 7H**). We

concluded that neither Rhob nor Rhoc compensated the spontaneous microglial activation induced by Rhoa deficiency.

Rhoa restrains Src tyrosine kinase activity in microglia

We next investigated the signaling pathway downstream of Rhoa controlling microglial immune restraint. Csk, the endogenous repressor of Src family of tyrosine kinases (SFKs) (Nada et al., 1991), is a tyrosine kinase that plays key roles in inflammation (Thomas et al., 2004). Besides, Src, the prototype and founding SFK member, is a key regulator of microglia activation (Socodato et al., 2015b). Therefore, Csk/Src emerged as good candidates for controlling microglial function and we hypothesized that Rhoa might modulate microglia immune restraint and activation via this pathway.

To test this hypothesis, we first investigated whether Rhoa deficiency increased Src activity in microglia. We analyzed Src activation on MACS-isolated microglia obtained from the brains of $Rhoa^{fl/fl}$:$Cx3cr1^{CreER+}$ and $Rhoa^{fl/fl}$ mice by Western blotting for active Src (phosphorylated at Tyr^{416}). Our results showed that $Rhoa^{fl/fl}$:$Cx3cr1^{CreER+}$ microglia contained higher amounts of active Src compared with control microglia (**Fig. 3A**). Then, we analyzed by Western blotting the amounts of Src $pTyr^{416}$ on lysates obtained from Rhoa KD and control N9 microglia. Src $pTyr^{416}$ amounts were significantly higher in Rhoa KD N9 microglia than in control microglia (**Fig. 3B**). Next, using the Src activity biosensor KRas Src YPet (Ouyang et al., 2008), we measured, by FRET, Src activity at the plasma membrane of living Rhoa KD CHME3 microglia. We found a significant increase in Src activity in Rhoa KD CHME3 microglia compared with controls (**Fig. 3C**). To further demonstrate that Src activity is directly linked to Rhoa function, we then used the pSicoR vector (Ventura et al., 2004) to knockdown Rhoa in CHME3 microglia expressing Cre recombinase (lenti-Cre microglia - infected with a lenti-Cre virus) or an empty vector (lenti-

CT microglia - infected with a lenti-CT virus). In the pSicoR vector system, loxP sites flank shRNA sequences and an EGFP cassette, which is expressed as a marker. Cre expression causes recombination and excision of both shRNA and EGFP sequences, turning their expression off (**Fig. 3D**). We found that activation of Src (as measured by Src pTyr^{416}) did not change by expressing a scrambled shRNA sequence in lenti-CT microglia or in lenti-Cre microglia (**Fig. 3E, blue bars on the graph**), but significantly increased by expressing shRhoa sequences in lenti-CT microglia (**Fig. 3E, compare the first and third bars on the graph**). Importantly, expressing shRhoa in lenti-Cre microglia excised shRhoa sequences and Src activation was retained to control levels (**Fig. 3E, compare the second and forth bars on the graph**). From these experiments we concluded that Rhoa suppresses Src activation in microglia.

Next, we investigated whether Rhoa deficiency decreased Csk expression because Csk endogenously represses Src activation by phosphorylating Src C-terminal region leading to constitutive Src inhibition (Nada et al., 1991). First, we examined, using qRT-PCR on microglia sorted from Rhoa$^{fl/fl}$:Cx3cr1^{CreER+} and Rhoa$^{fl/fl}$ brains, whether ablating Rhoa in microglia affected Csk transcript abundance. We observed a decrease of Csk mRNA transcripts in Rhoa$^{fl/fl}$:Cx3cr1^{CreER+} microglia (**Fig. 3F**). To evaluate whether a decrease in Csk mRNA resulted in reduced Csk protein content, we analyzed, by Western blotting, Csk amounts on lysates obtained from Rhoa KD N9 microglia and control microglia. We detected a significant decrease in Csk protein amounts in Rhoa KD N9 microglia compared with those in controls (**Fig. 3G**).

To further link Rhoa activity with regulation of Csk expression, we forced Rhoa activation by expressing the constitutively active Rhoa mutant Rhoa^{Q63L} in microglia. We found that CHME3 microglia expressing Rhoa^{Q63L} had higher amounts of Csk and, consequently, lesser amounts of active Src than control microglia (**Fig. 3H and Suppl.**

Fig. 8A and B), suggesting that Rhoa is a direct upstream regulator of microglial Csk/Src pathway.

To strengthen the link between Rhoa activity, Csk expression and Src activity in microglia, we tested whether depleting Csk whilst activating Rhoa would result in Src activation. We forced Rhoa activation using a Rho GTPase chemical inducible dimerization (CID) strategy (**Fig. 3I**). In this experimental set-up the FK506 binding protein (FKBP) and rapamycin binding domain of mTOR (FRB) is fused to the membrane targeting sequence of Lyn (Lyn_{11}-FRB) to provide a plasma membrane anchor for the constitutively active form of Rhoa (Rhoa CA), which is expressed as a cytosolic fusion with FKBP and YFP (Inoue et al., 2005). When microglia expressing both constructs are exposed to rapamycin, YFP-FKBP-Rhoa (CA) rapidly translocates to the plasma membrane and binds to Lyn_{11}-FRB triggering fast activation of Rhoa (Inoue et al., 2005) (**Fig. 3I**). We found that following exposure to rapamycin, activation of Rhoa in pLKO CHME3 microglia expressing both Lyn_{11}-FRB and YFP-FKBP-Rhoa (CA) (Rhoa-CID) substantially decreased Src activation relative to microglial clones co-expressing Lyn_{11}-FRB and YFP-FKBP (CT-CID) (**Fig. 3J**). However, in Csk-depleted microglia (Csk KD; **validation in Suppl. Fig 8C**), triggering activation of Rhoa (Rhoa-CID) failed to decrease Src activation (**Fig. 3J**), further confirming that Rhoa activity is required for Csk expression and downstream control of Src activation in microglia.

Lastly, we examined whether forcing Csk downregulation or Src hyperactivation would be sufficient to promote NFκB activation and consequently expression and secretion of Tnf, which is associated with the spontaneous microglia activation. Our results showed that Csk KD (**validation in Suppl. Fig. 8C**), which caused a large increase in Src activation (**Suppl. Fig. 8D**), or expressing the constitutively active Src mutant Src^{Y527F} (**Suppl. Fig. 8D; with additional control in Fig. Suppl. Fig. 8E**) in CHME3 microglia led

to nuclear accumulation of NFκB (assessed by increased nuclear fluorescence of the p65-GFP construct) (**Fig. 3K**), and increased Tnf secretion (**Fig. 3L**).

Blocking Src tyrosine kinase activity prevents synapse loss and neurodegeneration

Next, we investigated whether blocking Src could rescue, to some extent, the deregulation of microglia activation, synaptotoxicity and the associated memory deficits in Rhoa$^{fl/fl}$:Cx3cr1^{CreER+} mice. Therefore, following tamoxifen administration, we injected Rhoa$^{fl/fl}$:Cx3cr1^{CreER+} mice weekly with the potent Src blocker AZD 0530 (**Fig. 4A**), which crosses the blood-brain barrier and enters the brain (Kaufman et al., 2015), and one month later confirmed that this regimen of AZD 0530 administration was indeed effective in decreasing Src activation as measured by Western blot for Src phospho-Tyr^{416} (**Fig. 4B**). Accordingly, we have also shown that a single IP injection of AZD 0530 was sufficient to reduce Src activation in the brains of naïve WT mice for at least 8 days (**Suppl. Fig. 9A**). Src inhibition by AZD 0530 prevented the decrease of microglial numbers in Rhoa$^{fl/fl}$:Cx3cr1^{CreER+} mice (**Fig. 4C and D; Suppl. Fig. 9B and C**), suggesting that inhibiting Src limits microglial cell loss following Rhoa ablation.

AZD 0530 also prevented the increase of mRNA transcript of Tnf in Rhoa$^{fl/fl}$:Cx3cr1^{CreER+} brains (**Fig. 4E**). Furthermore, expressing the dominant negative Src mutant Src^{Y416F} in Rhoa KD microglia prevented Tnf release compared with Rhoa KD microglia (**Fig. 4F**). Consistent with this, Src^{Y416F} expression also caused reduced activation of NFκB, by showing less nuclear translocation of GFP-tagged p65 NFκB subunit in Rhoa KD microglia compared with the controls (**Suppl. Fig. 9D**). We further confirmed that microglia activation required Src function by showing that pharmacological inhibition of Src, using the Src blocker SKI-1, in Csk KD microglia also prevented Tnf release (**Fig. 4F**) and nuclear translocation of the GFP-tagged p65 NFκB subunit (**Suppl.**

Fig. 9D). Collectively, these data suggest that Rhoa promotes microglia immune restraint by suppressing Src activity through Csk.

Because blocking Src activity in microglia lacking Rhoa abrogated Tnf production we postulated that it would also inhibit glutamate release, thereby preventing microglia from becoming neurotoxic. Our results showed that ablating microglial Tnf (using Tnf KO) abrogated the release of glutamate triggered by depleting Rhoa (**Fig. 4G**) and, as expected, Tnf dose-dependently increased the release of glutamate from microglia (**Fig. 4H**). To further confirm that Tnf released from microglia was inducing the release of glutamate we used Adalimumab (a monoclonal anti-Tnf blocking antibody). Adalimumab completely blocked the release of glutamate triggered by overexpressing the dominant negative Rhoa mutant $Rhoa^{T19N}$ in microglia (**Fig. 4I**). Whereas the Src inhibitor SKI-1 attenuated the release of glutamate in Rhoa KD microglia (**Fig. 4J**), exogenous application of Tnf rescued the release of glutamate after inhibiting Src in Rhoa KD microglia (**Fig. 4J**), further confirming that Tnf is a major inducer of glutamate release downstream of Rhoa and Src. Preventing Tnf production in Rhoa KD microglia, using the antineoplastic Tnf inhibitor pomalidomide (POM), also inhibited the increase of glutamate release (**Fig. 4J**) and exogenous application of Tnf in Rhoa KD cells rescued glutamate release even in the presence of POM (**Fig. 4J**).

One main route for glutamate release from active microglia is its extrusion through gap junction hemichannels (Jin et al., 2015, Maezawa and Jin, 2010, Takeuchi et al., 2006, Socodato et al., 2018). Accordingly, blocking gap junctions using 18-alpha-glycyrrhetinic acid in Rhoa KD microglia prevented glutamate release (**Fig. 4J**). In addition, hyperactivating Src (by Csk KD or by expressing Src^{Y527F}) recapitulated the effect of Rhoa KD in microglia and increased glutamate release (**Fig. 4J**).

Increasing basal Rhoa activation in microglia by expressing Rhoa^{Q63L} was sufficient to decrease glutamate release (**Fig. 4K**). Therefore, we hypothesized that if Src acted downstream of Rhoa to promote glutamate release, then forcing Src activation, which increases Tnf production (**Fig. 3L**), in Rhoa^{Q63L}-expressing microglia should result in glutamate release. To test this hypothesis, we used a Src-CID strategy (by co-transfecting microglia with a rapamycin-inducible Src heteromerization quimera (RapR-Src) and FRB-Cherry to exert precise temporal control over Src activation (Karginov et al., 2010). In line with our hypothesis, exposing microglial cultures co-expressing RapR-Src and FRB-mCherry (Src-CID) to rapamycin led to a significant increase in glutamate release relative to control cells (**Fig. 4K**) and resulted in the release of glutamate in cells expressing Rhoa^{Q63L} (**Fig. 4K**). Paralleling this increase in glutamate release, Rhoa KD or direct Src hyperactivation led to an accumulation of glutamate in the extracellular medium compared with the extracellular medium of control microglia (**Fig. 4L**). As expected, inhibiting Src with SKI-1 in Rhoa KD microglia also abrogated extracellular accumulation of glutamate (**Fig. 4L**).

Glutamate release by microglia can cause neurite damage by excitotoxicity, thus we assessed whether inhibiting Src or Tnf after depleting Rhoa would attenuate neurite damage in hippocampal neurons. CM from Tnf-deficient microglia prevented neurite beading caused by Rhoa KD (**Fig. 4M and Suppl. Fig. 9E**). Besides, microglial inhibition of Src (either with SKI-1 or by overexpressing the dominant negative Src mutant Src^{Y416F}) prevented neurite beading in cultured hippocampal neurons caused by the CM of Rhoa KD microglia (**Fig. 4N and Suppl. Fig. 9F**). CM obtained from Rhoa KD microglia in which Tnf was inhibited with POM also prevented neurite beading and adding recombinant Tnf to Rhoa KD microglia in the presence of POM induced neurite beading (**Fig. 4N and Suppl. Fig. 9F**). As expected, the CM of control microglia treated with Tnf also caused

extensive neurite beading (**Fig. 4N and Suppl. Fig. 9F**). Paralleling the effect in neurite damage, we also found that the CM from microglia overexpressing the dominant negative Rhoa mutant Rhoa^{T19N} produced a significant loss of synaptic puncta in primary hippocampal neurons (**Fig. 4O**) and decreasing microglial Src activity (by overexpressing a dominant negative Src mutant) or blocking microglial Tnf (using the anti-Tnf antibody Adalimumab) significantly attenuated this effect (**Fig. 4O**). We concluded that by preventing Tnf production and Tnf-induced glutamate secretion, Src inhibition limited the neurotoxicity of Rhoa-deficient microglia.

Because Src inhibition limited microglia activation and associated neuronal damage, we evaluated whether the Src blocker AZD 0530 would prevent the loss of synapses in vivo in Rhoa$^{fl/fl}$:Cx3cr1^{CreER+} hippocampus. Indeed, we found that Rhoa$^{fl/fl}$:Cx3cr1^{CreER+} mice injected with AZD 0530 contained more excitatory synapses (vGlut-1^{+}/PSD95^{+} colocalization puncta) than Rhoa$^{fl/fl}$:Cx3cr1^{CreER+} mice injected with vehicle (**Fig. 4P**). Accordingly, hippocampal synapses in AZD 0530-injected Rhoa$^{fl/fl}$:Cx3cr1^{CreER+} mice were similar to those in Rhoa$^{fl/fl}$ littermates injected with vehicle (**Fig. 4P**), indicating that AZD 0530 almost completely prevented excitatory synapse loss following Rhoa ablation in adult microglia. We further revealed, by Western blotting on hippocampal lysates, that the protein amounts of the structural synaptic markers synapsin-1, synaptophysin and PSD-95 were higher in hippocampi of Rhoa$^{fl/fl}$:Cx3cr1^{CreER+} mice injected with AZD 0530 than in hippocampi of Rhoa$^{fl/fl}$:Cx3cr1^{CreER+} mice injected with vehicle (**Suppl. Fig. 9G**).

Next, we evaluated, using the NOR test, whether AZD 0530 would also attenuate memory deficits after Rhoa ablation in adult microglia. Rhoa$^{fl/fl}$:Cx3cr1^{CreER+} mice injected with AZD 0530 spent more time exploring the novel object (**Fig. 4Q**) and discriminated the novel object better than Rhoa$^{fl/fl}$:Cx3cr1^{CreER+} mice injected with vehicle (**Suppl. Fig. 9H**).

We observed no differences in total object exploration time between Rhoa$^{fl/fl}$:Cx3cr1^{CreER+} mice injected with AZD 0530 and controls (**Suppl. Fig. 9I**). These data suggest that suppressing Src activation in Rhoa$^{fl/fl}$:Cx3cr1^{CreER+} mice, using a clinically relevant Src inhibitor, improved their memory performance by limiting microglia-induced synapse loss.

Importantly, we did not find significant differences between DMSO-injected Cx3cr1^{CreER+}, AZD-injected Cx3cr1^{CreER+} or Rhoa$^{fl/fl}$ mice in microglial numbers (**Suppl. Fig. 10A**), excitatory synapse number (**Suppl. Fig. 10B**), recognition memory (**Suppl. Figs. 10C and D**), anxiety-related behavior (**Suppl. Figs. 10E-I**) and locomotor activity (**Suppl. Fig. 10J**), suggesting that AZD administration did not affect these features at the steady state. In addition, these results further indicate that the loss of one Cx3cr1 allele did not contribute for the phenotypes observed in the Rhoa$^{fl/fl}$:Cx3cr1^{CreER+} mice.

Because Tnf drives glutamate release and neurite toxicity downstream of Rhoa and Src in microglia we asked whether the increase of brain Tnf expression contributed to synapse loss in Rhoa$^{fl/fl}$:Cx3cr1^{CreER+} mice. We injected Rhoa$^{fl/fl}$:Cx3cr1^{CreER+} and control Cx3cr1^{CreER+} mice with POM (50 mg/Kg IP 3 times per week over 4 weeks) and found that this dosage of POM dramatically decreased the expression of Tnf in the brains of Cx3cr1^{CreER+}and Rhoa$^{fl/fl}$:Cx3cr1^{CreER+} mice (**Suppl. Fig. 10K**). Besides decreasing brain Tnf expression, POM administration also significantly prevented the decrease of vGlut-1^{+}/PSD95^{+} colocalization puncta in Rhoa$^{fl/fl}$:Cx3cr1^{CreER+} mice (**Suppl. Fig. 10L**), suggesting that the increased Tnf expression was, at least in part, involved in the synapse loss elicited by the ablation of Rhoa in microglia.

Ablation of Rhoa in adult microglia leads to an amyloid-like pathology

Together with synapse loss, LTP impairment and memory deficits (**Fig. 2**), deposition of amyloid beta (Aβ) underlies multiple CNS neurodegenerative states,

including Alzheimer´s Disease (AD). Interestingly, we found that ablation of Rhoa in adult microglia resulted in increased amounts of Aβ (**Fig. 5A**) and its amyloidogenic precursor β-CTF (a carboxyl-terminal fragment generated by the cleavage of APP by β-secretases; **Fig. 5B**) in the brain of Rhoa$^{fl/fl}$:Cx3cr1^{CreER+} mice. Total APP levels were comparable between Rhoa$^{fl/fl}$ and Rhoa$^{fl/fl}$:Cx3cr1^{CreER+} mice (**Fig. 5B**). Corroborating the increased amyloidogenic processing of APP, we detected, using ELISA, increased amounts of Aβ_{1-40} peptide and of Aβ_{1-42} peptide in the brains of Rhoa$^{fl/fl}$:Cx3cr1^{CreER+} mice compared with Rhoa$^{fl/fl}$ littermates (**Fig. 5C**). Moreover, we also found that the excess of Aβ formed fibrillar plaque-like structures (labeled by methoxy-X04) in the neocortex of Rhoa$^{fl/fl}$:Cx3cr1^{CreER+} mice but not in Rhoa$^{fl/fl}$ neocortices (**Fig. 5D**). Production of Aβ by neurons is in large part activity-dependent (Cirrito et al., 2005) and induced by activation of glutamate receptors (Lesne et al., 2005). As decreasing Rhoa activity in microglia enhanced glutamate secretion, we investigated whether this increase modulated the production of Aβ by neurons. We found that the CM from microglia overexpressing the dominant negative Rhoa mutant Rhoa^{T19N} induced a significant increase of Aβ42 in primary hippocampal neurons (**Fig. 5E**). This effect was abrogated by decreasing microglial Src activity (by overexpressing a dominant negative Src mutant) or by blocking microglial Tnf with the anti-Tnf antibody Adalimumab (**Fig. 5E**).

Aβ oligomers induce microglia neurotoxic polarization by decreasing Rhoa activity

Our results in Rhoa$^{fl/fl}$:Cx3cr1^{CreER+} mice suggest that microglia dysregulation drives amyloidogenic processing of APP leading to increased production of Aβ by neurons, but could Aβ signal back to microglia and alter Rhoa activity? Using APP/PS1 mice (Borchelt et al., 1997, Borchelt et al., 1996), in which Aβ is abundantly produced and secreted by neurons, we found by flow cytometry, a significant reduction of microglia

($CD45^{mid}CD11b^{+}$ cells) expressing the active form of Rhoa (GTP-Rhoa) in 4 mo APP/PS1 brains when compared with WT littermates (**Fig. 5F**). Consistent with this, we also detected a decrease of microglia expressing Csk and an increase of microglia expressing active Src (phosphorylated at Tyr^{416}) in 4 mo APP/PS1 brains compared with the brains of WT littermates (**Fig. 5F**). We found no significant differences in the numbers of microglia, brain macrophages or blood monocytes between 4 mo APP/PS1 and WT littermates (**Suppl. Fig. 11A and B**). Furthermore, we did not detect significant differences in the percentages of brain macrophages or in those of circulating blood monocytes expressing GTP-Rhoa, Csk or Src Tyr^{416} phosphorylation between 4 mo APP/PS1 and WT littermates (**Suppl. Fig. 11C and D**).

Next, we investigated whether application of low amounts (200 nM) of $A\beta_{1-42}$ oligomers (Walsh and Selkoe, 2007) could indeed modulate the Rhoa signaling in microglia. In line with the in vivo results showing a decrease in Rhoa activation in microglia of APP/PS1 mice, we found, by FRET using the Raichu-Rhoa biosensor (Yoshizaki et al., 2003), that Rhoa activity in living microglia dramatically decreased following exposure to $A\beta_{1-42}$ oligomers (**Fig. 5G and Suppl. Fig. 11E**). Conversely, Src activity at the plasma membrane (visualized by FRET with the KRas Src YPet biosensor) increased (**Fig. 5H and Suppl. Fig. 11F**), and expression of the constitutively active Rhoa mutant $Rhoa^{Q63L}$ significantly attenuated this effect (**Fig. 5H and Suppl. Fig. 11F**).

Importantly, by using the pIκBα-miRFP703 biosensor to detect the activation of canonical NFκB pathway (Shcherbakova et al., 2016), we also observed that exposure to $A\beta_{1-42}$ oligomers induced time-dependent activation of the NFκB pathway in living microglia (**Fig. 5I and Suppl. Fig. 11G**), and overexpressing $Rhoa^{Q63L}$ or blocking Src with AZD 0530 abrogated this effect (**Fig. 5I and Suppl. Fig. 11G**). Finally, using the FLIPE

biosensor we observed by FRET that exposure to $A\beta_{1-42}$ oligomers increased glutamate release from living microglia in a time-dependent manner (**Fig. 5J and Suppl. Fig. 11H**), an effect inhibited by $Rhoa^{Q63L}$, by AZD 0530 and by neutralizing Tnf with Adalimumab (**Fig. 5J and Suppl. Fig. 11H**). Taken together, these data suggest that Aβ oligomers can signal back to microglia and decrease RhoA activation, thereby providing a positive feedback loop for Src hyperactivation and Tnf-dependent glutamate release.

Blocking Src decreases amyloid-like pathology in $Rhoa^{fl/fl}$:$Cx3cr1^{CreER+}$ mice

Next, we investigated if inhibiting Src would modulate the reactivity of microglia in early-deposing APP/PS1 mice. Of note, a single IP injection of AZD 0530 in APP/PS1 mice was sufficient to decrease Src activity in their brains for at least a week (**Suppl. Fig. 11I**). Therefore, and as we did for $Rhoa^{fl/fl}$:$Cx3cr1^{CreER+}$ mice, we blocked Src activity by giving AZD 0530 weekly to 3 mo APP/PS1 mice for 1 month (**Suppl. Fig. 11J**) and investigated whether Src inhibition would preserve hippocampal synapses. In line with previous results (Hong et al., 2016), we confirmed that 4 mo APP/PS1 mice displayed a notorious loss of hippocampal synapses, revealed by a decrease in vGlut-1^+/PSD-95^+ colocalization puncta, relative to WT littermates (**Suppl. Fig. 11K**). Injecting AZD 0530 in APP/PS1 mice substantially inhibited the decrease of vGlut-1^+/PSD-95^+ colocalization puncta compared with age-matched APP/PS1 mice injected with vehicle (**Suppl. Fig. 11K**). Indeed, vGlut-1^+/PSD-95^+ colocalization puncta was comparable between AZD-injected APP/PS1 mice and vehicle-injected WT littermates (**Suppl. Fig. 11K**), thereby suggesting that the blockade of Src preserves hippocampal synapses in early-depositing APP/PS1 mice.

Concurrent with the idea that Src inhibition decreases microglia activation, using Sholl analysis in $Iba1^+$ microglia, we found increased microglial ramification in the

neocortex of APP/PS1 mice injected with AZD 0530 compared with APP/PS1 littermates injected with vehicle (**Suppl. Fig. 11L**). Paralleling this increased microglial ramification in APP/PS1 mice treated with AZD 0530, we also observed an increase in the ramification of microglia following Src inhibition with AZD 0530 in Rhoa$^{fl/fl}$:Cx3cr1^{CreER+} mice (**Suppl. Fig. 11M**).

Plaque-associated microglia restrict amyloid plaque formation limiting pathology in AD mouse models by phagocytosis of amyloid deposits (Wang et al., 2015, Wang et al., 2016). We thus investigated whether Rhoa activation and consequent blockade of Src would improve microglial engulfment of Aβ. Indeed, chemogenetic activation of Rhoa using the Rhoa-CID strategy (**Fig. 3I**) significantly increased the uptake of Aβ_{1-42} by microglia (**Fig. 6A**). Activation of Rhoa led to Src inhibition (**Fig. 3H and J**) and, accordingly, blockade of Src with AZD 0530 increased the uptake of Aβ_{1-42} by microglia (**Fig. 6B**). In addition, we performed colocalization analysis for Iba1^{+} microglia and Aβ deposits in vivo both in APP/PS1 mice and in Rhoa$^{fl/fl}$:Cx3cr1^{CreER+} mice. Our results showed that blocking Src with AZD 0530 promoted a significant increase of microglial engulfment of Aβ deposits both in the neocortex and hippocampus of APP/PS1 mice relative to APP/PS1 littermates injected with vehicle (**Suppl. Fig. 12A**). Similarly, we found that AZD 0530 inhibition of Src in Rhoa$^{fl/fl}$:Cx3cr1^{CreER+} mice increased the colocalization of Iba1^{+} microglia and Aβ deposits relative to Rhoa$^{fl/fl}$:Cx3cr1^{CreER+} injected with vehicle (**Fig. 6C and Suppl. Fig. 12B**), suggesting that inhibiting Src in Rhoa-deficient microglia also increases the engulfment of Aβ. AZD 0530 treatment caused no significant alterations in the amounts of APP either in APP/PS1 mice or in Rhoa$^{fl/fl}$:Cx3cr1^{CreER+} mice (**Suppl. Fig. 12C and D**), indicating that AZD 0530 does not impact APP production.

Paralleling the increased Aβ clearance by microglia, we observed a significant

decrease of amyloid burden (Aβ amounts detected using BAM-10 and E610 antibodies) in the brain of APP/PS1 mice injected with AZD 0530 compared with APP/PS1 littermates injected with vehicle (**Suppl. Fig. 12E and F**). Importantly, AZD 0530 significantly decreased Aβ deposition (**Fig. 6D and Suppl. Fig. 12G**), the production of both $A\beta_{1-40}$ and $A\beta_{1-42}$ peptides (**Fig. 6E**) and the formation of fibrillar plaque-like structures labeled by methoxy-X04 (**Fig. 6F**) in the neocortex of $Rhoa^{fl/fl}$:$Cx3cr1^{CreER+}$ mice compared with $Rhoa^{fl/fl}$:$Cx3cr1^{CreER+}$ littermates injected with vehicle. We concluded that blockade of Src downstream of Rhoa mitigates amyloid burden, highlighting the fundamental importance of microglial Rhoa signaling for synaptic integrity and neuronal function.

Discussion

Using inducible tissue-specific conditional gene ablation in mice, we demonstrated for the first time that Rhoa signaling is essential for adult microglia survival, activation and immune activity. Genetic ablation of Rhoa in healthy adult microglia resulted in microglial cell death and spontaneous microglia activation giving rise to a neurological phenotype, which included synapse loss, impairment of LTP, neuronal cell death, deficits in recognition memory, the formation of pathological Aβ species and fibrillar amyloid-like structures. Mechanistically, we showed that the loss of Rhoa led to Src activation, NFκB nuclear translocation, Tnf production and glutamate release, and that inhibiting Src prevented microglial loss and spontaneous activation, microglia-induced synaptotoxicity and the other neurological phenotypes.

To some extent, the $Rhoa^{fl/fl}$:$Cx3cr1^{CreER+}$ (Rhoa mutant) phenotype resembled the one reported for animal models of AD, including the APP/PS1 mouse. Interestingly, we found a reduction in Rhoa activity and an increase in Src activation in APP/PS1 microglia. Consequently, inhibiting Src activity in either Rhoa mutants or APP/PS1 mice prevented synapse loss and decreased the Aβ burden. Our results point out for a fundamental role of Rhoa signaling in restraining microglia immune activity with a subsequent and direct impact in neurodegeneration.

To define the mechanisms regulating microglia homeostasis in the adult brain under physiological conditions remains an important task that has been facilitated by the availability of microglia-specific Cre lines based on the insertion of a Cre^{ER} cassette into the Cx3cr1 locus (Parkhurst et al., 2013, Goldmann et al., 2013). These mouse lines allow very efficient and sustained microglial gene recombination because they take advantage of (1) the higher expression of Cx3cr1 in microglia in relation to other non-parenchymal

myeloid cells (Goldmann et al., 2016) and of the fact that (2) microglia are a self-sustained and long-lived cell population in the nervous tissue (Tay et al., 2017, Fuger et al., 2017, Askew et al., 2017). By crossing Cx3cr1$^{CreER\text{-}EYFP}$ mice (Parkhurst et al., 2013) with Rhoa floxed mice (Herzog et al., 2011, Jackson et al., 2011) we studied, for the first time, the *bona fide* role(s) of Rhoa in adult brain microglia under physiological conditions. This approach circumvented some of the limitations of previous studies of Rhoa signaling using overexpression of Rhoa dominant mutants (Bianchi et al., 2011, Ohsawa et al., 2000, Moon et al., 2013), which may trigger off-target and trans-dominant effects (Zhou and Zheng, 2013, Wang and Zheng, 2007), as well as the use of C3 exoenzyme toxin (Rattan et al., 2003, Hoffmann et al., 2008), which not only inhibits Rhoa but also Rhob and Rhoc (Mohr et al., 1992, Chardin et al., 1989).

Rhoa works through multiple downstream pathways and effectors, and it is to be expected that the loss of Rhoa might disturb the functions and/or interactions of more than one of its effectors. In line with this, knocking out Rhoa or knocking out one of its effectors can give rise to discordant phenotypes. For example, knocking out Rhoa in the mouse spinal cord neuroepithelium does not cause cytokinesis defects (Herzog et al., 2011), whereas knocking out the Rhoa effector citron-kinase impairs cytokinesis (Di Cunto et al., 2000). This could also explain why Rhoa deficiency activates microglia whereas the pharmacological inhibition of the Rhoa effector Rho-kinase (ROCK) does not (Mueller et al., 2005, Chen et al., 2013). Another factor potentially contributing for the disparity of these 2 phenotypes is that in addition of being activated by Rhoa, ROCK can also be regulated by Rhoe/Rnd3 (Riento et al., 2003) or by Rhoc (Riento and Ridley, 2003). Our data, however, suggested that Rhoc did not play a significant role in microglia proinflammatory activation and microglia-induced neurotoxicity. In this context, ROCK inhibition by Y27632 or fasudil attenuates microglia activation, promoting some functional

recovery in animal models for different neurological conditions (Mueller et al., 2005, Chen et al., 2013, Chong et al., 2017, Sellers et al., 2018). Because Rhoa is likely to exert its control over microglia immune activity through several other downstream effectors besides ROCK, which activation can also be regulated independently of Rhoa (Julian and Olson, 2014), these studies are not very informative concerning Rhoa regulation of microglial function. In addition, Y27632 and fasudil are not cell specific and have substantial off-target effects (Vigil and Der, 2013). For instance, Y27632 or fasudil can inhibit protein kinase C (PKC) and other kinases involved in cytoskeleton regulation (Vigil and Der, 2013) that might potentially modulate microglial function. In this particular, PKC activation is important for TLR-mediated inflammation (Loegering and Lennartz, 2011) and its inhibition reduces microglial activation (Kim et al., 2005, Wen et al., 2011), making it difficult to attribute any phenotype solely to the inhibition of ROCK downstream of Rhoa. Importantly, conditional-gene targeting studies also show that many of the specific pathways regulated by a given RhoGTPase are cell type and stimulus specific, and that knowing the role of a RhoGTPase in a given cell type cannot necessarily predict its function and signaling mechanisms in another one (Wang and Zheng, 2007, Pedersen and Brakebusch, 2012).

Genetic ablation of Rhoa in adult microglia was sufficient to induce synapse loss, LTP impairment and deficits in recognition memory, indicating that disrupting microglia immune restraint altered the synaptic landscape, which is important for long-term synaptic plasticity and memory (Scannevin and Huganir, 2000). Inflammatory cytokines and glutamate secretion by microglia can adversely impact neuronal activity/plasticity and induce nerve cell damage (Brown and Neher, 2014). Microglia lacking Rhoa acquired a spontaneous activated phenotype that led to increased production and secretion of Tnf and glutamate. Glutamate is the major excitatory neurotransmitter in the CNS, being functionally involved in almost all higher-order brain functions. However, excessive

secretion of glutamate by microglia can induce excitotoxic neuronal damage (Jin et al., 2015, Maezawa and Jin, 2010, Socodato et al., 2015a, Takeuchi et al., 2006), and by exacerbating neuronal activity can also increase the production of Aβ species by neurons (Lesne et al., 2005). Indeed, our results support the latter as conditioned media obtained from microglia overexpressing the dominant negative $Rhoa^{T19N}$ mutant induced a significant increase of Aβ42 in primary hippocampal neurons.

Tnf signaling enhanced microglial release of glutamate by increasing its extrusion through gap junctions. Blocking Tnf and the consequent release of glutamate from microglia lacking Rhoa prevented neurite damage and also the increase of Aβ42 in primary hippocampal neurons. Injecting pomalidomide (a brain penetrant immunomodulatory agent that also inhibits Tnf expression) in Rhoa mutant mice decreased brain Tnf expression and attenuated synapse loss. Although pomalidomide might have inhibited other pathways in addition to Tnf, our in vitro data demonstrated that Tnf signaling was required for neurite beading and synapse loss, strongly suggesting that Tnf contributed for the synapse loss following Rhoa ablation in microglia.

The interplay between Rhoa and Src is essential for normal cellular behavior and, in most cases, Src is hierarchically upstream of Rhoa to relay the activity of growth factor receptors and/or integrin-dependent extracellular matrix signaling to modulate the GTPase function of Rhoa (Huveneers and Danen, 2009, Brouns et al., 2001, Arthur et al., 2000). However, Rhoa deficiency in microglia disrupted their immune restraint by downregulating the expression of Csk, which increased Src activation. Still, the precise molecular mechanism by which Rhoa activity sustains the expression of Csk in microglia at the steady state warrants further examination.

Blockade of Src activity in Rhoa mutant mice, using the clinically relevant Src

inhibitor AZD 0530 (Kaufman et al., 2015), preserved the physiology of microglia (maintained microglial cell numbers and activity). In addition, following injection with AZD 0530 Rhoa mutant mice displayed higher density of excitatory synapses and performed substantially better in a task assessing recognition memory compared with those mice injected with vehicle solution.

AZD 0530 inhibits the phosphorylation of SFKs, including Fyn, Src, Lyn, and other family members. Although AZD 0530 inhibits Src more potently than other SFK family members (for example the reported IC50 for Src is 2.7 nM, while for Fyn is around 10 nM (Green et al., 2009)), and despite of our compelling in vitro results pointing out for a key and rather specific role of Src in driving the phenotype produced by depleting Rhoa in microglia, we cannot claim that, in vivo, the only kinase inhibited was Src. This is also applicable to the work of Kaufmann and colleagues, who report that the beneficial effect of AZD 0530 in diminishing AD-like pathology in APP/PS1 mice is due to decreased Fyn activation in neurons (Kaufman et al., 2015). It is likely that besides inhibiting Fyn in neurons, AZD 0530 might also inhibit other SFK family members in neurons and in other brain cell types, including microglia. Accordingly, and in the context of our work, we cannot therefore exclude that the effect of AZD 0530 in preventing synapse loss and decreasing the amyloid burden in Rhoa mutants and in APP/PS1 mice was contributed, at least in part, by SFK inhibition in both glia and neurons.

We observed decreased Rhoa activity in microglia obtained from early-depositing APP/PS1 AD mice, at a stage in which synapse loss was already present without robust amyloid pathology on these animals. Such decrease of Rhoa activity in AD microglia, reproduced in vitro by the addition of low amounts of $A\beta_{1-42}$ oligomers, led to increased Src tyrosine kinase activity, which culminated in NFκB activation and increased glutamate secretion. This suggests that the decrease in microglial Rhoa activity, which led to Src-

induced secretion of excitotoxic glutamate, might have contributed to the synapse loss in early-depositing APP/PS1 mice. Indeed, blocking Src, downstream of Rhoa, in APP/PS1 mice prevented early synapse loss, increased microglial engulfment of Aβ and decreased Aβ burden. In line with our data, inhibitors of Src, of Tnf or of gap junctions (inhibitors of glutamate secretion through hemichannels) are now considered to be beneficial therapies for animal models of AD (Kaufman et al., 2015, Takeuchi et al., 2011, Ekert et al., 2018). On the other hand, substantial glial activation driven by overexpressing proinflammatory cytokines can also decrease amyloid burden in AD mice (Chakrabarty et al., 2011, Chakrabarty et al., 2010b, Chakrabarty et al., 2010a), casting doubts whether attenuating microglial activation *per se* would be sufficient to preserve synapses as amyloid pathology builds up during the course of AD.

Loss of synapses, LTP impairment, recognition memory deficits and deposition of Aβ are consistent hallmarks found in human AD patients and in animal models of AD. Similarly, Rhoa ablation in adult microglia reproduced some of these hallmarks, further supporting the hypothesis that disrupting Rhoa signaling leads to spontaneous microglia activation and subsequent neurodegeneration. In this regard, our data provide additional validation to notion of “microgliopathy” (Prinz and Priller, 2014), in which microglia dysfunction, by itself, could initiate or be a major cause of neurological disease.

Acknowledgements

The authors acknowledge the support of the following i3S Scientific Platforms: Animal Facility, Cell Culture and Genotyping (CCGen), Translational Cytometry Unit (TraCy), BioSciences Screening (BS) and Advanced Light Microscopy (ALM), members of the national infrastructure PPBI-Portuguese Platform of BioImaging (supported by POCI-01–0145-FEDER-022122).

FEDER and FCT, Portugal (Norte-01-0145-FEDER-000008000008—Porto Neurosciences and Neurologic Disease Research Initiative at I3S, supported by Norte Portugal Regional Operational Programme (NORTE 2020), under the PORTUGAL 2020 Partnership Agreement, through the European Regional Development Fund (ERDF); FCOMP-01-0124-FEDER-021333) supported work in JBR lab.

FCT Portugal, PEst (UID/NEU/04539/2013), COMPETE-FEDER (POCI-01-0145-FEDER-007440) and Centro 2020 Regional Operational Programme (CENTRO-01-0145-FEDER-000008: BrainHealth 2020) supported work in AFA lab.

CCP and RS hold employment contracts financed by national funds through FCT – Fundação para a Ciência e a Tecnologia, I.P., in the context of the program-contract described in paragraphs 4, 5 and 6 of art. 23 of Law no. 57/2016, of August 29th, as amended by Law no. 57/2017 of July 19th. RPC is a research fellow from CNPq and Faperj (Brazil). TC is supported by an FCT grant (SFRH/BD/117148/2016). RLA is supported by an FCT grant (PD/BD/114266/2016). AM was supported by FCT (IF/00753/2014 and CP1244/CT0005). TS was supported by FCT (IF/00875/2012). FIB and SHV hold postdoctoral fellowships from FCT (SFRH/BPD/86830/2012 and SFRH/BPD/81627/2011, respectively). Authors declare no conflict of interest.

Figure legends

Figure 1. Rhoa is required for microglia survival and its ablation triggers spontaneous microglia activation.

A, expression of Rhoa in microglia from the brains of Rhoa$^{fl/fl}$ and Rhoa$^{fl/fl}$:Cx3cr1^{CreER+} mice 35-45 days after TAM administration (n=4 animals per genotype). Graphs (mean and SEM) depict Rhoa^{+} microglia and microglial Rhoa MFI. Cell debris was excluded by size. *P<0.05 (Mann-Whitney test).

B, histological confocal analysis for Iba1 on tissue sections for the indicated brain regions from Rhoa$^{fl/fl}$ and Rhoa$^{fl/fl}$:Cx3cr1^{CreER+} mice 35-45 days after TAM administration (n=9-11 animals). Graph (mean and SEM) depicting Iba1^{+} cells for each genotype is shown. *P<0.05 (unpaired t test). Scale bars: 50 μm.

C, Flow cytometry analysis of microglial numbers and cell death in Rhoa$^{fl/fl}$ and Rhoa$^{fl/fl}$:Cx3cr1^{CreER+} mice 35-45 days after TAM administration (n=7-9 animals). Graphs show microglia cell counts (mean and SEM). Cell debris was excluded by size. *P<0.05 (Mann-Whitney test).

D, Flow cytometry analysis of cell death markers in microglia from Rhoa$^{fl/fl}$ and Rhoa$^{fl/fl}$:Cx3cr1^{CreER+} mice 150 days after TAM administration (n=5 animals per genotype). Graphs show necrotic and apoptotic microglia (mean and SEM). Cell debris was excluded by size. *P<0.05 (Mann-Whitney test).

E, histological confocal analysis for Iba1 on tissue sections from the neocortex of Rhoa$^{fl/fl}$ and Rhoa$^{fl/fl}$:Cx3cr1^{CreER+} mice 35-45 days after TAM administration (n=3-5 animals for each time point). Graph (mean and SEM) depicting Sholl analysis for each genotype is shown. *P<0.05 (Two-way ANOVA comparing Rhoa$^{fl/fl}$ vs. Rhoa$^{fl/fl}$:Cx3cr1^{CreER+} for each distance). Scale bar: 20 μm.

F, qRT-PCR in microglia sorted from brains of Rhoa$^{fl/fl}$ and Rhoa$^{fl/fl}$:Cx3cr1^{CreER+} mice 35-45 days after TAM administration (n=4 animals). Graphs (means and SEM) show the mRNA expression for the indicated transcripts. *P<0.05 (Mann-Whitney test) vs. Rhoa$^{fl/fl}$.

G, Tnf amounts in brains of Rhoa$^{fl/fl}$ and Rhoa$^{fl/fl}$:Cx3cr1^{CreER+} mice 35-45 days after TAM administration (n=8-11 animals). Graphs (means and SEM) show Tnf amounts determined by ELISA. *P<0.05 (unpaired t test).

Figure 2. Rhoa deficiency in adult microglia leads to phenotypic features underlying neurological disorders.

A, primary cortical microglial cultures expressing a glutamate release FRET biosensor (FLIPE^{600nSurface}) were transduced with pLKO (CT) or Rhoa shRNA (Rhoa KD) lentiviruses (n=11-15 cells pooled across 3 different cultures). Graph (means and SEM) displays time-lapse CFP/FRET ratio images averaged for 10 min. *P<0.05 (Mann-Whitney test).

B, Extracellular glutamate was measured in the culture media from pLKO (CT) and Rhoa KD microglia (n=3 different cultures). Graph (means and SEM) displays glutamate content accumulated in the culture media. fau = fluorescence arbitrary units. *P<0.05 (Mann-Whitney test).

C, primary hippocampal neuronal cultures expressing the yellow fluorescent protein variant mVenus were incubated for 24 h with conditioned media from microglial cultures (MCM) obtained from WT mice that were previously infected with pLKO (CT) or Rhoa shRNA (Rhoa KD) lentiviruses (n=3 different cultures). In some conditions neurons were co-incubated with the NMDA receptor antagonist kynurenic acid (KyA; 1 μM). Graph (means and SEM) displays the number of mVenus^{+} neurons with beaded neurites over the total number of mVenus^{+} neurons. Arrowheads display a typical beaded neurite. *P<0.05 vs CT (MCM), #P<0.05 vs. Rhoa KD (MCM) (One-way ANOVA). Scale bar: 50 μm.

D, histological confocal analysis of Rhoa$^{fl/fl}$ and Rhoa$^{fl/fl}$:Cx3cr1^{CreER+} mice 35-45 days after TAM administration (n=6 animals per genotype). vGlut-1 (green) and PSD-95 (red) immunolabeling on tissue sections from the hippocampus CA1 region is shown. Graph (mean and SEM) depicts vGlut-1^{+}PSD-95^{+} colocalization puncta normalized to the Rhoa^{flfl} values. *P<0.05 (Mann-Whitney test). Scale bars: 5 μm and 1 μm (high mag). White asterisks denote synaptic puncta (yellow).

E, Western blot for PSD-95 and vGlut-1 on lysates from the brains of Rhoa$^{fl/fl}$ and Rhoa$^{fl/fl}$:Cx3cr1^{CreER+} mice 35-45 days after TAM administration (n=5 animals per genotype). GAPDH was used as the loading control. *P<0.05 (Mann-Whitney test).

F and G, panel (F) shows the averaged time course changes in field excitatory post-synaptic potential (fEPSP) slope induced by θ-burst stimulation in Rhoa$^{fl/fl}$ and Rhoa$^{fl/fl}$:Cx3cr1^{CreER+} mice 35-45 days after TAM administration (n=9-11 slices from 5-6 animals). Ordinates represent normalized fEPSP slopes, from which 0% corresponds to slopes averaged and recorded for 10 min before θ-burst stimulation ((-0.99±0.04 mV/ms (Rhoa^{flfl}), −0.93±0.04 mV/ms (Rhoa$^{fl/fl}$:Cx3cr1^{CreER+})), and the abscissa represents the time that average begun. Experiments are the average of six consecutive responses obtained for Rhoa$^{fl/fl}$ or Rhoa$^{fl/fl}$:Cx3cr1^{CreER+} mice before (1 or 3) and 58-60 min after (2 or 4) θ-burst stimulation, and is composed by the stimulus artifact, followed by the pre-synaptic fiber volley and the fEPSP. Panel (G) compares the magnitude of LTP obtained in slices from each genotype, as indicated below each bar; the values in ordinates represent the average of the fEPSP recorded 50-60 min after LTP induction, normalized to pre θ-burst stimulation values. All values are presented as mean and SEM. *P<0.05 (unpaired t test).

H, histological confocal analysis of Rhoa$^{fl/fl}$ and Rhoa$^{fl/fl}$:Cx3cr1^{CreER+} mice 35-45 days after TAM administration (n=8 animals per genotype in TUNEL and 6 animals per genotype in NeuN). TUNEL (red) and NeuN (cyan) immunolabeling on tissue sections from the hippocampus CA1 region are shown. Graphs (mean and SEM) depict TUNEL^{+} or NeuN^{+} cells per mm^{2}. *P<0.05 (unpaired t test). Scale bars: 100 μm.

I, Rhoa$^{fl/fl}$ and Rhoa$^{fl/fl}$:Cx3cr1^{CreER+} were evaluated in the NOR test 35-45 days after TAM administration (n=9 animals). Rhoa$^{fl/fl}$:Cx3cr1^{CreER+} mice spent more time exploring the novel object than the familiar object, whereas Rhoa$^{fl/fl}$ animals preferred exploring the novel object, reflecting a clear difference in the discrimination index between the

genotypes. Total exploration time was similar between genotypes. Graphs (means and SEM) display the NOR parameters after a 4 h delay. *P<0.05 (unpaired t test).

Figure 3. Loss of Rhoa in adult microglia leads to Src hyperactivation through Csk.

A, Western blot for Src pTyr^{416} on lysates from MACS-separated microglia collected from the brains of Rhoa$^{fl/fl}$ and Rhoa$^{fl/fl}$:Cx3cr1^{CreER+} mice 90 days after TAM administration (n=3 mice per genotype). Src was the loading control. *P<0.05 (Mann-Whitney test)

B, Western blot for Src pTyr^{416} on lysates from control (CT) or Rhoa shRNA (Rhoa KD) stable N9 microglial cell sub-clones (n=3 different cultures). Src was used as the loading control. Graphs (means and SEM) display Src pTyr^{416}/Src ratio normalized to the CT values. *P<0.05 (Mann-Whitney test).

C, CHME3 microglial cultures expressing the Src FRET biosensor (KRas Src YPet) were transduced with pLKO (CT) or Rhoa shRNA (Rhoa KD) lentiviruses (n=16-18 cells pooled across 3 different cultures). Graph (means and SEM) displays time-lapse CFP/FRET ratio images averaged for 10 min. Pseudocolor ramps represent min/max CFP/FRET ratios. *P<0.05 (Mann-Whitney test). Scale bar: 5 µm.

D, schematic representation of pSicoR vector-dependent knockdown of Rhoa (active pSicoR). Rhoa re-expression (inactive pSicoR) is achieved after Cre-dependent recombination of loxP sites.

E, Western blots for Src pTyr^{416} on lysates from CHME3 microglial cells transduced with lentiviruses carrying pSicoR with a scrambled sequence (lox-scramble-lox) or Rhoa shRNA (lox-shRhoa-lox) (n=3-4 different cultures). In some conditions cells were transfected with an empty vector (lenti-CT) or with a Cre recombinase-expressing vector (lenti-Cre). Src was used as the loading control. Graphs (means and SEM) display Src pTyr^{416}/Src ratio normalized to CT (lox-scramble-lox) values. *P<0.05 (Kruskal-Wallis test) vs. CT (lox-scramble-lox); $^{\#}$P<0.05 (Kruskal-Wallis test) vs. CT (lox-shRhoa-lox).

F, qRT-PCR on sorted brain microglia from of Cx3cr1^{CreER+} and Rhoa$^{fl/fl}$:Cx3cr1^{CreER+} mice 35-45 days after TAM administration (n=3-4 animals). Graphs (means and SEM) show the mRNA expression levels for Csk. *P<0.05 (Mann-Whitney test).

G, Western blot for Csk on lysates from control (CT) or Rhoa shRNA (Rhoa KD) stable N9 microglial cell sub-clones (n=3 different cultures). Actin was used as the loading control. Graphs (means and SEM) display Csk/Actin ratio normalized to the CT values. *P<0.05 (Mann-Whitney test).

H, Western blot for Csk or Src pTyr^{416} on lysates from CHME3 microglial cells transfected with the Rhoa^{Q63L} mutant. Actin and Src were the loading controls (n=3 different cultures). Graphs (means and SEM) display Csk/actin and Src pTyr^{416}/Src ratios normalized to the CTs values. *P<0.05 (Mann-Whitney test).

I, schematic representation of Rhoa activation using chemical-inducible dimerization (CID). **J**, Western blot for Src pTyr^{416} on lysates from pLKO or Csk shRNA (Csk KD) stable CHME3 microglial cell sub-clones (n=3-5 different cultures). In some conditions cells were co-transfected with YFP-FKBP and Lyn$_{11}$-FRB (CT-CID) or with YFP-FKBP-Rhoa (CA) and Lyn$_{11}$-FRB (Rhoa-CID). All groups were treated with 500 nM rapamycin for 24 h. Src was used as the loading control. Graphs (means and SEM) display Src pTyr^{416}/Src ratio normalized to the CT values. *P<0.05 (Kruskal-Wallis test) vs. CT-CID (pLKO).

K and L, confocal imaging of p65-GFP-transfected (green; K) pLKO (CT), Csk KD or Src^{Y527F} stable N9 microglial cell sub-clones. Nuclei were stained with DAPI (blue). Tnf amounts (ELISA; L) were determined from the culture supernatant. Graphs are mean and SEM (n=3-4 different cultures). *P<0.05 (Kruskal-Wallis test) vs. CTs. Scale bar: 10 μm.

Figure 4. Src inhibition compensates Rhoa deficiency in microglia preventing synapse loss and memory deficits.

A, regimen of 10 mg/kg AZD 0530 or DMSO injections to Rhoa$^{fl/fl}$:Cx3cr1^{CreER+} mice after TAM administration.

B, Western blot for Src pTyr^{416} on lysates from the brains of Rhoa$^{fl/fl}$:Cx3cr1^{CreER+} mice injected with 10 mg/kg AZD 0530 (one IP per week over 4 weeks) or DMSO (n=6 animals per group). Src was used as the loading control.

C, FACS analysis of microglia in Rhoa$^{fl/fl}$ and Rhoa$^{fl/fl}$:Cx3cr1^{CreER+} mice injected with 10 mg/kg AZD 0530 (one IP per week over 4 weeks) or DMSO (n=5-7 animals). Graphs depict microglia cell counts (mean and SEM). *P<0.05 (Kruskal-Wallis test) vs. Rhoa^{flfl} - DMSO; $^{\#}$P<0.05 (Kruskal-Wallis test) vs. Rhoa$^{fl/fl}$:Cx3cr1^{CreER+} - DMSO.

D, histological confocal analysis of Rhoa$^{fl/fl}$ and Rhoa$^{fl/fl}$:Cx3cr1^{CreER+} mice injected with 10 mg/kg AZD 0530 (one IP per week over 4 weeks) or DMSO (n=6-7 animals). Iba1 immunolabeling on tissue sections from the hippocampal dentate gyrus. Graph (mean and SEM) depicts Iba1 positive cells per mm^2. *P<0.05 (Kruskal-Wallis test) vs. Rhoa$^{fl/fl}$ - DMSO; #P<0.05 (Kruskal-Wallis test) vs. Rhoa$^{fl/fl}$:Cx3cr1^{CreER+} - DMSO.

E, qRT-PCR from the neocortex of Rhoa$^{fl/fl}$ and Rhoa$^{fl/fl}$:Cx3cr1^{CreER+} mice injected with 10 mg/kg AZD 0530 (one IP per week over 4 weeks) or DMSO (n=6-9 animals). Graphs (means and SEM) show the transcript abundance for Tnf normalized to Rhoa$^{fl/fl}$ – DMSO values. *P<0.05 (Kruskal-Wallis test) vs. Rhoa$^{fl/fl}$ - DMSO; $^{\#}$P<0.05 (Kruskal-Wallis test) vs. Rhoa$^{fl/fl}$:Cx3cr1^{CreER+} - DMSO.

F, Tnf amounts (ELISA) determined from the culture supernatant of pLKO (CT), Rhoa KD or Rhoa KD:Src^{Y416F}, Csk KD or Csk KD treated with SKI-1 (500 nM; 24 h) stable N9 microglial cell sub-clones. Graph is mean and SEM (n=4-7 different cultures). *P<0.05 (Kruskal-Wallis test) vs. CT; $^{\#}$P<0.05 (Kruskal-Wallis test) vs. Rhoa KD; $^{\&}$P<0.05 (Kruskal-Wallis test) vs. Csk KD.

G, primary microglia from WT or Tnf KO mice were infected with pLKO (CT), Rhoa KD lentiviruses and then transfected with the glutamate release FRET biosensor FLIPE (n=15-32 cells pooled across 3 different cultures). Graph (means and SEM) displays time-lapse CFP/FRET ratio images averaged for 10 min. *P<0.05 (Kruskal-Wallis test) vs. CT; $^{\#}$P<0.05 (Kruskal-Wallis test) vs. Rhoa KD.

H, CHME3 microglial cells expressing the glutamate release FRET biosensor FLIPE were treated with different concentrations of recombinant Tnf (n=6 cells for each condition pooled across 2 different cultures). Graph (means and SEM) displays time-lapse CFP/FRET ratio images averaged for 30 min. Blue line represents baseline glutamate release without stimulation with Tnf.

I, CHME3 microglial cells were co-transfected with the $Rhoa^{WT}$ or $Rhoa^{T19N}$ and the glutamate release FRET biosensor FLIPE (n=15-20 cells pooled across 2 different cultures). In some conditions $Rhoa^{T19N}$ cells were treated with Adalimumab (α-Tnf; 5 µg/ml; 48 h). Graph (means and SEM) displays time-lapse CFP/FRET ratio images averaged for 10 min. *P<0.05 (Fisher´s LSD test) vs. $Rhoa^{WT}$; $^{\#}$P<0.05 (Fisher´s LSD test) vs. $Rhoa^{T19N}$.

J, pLKO (CT), Rhoa KD, Csk KD or Src^{Y527F} CHME3 microglial cell sub-clones were transfected with the glutamate release FRET biosensor FLIPE (n=8-15 cells pooled across 3 different cultures). In some conditions Rhoa KD cells were treated with the Src inhibitor SKI-1 (500 nM; 24 h), the inhibitor of Tnf production pomalidomide (POM; 500 nM; 24 h), recombinant Tnf (30 pg/ml; 24 h) or the gap junction blocker 18-alpha- glycyrrhetinic acid (10 µM; 24 h). Graph (means and SEM) displays time-lapse CFP/FRET ratio images averaged for 10 min. *P<0.05 (Kruskal-Wallis test) vs. CT; $^{\#}$P<0.05 (Kruskal-Wallis test) vs. Rhoa KD; †P<0.05 (Kruskal-Wallis test) vs. Rhoa KD + SKI-1; ‡P<0.05 (Kruskal-Wallis test) vs. Rhoa KD + POM.

K, CHME3 microglial cells expressing the glutamate release FRET biosensor FLIPE were co-transfected with pLKO (CT) or Rhoa^{Q63L} together with RapR-Src and FRB-mCherry (n=8-9 cells pooled across 3 different cultures). All groups were treated with 500 nM rapamycin for 90 min. Graph (means and SEM) displays time-lapse CFP/FRET ratio images averaged for 30 min. *P<0.05 (Kruskal-Wallis test) vs. CT; $^{\#}$P<0.05 (Kruskal-Wallis test) vs. Rhoa^{Q63L}.

L, extracellular glutamate was measured in the culture media from pLKO (CT), Rhoa KD, Csk KD or Src^{Y527F} N9 microglial cell sub-clones (n=4-7 different cultures). In some conditions Rhoa KD cells were treated with the Src inhibitor SKI-1 (500 nM; 24 h). Graph (means and SEM) displays glutamate content accumulated in the culture media. fau = fluorescence arbitrary units. *P<0.05 (Kruskal-Wallis test) vs. CT; $^{\#}$P<0.05 (Kruskal-Wallis test) vs. Rhoa KD.

M, primary hippocampal neuronal cultures expressing the yellow fluorescent protein variant mVenus were incubated for 24 h with MCM obtained from WT cortical microglia infected with CT or Rhoa KD lentiviruses or Tnf KO cortical microglia infected with Rhoa KD lentiviruses (n=3 different cultures). Graph (means and SEM) displays the number of mVenus^{+} neurons with beaded neurites over the total number of mVenus^{+} neurons. *P<0.05 (Kruskal-Wallis test) vs. WT - CT (MCM); $^{\#}$P<0.05 (Kruskal-Wallis test) vs. WT - Rhoa KD (MCM).

N, primary hippocampal neuronal cultures expressing the yellow fluorescent protein variant mVenus were incubated for 24 h with MCM obtained from pLKO (CT), Rhoa KD, and RhoA KD + Src^{Y416F} N9 microglial cell sub-clones (n=3 different cultures). In some conditions Rhoa KD microglia were treated with SKI-1 (500 nM; 24 h) or pomalidomide (POM; 500 nM; 24 h). Recombinant Tnf (30 pg/ml; 24 h) was used in CT microglial clones. Graph (means and SEM) displays the number of mVenus^{+} neurons with beaded neurites over the total number of mVenus^{+} neurons. *P<0.05 (Kruskal-Wallis test) vs. CT (MCM);

$^{\#}$P<0.05 (Kruskal-Wallis test) vs. Rhoa KD (MCM); †P<0.05 (Kruskal-Wallis test) vs. Rhoa KD + POM.

O, vGlut-1 (green) and PSD-95 (red) immunolabelling in primary hippocampal neurons incubated for 24 h with conditioned media from microglial cultures (MCM) overexpressing Rhoa^{WT}, Rhoa^{T19N} or Src^{Y416F} (n=20 neurites per group pooled from 2 different cultures). In some conditions microglial cultures were pre-incubated with Adalimumab (α-Tnf; 5 µg/ml; 48 h). Graph (mean and SEM) depicts vGlut-1^{+}PSD-95^{+} colocalization puncta normalized to Rhoa^{WT} values. *P<0.01 vs. Rhoa^{WT} (MCM), #P<0.05 vs. Rhoa^{T19N} (MCM), †P<0.01 vs. Rhoa^{T19N} (MCM) (One-way ANOVA). Scale bar: 5 µm.

P, histological confocal analysis of Rhoa$^{fl/fl}$ and Rhoa$^{fl/fl}$:Cx3cr1^{CreER+} mice injected with 10 mg/kg AZD 0530 (one IP per week over 4 weeks) or DMSO (n=6-7 animals). vGlut-1 (green) and PSD-95 (red) immunolabeling on tissue sections from the hippocampal CA1 region is shown. Graph (mean and SEM) depicts vGlut-1^{+}PSD-95^{+} colocalization puncta normalized to the Rhoa$^{fl/fl}$ - DMSO values. *P<0.05 (Kruskal-Wallis test) vs. Rhoa$^{fl/fl}$ - DMSO; #P<0.05 (Kruskal-Wallis test) vs. Rhoa$^{fl/fl}$:Cx3cr1^{CreER+} - DMSO. Scale bar: 5 µm. Asterisks denote synaptic puncta (yellow).

Q, DMSO and AZD 0530-injected Rhoa$^{fl/fl}$ or Rhoa$^{fl/fl\ l}$:Cx3cr1^{CreER+} mice were evaluated in the NOR test (n=10-11 animals). AZD-injected Rhoa$^{fl/fl}$:Cx3cr1^{CreER+} mice performed the NOR test substantially better than DMSO-injected Rhoa$^{fl/fl}$:Cx3cr1^{CreER+} mice. AZD-injected Rhoa$^{fl/fl}$:Cx3cr1^{CreER+} animals also explored more the novel object. Graphs (means and SEM) display the NOR parameters after a 4 h delay. *P<0.05 (One-way ANOVA) vs. Rhoa$^{fl/fl}$ - DMSO; $^{\#}$P<0.05 (One-way ANOVA) vs. Rhoa$^{fl/fl}$:Cx3cr1^{CreER+} - DMSO.

Figure 5. Loss of Rhoa in adult microglia produces an amyloid-like pathology.

A, histological confocal analysis of Rhoa$^{fl/fl}$ and Rhoa$^{fl/fl}$:Cx3cr1^{CreER+} mice 50 days after TAM administration (n=7 animals per genotype for BAM-10 and 10 animals per genotype for M3.2). Aβ deposits (M3.2 or BAM-10; green) on tissue sections from the neocortex and hippocampal CA1 region are shown. Graph (mean and SEM) depicts the fraction of Aβ fluorescence area normalized to Rhoa^{flfl}. *P<0.05 (unpaired t test). Scale bars: 100 μm.

B, Western blot using M3.2 antibody (detecting APP and β-CTF) on lysates from the brains of Rhoa$^{fl/fl}$ and Rhoa$^{fl/fl}$:Cx3cr1^{CreER+} mice 50 days after TAM administration (n=7-14 animals). GAPDH was used as the loading control. *P<0.05 (unpaired t test).

C, Quantification of the amounts of $A\beta_{1-40}$ and $A\beta_{1-42}$ in the neocortex of RhoA$^{fl/fl}$ and RhoA$^{fl/fl}$:Cx3cr1^{CreER+} mice 50 days after TAM administration (n=14-16 animals for $A\beta_{1-40}$ and n=10-11 animals for $A\beta_{1-42}$). Graphs (mean and SEM) show Aβ amounts normalized for protein amounts of the tissue extracts. *P<0.05 (unpaired t test vs. RhoA$^{fl/fl}$).

D, histological confocal analysis of methoxy-X04 positive plaque-like deposits on neocortical sections from RhoA$^{fl/fl}$ and RhoA$^{fl/fl}$:Cx3cr1^{CreER+} mice 50 days after TAM administration (n=5 animals per group). Graph (mean and SEM) show the quantification of the size of plaque-like deposits and the percent area occupied by plaque-like deposits (plaque load).

E, Intracellular endogenous Aβ42 (immunolabelled with anti-Aβ42 clone 12F4) and CellMask dye (cyan) in primary hippocampal neurons incubated for 24 h with conditioned media from microglial cultures (MCM) overexpressing Rhoa^{WT}, Rhoa^{T19N} or Src^{Y416F} (n=2 different cultures). In some conditions microglial cultures were pre-incubated with Adalimumab (α-Tnf; 5 μg/ml; 48 h). Graph (means and SEM) displays Aβ42 fluorescence normalized to Rhoa^{WT} values. *P<0.001 vs Rhoa^{WT} (MCM), #P<0.01 vs. Rhoa^{T19N} (MCM), †P<0.01 vs. Rhoa^{T19N} (MCM) (One-way ANOVA). Scale bar: 20 μm.

F, flow cytometry showing expression of GTP-Rhoa, Csk or Src pTyr^{416} in microglia (gated using CD45^{mid}CD11b^{+}) from 4-month-old WT and APP/PS1 mice (n=3-4 animals). Graphs are mean with SEM. *P<0.05 (Mann-Whitney test).

G, CHME3 microglia expressing a RhoA FRET activity biosensor were recorded in saline before (t=0 min) and after treatment with 200 nM Aβ_{1-42} oligomers. Graph (mean and SEM) show time-lapse FRET/Donor ratio change (n=20 cells pooled across 3 different experiments). *p<0.001 (Two-Way ANOVA vs. 0 min).

H, CHME3 microglia expressing a Src FRET activity biosensor were transfected with RhoA^{Q63L} and then recorded in saline before (t=0 min) and after treatment with 200 nM Aβ_{1-42} oligomers. Graph (mean and SEM) show time-lapse Donor/FRET ratio change images (n=19-23 cells pooled across 3 different experiments). *p<0.01 (Two-Way ANOVA vs. Mock 0 min); #p<0.001 (Two-Way ANOVA vs. Mock 20 or 30 min).

I and J, CHME3 microglia expressing a NFkB pathway activity biosensor (I) or a glutamate release FRET biosensor (J) were either transfected with RhoA^{Q63L} or incubated with AZD 0530 (200 nM; 1 h) or pre-incubated with Adalimumab (α-Tnf; 5 µg/ml; 48 h) and then recorded in saline before (t=0 min) and after treatment with 200 nM Aβ_{1-42} oligomers. Graphs (mean and SEM) show time-lapse 1/(F-F0) fluorescence change (I) or Donor/FRET ratio change (J). (n=23-39 (I) or 25-40 (J) cells pooled across3 different experiments). *p<0.001 (Two-Way ANOVA vs. Mock 0 min); #p<0.001 (Two-Way ANOVA vs. Mock 20 or 30 min); †p<0.01 (Two-Way ANOVA vs. Mock 20 or 30 min); ‡p<0.01 (Two-Way ANOVA vs. Mock 20 or 30 min).

Figure 6. Src inhibition mitigates the amyloid-like pathology elicited by the loss of Rhoa in adult microglia.

A, CHME3 microglia were co-transfected with YFP-FKBP and Lyn_{11}-FRB (CT-CID; n=395 cells polled across 3 different experiments) or with YFP-FKBP-Rhoa (CA) and Lyn_{11}-FRB (Rhoa-CID; n=211 cells polled across 3 different experiments). All cells were treated with $A\beta_{1-42}$ fluorescent particles (10 µg/ml) and rapamycin (500 nM) for 90 min. Graph (means and SEM) displays $A\beta_{1-42}$ levels per cell normalized to the CT-CID values. *P<0.05 (unpaired t test).

B, CHME3 microglia were treated with DMSO (n=113 cells polled across 3 different experiments) or AZD 0530 (n=89 cells polled across 3 different experiments) and incubated with $A\beta_{1-42}$ fluorescent particles (10 µg/ml) for 90 min. Graph (means and SEM) displays $A\beta_{1-42}$ levels per cell (stained with CellMask dye; green) normalized to the DMSO values. *P<0.05 (unpaired t test).

C, histological confocal analysis showing colocalization (white) of $Iba1^{+}$ microglia (magenta) with M3.2 immunoreactive amyloid deposits (green) on tissue sections from $Rhoa^{fl/fl}$:$Cx3cr1^{CreER+}$ mice (hippocampus) injected with 10 mg/kg AZD 0530 (one IP per week over 4 weeks) or DMSO MSO (n=8 animals per group). Graphs (mean and SEM) show the % area of M3.2 fluorescence channel colocalized with Iba1. *P<0.05 (Mann-Whitney test vs. $Rhoa^{fl/fl}$:$Cx3cr1^{CreER+}$ - DMSO). Scale bars: 10 µm.

D, histological confocal analysis showing M3.2 immunoreactive amyloid deposits (green) on tissue sections from $Rhoa^{fl/fl}$:$Cx3cr1^{CreER+}$ mice injected with 10 mg/kg AZD 0530 (one IP per week over 4 weeks) or DMSO (n=10 animals per group). Graphs (mean and SEM) show the quantification of area occupied by M3.2 immunoreactive deposits (Aβ load) normalized to $Rhoa^{fl/fl}$:$Cx3cr1^{CreER+}$ – DMSO. *P<0.05 (Mann-Whitney test vs. $Rhoa^{fl/fl}$:$Cx3cr1^{CreER+}$ - DMSO). Scale bars: 200 µm.

E, Quantification of the amounts of $A\beta_{1-40}$ and $A\beta_{1-42}$ in the neocortex of $RhoA^{fl/fl}$:$Cx3cr1^{CreER+}$ mice injected with 10 mg/kg AZD 0530 (one IP per week over 4 weeks) or DMSO (n=8-21 animals for $A\beta_{1-40}$ and n=8-14 animals for $A\beta_{1-42}$). Graphs (mean and SEM) show $A\beta_{1-42}$ amounts normalized for protein amounts of the tissue extract. *P<0.05 (unpaired t test vs. $RhoA^{fl/fl}$:$Cx3cr1^{CreER+}$ - DMSO).

F, histological confocal analysis of methoxy-X04 positive plaque-like deposits on tissue sections from $RhoA^{fl/fl}$:$Cx3cr1^{CreER+}$ mice (neocortex) injected with with 20 mg/kg AZD 0530 (one IP per week over 4 weeks) or DMSO (n=5 animals per group). Graph (mean and SEM) show the quantification of the size of plaque-like deposits and the percent area occupied by plaque-like deposits (plaque load). *P<0.05 (Mann-Whitney test vs. $RhoA^{fl/fl}$:$Cx3cr1^{CreER+}$ - DMSO). Scale bar: 50 µm.

STAR Methods

LEAD CONTACT AND MATERIALS AVAILABILITY

Further information and requests for resources and reagents should be directed to the Lead Contact, João Relvas (jbrelvas@ibmc.up.pt) and are available upon reasonable justification.

EXPERIMENTAL MODEL AND SUBJECT DETAILS

Animals: All mice experiments were reviewed by i3S animal ethical committee and were approved by Direção-Geral de Alimentação e Veterinária (DGAV). Animals were maintained in standard laboratory conditions with inverted 12h/12h light dark cycle and were allowed free access to food and water. Animals were group-housed under specific pathogen-free conditions. Experiments were carried out following the 3Rs ethics and mice were kept on a C57BL/6 background.

Conditional Rhoa-deficient mice: All mice experiments were approved by Direção-Geral de Alimentação e Veterinária (DGAV). Cx3cr1$^{CreER\text{-}EYFP}$ mice were purchased from Jackson Laboratories. In such mice, the *Cx3cr1* promoter drives high expression of the CreER cassette in microglia (Parkhurst et al., 2013). Mice homozygous for the *Rhoa* floxed allele (Herzog et al., 2011, Jackson et al., 2011) were backcrossed at least for 10 generations and were kept at the I3S animal facility. All genotypes were determined by PCR on genomic DNA. Primers used for Rhoa floxed alleles were: AGC CAG CCT CTT GAC CGA TTT A (forward); TGT GGG ATA CCG TTT GAG CAT (reverse). Primers for CreER insertion were: AAG ACT CAC GTG GAC CTG CT (WT forward); AGG ATG TTG ACT TCC GAG TG (WT reverse); CGG TTA TTC AAC TTG CAC CA (mutant reverse).

Rhoa floxed mice were crossed with Cx3cr1$^{CreER\text{-}EYFP}$ mice. Progeny of interest were: Control (Rhoa$^{fl/fl}$) and mutants (Rhoa$^{fl/fl}$:Cx3cr1^{CreER+}). Mice were given tamoxifen (10 mg *per* animal by oral gavage) at P26 and P28 and then analyzed at different time points. All experiments were performed on mice kept on a C57Bl/6 background. For electrophysiological recordings and in behavioral tests only male Rhoa$^{fl/fl}$, Cx3cr1^{CreER+} and Rhoa$^{fl/fl}$:Cx3cr1^{CreER+} littermates were used. No differences in the mRNA expression levels of Rhoa were found in FACS-sorted microglia between the brains of Rhoa$^{fl/fl\,-}$ and wild-type mice after TAM administration. In addition, after TAM administration, Rhoa$^{fl/fl}$ mice

displayed no overt difference in the behavioral performance on motor, anxiety-related and memory tests when compared to wild-type mice. Administration of AZD 0530 (used at a final concentration of 10 mg/kg via IP injections; 1 IP per week lasting 4 weeks) to Rhoa$^{fl/fl}$:Cx3cr1^{CreER+} and Rhoa$^{fl/fl}$ mice started 1 week after the second TAM pulse. Administration of pomalidomide (used at a final concentration of 50 mg/kg via IP injections; 3 IPs per week lasting 4 weeks) to Rhoa$^{fl/fl}$:Cx3cr1^{CreER+} and Cx3cr1^{CreER+} mice started 1 week after the second TAM pulse.

Tnf deficient mice: Prof. Rui Applelberg (University of Porto) supplied C57BL/6.Tnf knockout (referred herein as Tnf KO) mice. Tnf KO mice were genotyped by PCR using ATC CGC GAC GTG GAA CTG GCA GAA (forward) and CTG CCC GGA CTC CGC AAA GTC TAA (reverse) primer pair. Tnf KO mice display a single band of 2 kb in the PCR gel. Mice were bred at i3S animal facility. Tnf KO animals were bred to maintain maximal heterozygosity.

AD mice: The AβPPswe/PS1A246E (termed APP/PS1) AD mice model co-expresses a chimeric mouse-human amyloid-β protein precursor (AβPP) bearing a human Aβ domain with mutations (K595N and M596L) linked to Swedish familial AD pedigrees and human presenilin-1 A246E mutation, with both transgenes under the control of the mouse prion protein promoter (Borchelt et al., 1997). This AD mouse model displays age-dependent and region-specific amyloidosis, gliosis and associated hippocampal-dependent memory deficits, resembling the AD pathology found in human patients (Borchelt et al., 1997). APP/PS1 mice were genotyped by PCR using PSEN primers: AAT AGA GAA CGG CAG GAG CA (forward) and GCC ATG AGG GCA CTA ATC AT (reverse); APP primers: GAC TGA CCA CTC GAC CAG GTT CTG (forward) and CTT GTA AGT TGG ATT CTC ATA TCC G (reverse); WT primers: CCT CTT TGT GAC TAT

GGT GAC TGA TGT CGG (forward) and GTG GAT AAC CCC TCC CCC AGC CTA GAC C (reverse). APP/PS1 mice were maintained in SV129 background and were bred at the i3S animal facility. Administration of AZD 0530 (used at a final concentration of 20 mg/kg via IP injections; 1 IP per week lasting 4 weeks) to APP/PS1 mice started when animals completed 3 months of age.

Primary cultures of hippocampal neurons: Hippocampi were dissected from embryonic day 18 Wistar rat embryos and dissociated using trypsin (0.25%, v/v). Neurons were plated at a final density of 1×10^4 to 5×10^4 cells per dish and cultured in the presence of a glial feeder layer. Cells were cultured in Neurobasal medium supplemented with B27 supplement (1:50, v/v), 25 mM glutamate, 0.5 mM glutamine, and gentamicin (0.12 mg/ml). To prevent glial overgrowth, neuronal cultures were treated with 5 mM cytosine arabinoside after 3 days in vitro (DIV) and maintained in a humidified incubator with 5% CO_2/95% air at 37°C for up to 2 weeks, feeding the cells once per week by replacing one-third of the medium. To assess neurite beading, hippocampal neurons expressing mVenus were observed under a fluorescence microscope after 24 h of incubation with 50% (v/v) microglia conditioned media. Neurons were observed blindly in three independent hippocampal cultures. The ratio of bead-bearing mVenus$^+$ neurons was calculated over the total mVenus$^+$ neurons counted.

Primary cultures of cortical microglia: Primary cortical microglial cell cultures were performed as previously described (Socodato et al., 2015a, Socodato et al., 2015b, Portugal et al., 2017). In brief, mice pups (2-day-old) were sacrificed, their cerebral cortices were dissected in HBSS, pH 7.2, and digested with 0.07% trypsin plus 50 µL (w/v) DNAse for 15 min. Next, cells were gently dissociated using a glass pipette in DMEM F12 GlutaMAX™-I supplemented with 10% FBS, 0.1% gentamicin. Cells were plated in poly-

D-lysine-coated T-flasks (75 cm^2) at $1.5x10^6$ cells per cm^2. Cultures were kept at 37°C and 95% air/5% CO_2 in a humidified incubator. Culture media was changed every 3 days up to 21 days. To obtain purified microglial cell cultures, culture flasks were subjected to orbital shaking at 200 rpm for 2 h. Next, culture supernatant was collected to tubes, centrifuged at 453 g for 5 min at room temperature. The supernatant was discarded and the pellet, containing microglia, was re-suspended in culture medium, and cells were seeded in poly-D-lysine-coated 6 or 12-well culture plates at $2.5x10^5$ cells/cm^2 with DMEM F12 GlutaMAX™-I supplemented with 10% FBS, 0.1% gentamicin and 1 ng/ml M-CSF or 1 ng/ml GM-CSF. Purified microglia were cultured for 5-8 days. Immunolabeling with CD11b showed a purity of 95-99% for these cultures.

Microglial cell lines: The microglial cell line N9 was obtained by immortalization of primary cultures from the ventral mesencephalon and cerebral cortex from ED12-13 CD1 mouse embryos with the 3RV retrovirus carrying an activated v-myc oncogene (Righi et al., 1989). Cells were cultured in RPMI 1640 supplemented with 5% FBS, 23.8mM sodium bicarbonate, 30mM D-Glucose, 100 U/mL penicillin and 100 µg/mL streptomycin, and were maintained at 37°C, 95% air and 5% CO_2 in a humidified incubator.

The microglial cell line CHME3 was obtained from primary cultures of human embryonic microglial cells by transfection with a plasmid encoding for the large T antigen of SV40 (Janabi et al., 1995). These cells were cultivated with DMEM GlutaMAX™-I supplemented with 10% FBS and 100 U/mL penicillin and 100 µ/mL streptomycin, and were maintained at 37°C, 95% air and 5% CO_2 in a humidified incubator.

For generation of microglial stable cell sub-clones, N9 or CHME3 cultures were infected with viral particles and allowed to grow for additional 48h. Cultures were then selected using puromycin as before (Socodato et al., 2015b, Portugal et al., 2017). Stable

cell sub-clones carrying an empty vector (pLKO) or the insert of interest were validated by Western blotting or by qRT-PCR.

Primary microglial cells, N9 and CHME3 microglial cell lines were transfected using jetPRIME® (Polyplus Transfection) according to the manufacturer`s protocol.

METHOD DETAILS

Flow cytometry and cell sorting: For characterization of microglia and macrophages in the samples, the following markers were used: CD45-PE, CD11b-APC, CD11b-Alexa Fluor 647, CCR2-PE/Cy7 and Ly6C-PerCP/Cy5.5. Microglial and macrophages were collected from the tissues (brain, blood and spleen) of control and mutant mice using density gradient separation. In brief, mice were anesthetized and then perfused with ice-cold PBS. For single cell suspensions, tissues were quickly dissected, placed on ice-cold RPMI and mechanically homogenized. Cell suspension was passed through a 100 µm cell strainer and centrifuged over a discontinuous 70%/30% Percoll gradient. Cells on the interface were collected, pelleted, washed extensively and then counted in a Neubauer chamber using trypan blue exclusion to estimate the number of live cells. Single cell suspensions (5×10^5 cells) were incubated with different mixes of FACS antibodies for 30 min at 4°C in the dark. Compensation settings were determined using spleen from both control and mutant. Cell suspensions were evaluated on a FACS Canto II analyzer (BD Immunocytometry Systems). For intracellular staining, cell suspensions were run over Percoll gradient, washed and counted as above. Afterwards, cells were seeded in a U bottom 96-well plate and incubated with CD45-PE, CD11b-Alexa Fluor 647 or CD11b-PE/Cy7. After antibody washing, cells were fixed in 2% PFA for 30 min, washed in PBS and permeabilized with permeabilization buffer (Life Technologies 00-8333-56). Intracellular antibody staining mix was prepared in permeabilization buffer and incubated with the cells overnight at 4ºC in the dark. After washing in permeabilization buffer, cells were incubated with Alexa Fluor 488 or 647 secondary antibody for 1 h at 25ºC in the dark. After that, cells were washed twice in permeabilization buffer, washed twice in FACS staining buffer (2% BSA, 0.1% sodium azide in PBS) and analyzed in FACS Canto II. Fluorescence minus one controls for Rhoa, GTP-Rhoa, Csk and phospho-Src were

prepared in mixes with CD45-PE and CD11b-Alexa Fluor 647 CD11b-PE/Cy7 plus secondary antibodies alone. Cell sorting was performed on a FACS ARIA cell sorter. Data were analyzed by FlowJo X10 software (TreeStar).

MACS isolation of adult microglia: Mice were sacrificed in a CO_2 chamber and the brains were removed. The right hemisphere was mechanically dissociated in ice-cold Dounce buffer (15mM HEPES; 0,5% Glucose; and DNAse in PBS) by 6 strokes in a tissue potter. Then, the homogenate was passed through a 70 µm cell strainer, centrifuged and cells were counted in a TC10 Automated Cell Counter from BIO-RAD using Trypan Blue to exclude dead cells. 4 x 10^7 cells were pelleted by centrifugation (9300 g; 1 min; 4ºC) and resuspended in 360 µL of MACS Buffer (0.5% BSA; 2 mM EDTA in PBS) followed by incubation with 40 µL CD11b Microbeads (130-093-634 Miltenyi Biotec). $CD11b^+$ fraction was selected using LS columns (130-042-401 Miltenyi Biotec) in a MACS separator (Miltenyi Biotec) according to the manufacture's instructions. Eluted CD11b enriched fraction was centrifuged (9300 g; 1 min; 4ºC), the pellet was lysed in RIPA-DTT buffer and used for protein isolation.

Brain tissue preparation and immunofluorescence: After animal perfusion with ice-cold PBS (15 ml) and fixation by perfusion with 4% PFA, brains were post-fixed by immersion in 4% PFA in PBS, pH 7.4 overnight. After that, brains were washed with PBS and then cryoprotected using sucrose gradient in a row (15 and 30%). After 24 h, brains were mounted in OCT embedding medium, frozen and cryosectioned in the CM3050S Cryostat (Leica Biosystems). Coronal sections from brains (30 µm thickness between bregma positions 1.0 mm and −2.0 mm) were collected non-sequentially on Superfrost ultra plus slides. Brain sections from control and from mutant mice encompassing identical

stereological regions were collected on the same glass slide. Slides were stored at -20°C until processed for immunohistochemistry.

Frozen sections were defrosted by at least 1 h and hydrated with PBS for 15 min. Sections were permeabilized with 0.25% Triton X-100 for 15 min, washed with PBS for 10 min and blocked (5% BSA, 5% FBS, 0.1% Triton X-100) for 1 h. Primary antibodies were incubated in blocking solution in a humidified chamber overnight at 4°C. Secondary antibodies were incubated for 2 h in blocking solution. After the secondary antibody, sections were washed three times for 10 min with PBS and incubated for 10 min with DAPI and rinsed twice in PBS. Slides were cover slipped using glycergel or Immumount and visualized under a Leica TCS SP5 II confocal microscope.

Image reconstruction and morphometric analysis: Images from tissue sections were acquired using a Leica HC PL APO Lbl. Blue 20x /0.70 IMM/CORR or a Leica HC PL APO CS 40x /1.10 CORR water objective in 8-bit sequential mode using standard TCS mode at 400 Hz and the pinhole was kept at 1 airy in the Leica TCS SP5 II confocal microscope. Images were resolved at 1024 x 1024 pixels format illuminated with 2-5% DPSS561 561 nm wave laser using a HyD detector in the BrightR mode and entire Z-series were acquired from mouse brain sections. Equivalent stereological regions were acquired for all tissue sections within a given slide. Image series were deconvolved using the Hyugens Professional using the Classic Maximum Likelihood Estimation (CMLE) algorithm together with a determined theoretical PSF established using a routine-based implementation for the Hyugens software. Reconstruction and generation of 3D volumes of deconvolved images were performed using the ImageJ 3D viewer plugin and cell counts were performed blinded on integral 3D volume-rendered images. Sholl analyses were performed using an ImageJ Sholl plugin (Ferreira et al., 2014).

All immunostaining in sets of slides were performed together, using the same batch of primary and secondary antibodies, and blocking and washing solutions. Furthermore, images from different sections within a given slide were acquired on the same day, always by the same operator and with identical microscope parameters (e.g., same power for the confocal Argon laser; same laser-line potency; same objective; same fluorescence exposure times and offset for a given fluorophore; same camera binning, zoom and ROI magnification; same pinhole aperture; same pixel size; same line averaging; same TCS scanner mode and speed; same z-stack step size and optical sectioning).

NeuN quantification: Number of $NeuN^+$ neurons were manually scored from stereological identical images (3D volume-rendered) of the CA1 region of the hippocampus of stained sections (6 images per hippocampal section; 6 hippocampal sections per animal).

Quantification of amyloid deposits: Briefly, M3.2, BAM-10 or 6E10 immunostained sections covering layers II/III and IV of the neocortex or CA1 region of the hippocampus (4 images per section; 6 sections (BAM-10 and 6E10) or 10 sections (M3.2) per animal) were imaged, converted into 8-bit gray scale, 3D volume-rendered and thresholded to highlight immunostained amyloid deposits. Using FIJI software, the percent of immunostained area was calculated for each field and each section.

APP quantification: Briefly, APP immunostained sections covering layers II/III and IV of the neocortex (4 images per section; 6 sections per animal) were imaged, converted into 16-bit gray scale, and thresholded to highlight immunostained APP amounts. Using FIJI software, the percent of immunostained area was calculated for each field and each section.

Methoxy-X04 quantification: Briefly, stained sections covering layers II/III and IV of the neocortex (5 images per section; 4 sections per animal) were imaged, converted into 16-bit gray scale, and thresholded to highlight stained. Using FIJI software, the percent of stained area was calculated for each field and each section.

Quantification of synapses: Images from stereological identical hippocampal CA1 regions from each experimental group (3 images per hippocampi; 4 hippocampal sections per animal) were acquired using a Leica HC PL APO CS 40x /1.10 CORR water objective at 1024 x 1024 pixels resolution with 8-bit bidirectional non-sequential scanner mode at 400 Hz and pinhole at 1 airy in the Leica TCS SP5 II confocal microscope. Z-stacks were converted to maximum projection images using LAS AF routine and the LAS AF colocalization plugin processed each projection using subtracted background (25–36% offset for both channels) and thresholded foreground (35-45% offset for vGlut-1 channel; 30-40% offset for PSD-95 channel). Values corresponding to the positive area of vGlut-1/PSD-95 colocalization puncta (synapses) and values for the overall image area for each image was extracted using the LAS AF colocalization plugin and statistically evaluated in GraphPad Prism.

TUNEL assay: Slides were defrosted at room temperature for at least 1 h. After that, sections were hydrated in PBS and fixed with 4% PFA for 10 min. After washes with PBS, sections were blocked (10% NGS; 0,1% BSA and 1% Triton X-100) for 1 h and then equilibrated in TdT buffer (30 mM Tris-HCl; 140 mM Sodium Cacodylate; 1 mM Cobalt chloride; pH 7.2) for 10 min at room temperature. To perform the TUNEL reaction was performed using 1.6 µL of TUNEL Enzyme (11767305001; Roche); 1.2 µL of Biotin-16-dUTP (11093070910; Roche) and 1.2 µL of 1 mM dATP in 200 µL of TdT buffer. The

reaction was performed at 37ºC for 90 min. The reaction was stopped by incubation with 2x SSC buffer for 10 min. After washes with PBS, Cy3-conjugated Streptavidin (1:200 in blocking solution) and DAPI (2 ug/ml) were incubated for 1 h at room temperature. After PBS washes, sections were mounted with fluoroshield (Sigma-Aldrich). The number of TUNEL$^+$ cells was manually scored from stereological identical images of the CA1 region of the hippocampus of stained sections (4 images per hippocampal section; 8 hippocampal sections per animal).

Quantification of Iba1 colocalization with amyloid deposits: Images from stereological identical neocortical or hippocampal CA1 regions from each experimental group (4 images per section; 6 sections per animal) were acquired using a Leica HC PL APO CS 40x /1.10 CORR water objective at 1024 x 1024 pixels resolution with 8-bit bidirectional scanner mode at 200 Hz in the Leica TCS SP5 II confocal microscope. Z-stacks were converted to maximum projection images using LAS AF routine and the LAS AF colocalization plugin processed each projection using subtracted background (45-55% offset for both channels) and thresholded foreground (65% offset for BAM-10/M3.2 channel; 20-35% offset for Iba1 channel). Values corresponding to the positive area of colocalization puncta and values for the overall image area for each image were extracted using the LAS AF colocalization plugin and statistically evaluated in GraphPad Prism.

Immunofluorescence on cultured microglia: Microglial cultures were cultivated in glass coverslips. Coverslips were fixed with 4% PFA, washed three times for 5 min in PBS, permeabilized with 0.1% Triton X-100 for 10 min, washed again and incubated for 1 h in blocking solution (5% BSA). Primary antibodies were added in blocking solution and coverslips were maintained in a humidified chamber for 1 h. Coverslips were washed three times for 10 min with PBS and incubated with secondary antibodies for 1 h in blocking

solution. Next, coverslips were washed three times for 10 min with PBS. After the last secondary antibody (when double-labeling was performed), the coverslips were incubated for 1 min with 1 mg/ml DAPI, and rinsed twice in PBS. Coverslips were mounted with Immumount, visualized in a Leica DMI6000B inverted epifluorescence microscope using PlanApo 63X/1.3NA glycerol immersion objective. Images were acquired with 4 x 4 binning using a digital CMOS camera (ORCA-Flash4.0 V2, Hamamatsu Photonics).

For quantification, images were exported as raw 16-bit tiff using the LAS AF software. Background was subtracted in FIJI using the roller-ball ramp in between 35-50% pixel radius. Images were segmented in FIJI using the local Otsu threshold. Thresholded images were converted to binary mask using the dark background function. Binary mask images were multiplied for their respective original channel images using the image calculator plug-in to generate a masked 32-bit float images relative to each channel. Original coordinate vectors were retrieved from the ROI manager and FIJI returned the mean fluorescent intensity in gray values contained within any single microglia using the multi-measure function. Mean fluorescent intensity for each single microglia were exported and statistically evaluated with the GraphPad Prism software.

Time-lapse video microscopy and FRET assays: For live cell imaging, microglia were plated on plastic-bottom culture dishes (μ-Dish 35 mm, iBidi). Imaging was performed using a Leica DMI6000B inverted microscope. The excitation light source was a mercury metal halide bulb integrated with an EL6000 light attenuator. High-speed low vibration external filter wheels (equipped with CFP/YFP excitation and emission filters) were mounted on the microscope (Fast Filter Wheels, Leica Microsystems). A 440-520nm dichroic mirror (CG1, Leica Microsystems) and a PlanApo 63X 1.3NA glycerol immersion objective were used for CFP and FRET images. Images were acquired with 2x2 binning using a digital CMOS camera (ORCA-Flash4.0 V2, Hamamatsu Photonics). Shading

illumination was online-corrected for CFP and FRET channels using a shading correction routine implemented for the LAS AF software. At each time-point, CFP and FRET images were sequentially acquired using different filter combination (CFP excitation plus CFP emission (CFP channel), and CFP excitation plus YFP emission (FRET channel), respectively).

Quantification of biosensors was performed as before (Portugal et al., 2017, Socodato et al., 2015a, Socodato et al., 2015b, Socodato et al., 2018). In brief, images were exported as 16-bit tiff files and processed in FIJI software. Background was dynamically subtracted from all frames from both channels. Segmentation was achieved on a pixel-by-pixel basis using a modification of the Phansalkar algorithm. After background subtraction and thresholding, binary masks were generated for the CFP and FRET images. Original CFP and FRET images were masked, registered and bleach-corrected. Ratiometric images (CFP/FRET for KRas Src YPet probe and FLIPE glutamate release probe or FRET/CFP for Raichu-Rhoa and Flare.Rhoc sensors) were generated as 32-bit float-point tiff images. Values corresponding to the mean gray values were generated using the multi calculation function in FIJI and exported as mentioned above. KRas Src and glutamate (pDisplay FLIPE-600n^{SURFACE}) biosensors have been previously used in microglia giving reliable FRET to donor signals within the probe dynamic range (Socodato et al., 2015b, Socodato et al., 2015a, Socodato et al., 2018, Portugal et al., 2017).

For quantification of microglial protrusion velocity, HMC3 microglia expressing Lifeact-mCherry were incubated in DMEM without phenol red plus 15 mM HEPES and recorded (5 min frames for 90 min at 37°C) using appropriate dichroics for red fluorescent protein. Time-lapse images were exported as 16-bit tiff files and processed in FIJI software using the multi kymograph plugin. Protrusion velocities from Lifeact kymograms were extracted using a routine macro from the multi kymograph package in ImageJ.

***Preparation of lysates (tissue and cell cultures*)**: For ELISA, brains were removed, different brains areas were isolated, fast frozen on dry ice and stored at -80ºC. Cortices were defrosted and 400 ul of homogenization buffer (50 mM Tris-Base, 4 mM EDTA, 150 mM NaCl, 0.1% Triton X 100 and protease inhibitor cocktail containing AEBSF (Sigma – P8340)). Samples were sonicated (10 pulses of 1 sec at 60Hz) and centrifuged for 15 min at 2271 g at 4ºC. The pellets were discarded and samples were centrifuged again at 13500 g for 5 minutes at 4ºC. The supernatant was used for ELISA and the total amount of protein were estimated using the Pierce BCA protein assay kit.

For all other applications, cell cultures or mice tissues were lysed using RIPA-DTT buffer (150 mM NaCl, 50 mM Tris, 5 mM EGTA, 1% Triton X-100, 0.5% DOC, 0.1% SDS) supplemented with complete-mini protease inhibitor cocktail tablets, 1 mM DTT and phosphatase inhibitor cocktail. Samples were sonicated (6 pulses of 1 sec at 60Hz) and centrifuged at 16,000 g, 4°C for 10 min. The supernatants were collected and the protein concentration was determined by the Pierce BCA protein assay kit. All samples were denatured with sample buffer (0.5 M Tris-HCl pH 6.8, 30% glycerol, 10% SDS, 0.6 M DTT, 0.02% bromophenol blue) at 95°C for 5 min and stored at −20°C until use.

Enzyme-linked immunosorbent assay (ELISA): The concentration of Tnf, $A\beta_{1-40}$ and $A\beta_{1-42}$ were quantified by ELISA following the instructions provided by the manufacturer (Peprotech, UK). Absorbance at 405 nm, with wavelength correction at 650 nm, was measured with a multimode microplate reader (Synergy HT, Biotek, USA). Values corresponding to pg/ml were obtaining by extrapolating a standard concentration curve using recombinant Tnf.

Glutamate determination by fluorimetry: Extracellular glutamate was measured in microglia culture supernatant by the formation of NADH in a reaction catalyzed by glutamate dehydrogenase essentially as elsewhere (Socodato et al., 2015b). Briefly, Tris–acetate (75 mM, pH 8.4) plus NAD and ADP were added to culture supernatants and initial fluorescence arbitrary unit (FAU_i) was quantified in a Luminometer. Glutamate dehydrogenase was added for 30 min to promote the formation of alpha-ketoglutarate and NADH. NADH fluorescence was also determined (FAU_f). Relative extracellular glutamate content was plotted as FAU_f - FAU_i.

Nuclear and cytosolic fractionation: Cultures were washed twice with PBS, and cells were scraped off culture dishes with lysis buffer [50 mM tris-HCl, 5 mM EDTA, 100 mM NaCl, 1 mM DTT, 100 mM phenylmethylsulfonyl fluoride, 200 mM Na_3VO_4, 1% Triton X-100, leupeptin (4 mg/ml)]. Lysates were centrifuged (16,000g for 10 min at 4°C), the supernatant (cytosolic fraction) was collected, and the pellet (nuclear fraction) was resuspended. All samples were denatured with sample buffer for 5 min at 95°C and stored at −20°C. Both fractions were subjected to SDS–polyacrylamide gel electrophoresis (SDS-PAGE). To confirm the efficacy of the separation assay, we used LAMP-1 (Enzo Life Sciences) as a cytosolic fraction marker and histone H3 (Millipore) as a nuclear fraction marker.

Western blotting: Samples were separated in SDS-PAGE, transferred to PVDF membranes, which were incubated overnight with primary antibodies. Membranes were washed in TBS-T buffer pH 7.6, incubated with peroxidase-conjugated secondary antibodies and developed using an ECL chemiluminescence kit or an ECF fluorescence kit. Images were acquired in a Typhoon FLA 9000 system or ChemiDoc XRS System (Bio-Rad) and quantified by FIJI software.

Electrophysiology: For electrophysiological recordings, acute hippocampal slices from P65-80 male control and Rhoa mutants mice were prepared. All procedures were carried out according to the European Union Guidelines for Animal Care (European Union Council Directive 2010/63/EU) and Portuguese law (DL 113/2013) with the approval of the Institutional Animal Care and Use Committee.

Animals were sacrificed by decapitation after cervical displacement and the brain was rapidly removed in order to isolate the hippocampus. Hippocampi were dissected in ice-cold artificial cerebrospinal fluid (aCSF) containing: 124 mM NaCl, 3 mM KCl, 1.2 mM NaH_2PO_4, 25 mM $NaHCO_3$, 2 mM $CaCl_2$, 1 mM $MgSO_4$ and 10 mM glucose), which was continuously gassed with 95%O_2/5% CO_2. Hippocampal slices were quickly cut perpendicularly to the long axis of the hippocampus (400 µm thick) with a McIlwain tissue chopper and allowed to recover functionally and energetically for at least 1 h in a resting chamber filled with continuously oxygenated aCSF, at room temperature (22–25°C), before being set up for electrophysiological recordings.

For extracellular recordings of field Excitatory Post-Synaptic Potentials (fEPSP), slices were transferred to a recording chamber for submerged slices (1 ml capacity plus 5 ml dead volume) and were constantly superfused at a flow rate of 3 ml/min with aCSF kept at 32ºC, gassed with 95% O_2 – 5%CO_2. Evoked fEPSP were recorded extracellularly using a microelectrode (4 to 8 M extracellularly using feraCSF solution placed in the *stratum radiatum* of the CA1 area). fEPSP data were acquired using an Axoclamp-2B amplifier (Axon Instrumnets, USA). fEPSPs were evoked by stimulation through a concentric electrode to the Schaffer collateral fibres. Each individual stimulus consisted of a 0.1 ms rectangular pulse applied once every 20s, except otherwise indicated. Averages of six consecutive responses were continuously acquired, digitized with the WinLTP program (Anderson and Collingridge, 2001) and quantified as the slope of the initial phase of the

averaged fEPSPs. The stimulus intensity was adjusted at the beginning of the experiment to obtain a fEPSP slope close to 1 mV/ms, which corresponded to about 50% of the maximal fEPSP slope.

θ-burst stimulation was used to induce LTP because this pattern of stimulation is considered closer to what physiologically occurs in the hippocampus during episodes of learning and memory in living animals (Albensi et al., 2007). After obtaining a stable recording of the fEPSP slope, a θ-burst of stimuli, consisting of 1 train of 4 bursts (200 ms interburst interval), each burst being composed of 4 pulses delivered at 100 Hz [1 x (4 x 4)], was applied, and the stimulus paradigm was then resumed to pre-burst conditions up to the end of the recording period (60 min after burst stimulation). LTP magnitude was quantified as % change in the average slope of the fEPSP taken from 50-60 min after LTP induction as compared with the average slope of the fEPSP measured during the 10 min before induction of LTP. fEPSPs were recorded under basal stimulation conditions (standard stimulus intensity and frequency) and stability of fEPSP slope values guaranteed for more than 10 min before changing any protocol parameter. One or two slices per animal were tested at each experimental day.

Behavioral tests: Testing procedures were conducted in the dark phase of the light/dark cycle. Only male mice were used in behavioural analysis. Before each session, mice were removed from their home cage in the colony room and brought into the adjacent testing rooms (illuminated with 100 lux and attenuated noise). Behavioural tests were performed in 3 consecutive days in the following order: (1) elevated plus-maze; (2) open field; (3) novel object recognition. All tests were video-recorded. In the elevated plus-maze and open-field tests movement and location of mice were analyzed by an automated tracking system equipped with an infrared-sensitive camera (Smart Video Tracking Software v 2.5, Panlab, Harvard Apparatus). Data from the object recognition test were analyzed using

the Observer 5 software (Noldus Information Technology, Wageningen, The Netherlands). All apparatus were thoroughly cleaned with neutral soap after each test session.

Elevated plus-maze (EPM): The maze was made of opaque grey PVC consisting of four arms arranged in a plus-shaped format; two arms have surrounding walls (closed arms, 37x6 cm x18 cm-high), while the two opposing arms have no walls (open arms, 37x6 cm). The apparatus is elevated by 50 cm above the ground. Mice were placed on the central platform facing an open arm and were allowed to explore the maze for 5 min. Open arms entries and time spent in open arms were obtained automatically (video tracking) and used to assess anxiety-like behavior.

Open field (OF): Mice were placed in the center of an OF apparatus (40 x 40 x 40 cm) and then allowed to move freely for 10 min. The distance travelled, peripheral activity and center activity (locomotion in the central section of the OF) were obtained automatically (video tracking).

Novel object recognition (NOR): The NOR test was performed as previously described (Leger et al., 2013). Briefly, the test apparatus consists of an open box and the objects used are made of plastic, glass or metal in three different shapes: cubes, pyramids and cylinders. The test consists of three phases. During habituation phase mice are allowed to explore the apparatus for 10 min (time used to perform OF test). The following day, the acquisition/sample phase starts by placing each mouse in the apparatus with two identical objects (familiar) for 10 min. Then the mouse goes back to its home cage. After 4 h (inter-trial interval, ITI), the retention/choice session is performed. In this phase, the apparatus contains a novel object and a copy of the previous familiar object; animals are allowed to explore these objects for 3 min. Exploration was defined as follows: mouse touched the object with its nose or the mouse's nose was directed toward the object at a distance shorter than 2 cm (Ennaceur et al., 2005). Circling or sitting on the object was

not considered exploratory behavior. Increased time spent exploring the novel object serves as the measure of recognition memory for the familiar object. Positive difference between the exploration time for novel and familiar objects and a discrimination index (DI) above 0.5 were used as indicators of object recognition (Ennaceur et al., 2005). The discrimination index (DI) was calculated as index of memory function, DI = (time exploring the novel object) / (total time spent exploring both objects) (Ennaceur et al., 2005).

Cloning of shRNAs into pSicoR-GFP vector: The cloning was performed as previous described (Ventura et al., 2004). Briefly, shRNA oligos (Rhoa sense: TGTCAAGCATTTCTGTCCTTCAAGAGAATTTGGACAGAAATGCTTGACTTTTTTC and antisense: CGAGAAAAAAGTCAAGCATTTCTGTCCAAATTCTCTTGAAATTTGGACAG AAATGCTTGACA; Rhob sense: TCGACGTCATCCTTATGTGCTTTTCAAGAG AAAGCACATAAGGATGACGTCGTTTTTTC and antisense: TCGAGAAAAAACGACGT CTTATGTGCTTTCTCTTGAAAAGCACATAAGGATGACGTCGA; Rhoc sense: TACCTG AGGCAAGATGAGCATATTCAAGAGATATGCTCATCTTGCCTCAGGTTTTTTTC and antisense: GAGAAAAAAACCTGAGGCAAGATGAGCATATCTCTTGAATATGCTCATCT TGCCTCAGGTA were annealed and cloned into *Hpa*I-*Xho*I-digested pSicoR using the T_4 ligase. Oligos insertion into the vector was validated using PCR and confirmed by sequencing. A control shRNA with no mammalian target (directed against DsRed2; referred to as scrambled) was used in experiments using the pSicoR as before (Portugal et al., 2017).

Lentiviruses/Retroviruses production: This protocol was performed exactly as described elsewhere (Socodato et al., 2012, Mejia-Garcia et al., 2013). Low passage HEK293T cells were seeded in 100 mm culture dishes. When cultures reached ~80% confluence cells were co-transfected overnight with viruses-producing plasmids using

jetPRIME®. Transfection ratios were as follows: 6 µg of shRNA plasmids to 3 µg of psPAX2 to 3 µg of VSVG (2:1:1) for lentiviruses production or 8 µg of VSVG (or Src^{Y416F} or Src^{Y527F} construct to 4 µg of pUMVC to 2 µg of VSVG (4:2:1) for retroviruses production. The next day, normal growth media replaced transfection media and cells were cultivated for an additional 48 h. Next, media with viral particles were collected, centrifuged at 906 g for 15 min at 4°C, and the supernatant was collected into new tubes and kept at -80°C.

Total RNA extraction, cDNA synthesis and qRT-PCR: Total cerebral cortex RNA was extracted using the Direct-zol™ RNA MiniPrep kit according to the manufacturer's instructions. RNA from FACS-sorted microglia was harvested using the Quick-RNA™ MicroPrep kit. RNAs quality and concentration were all determined using a NanoDrop ND-1000 Spectrophotometer. cDNA synthesis was performed using 100-500 ng of total RNA (DNase I treated) with SuperScript® III First-Strand Synthesis SuperMix.

qRT-PCR was carried out using iQ™ SYBR® Green Supermix on an iQ™5 multicolor real-time PCR detection system (Bio-Rad). The efficiency was analyzed using a log-based standard curve. Expression of PCR transcripts between genotypes was calculated using the $2^{-deltaCt}$ method with *Yhwaz* serving as the internal control gene.

Preparation of Aβ oligomers: Human $A\beta_{1-42}$ peptide (Genscript) was dissolved to 2 mM in DMSO essentially as before (Silva et al., 2017). For oligomer formation, $A\beta_{1-42}$ peptide was diluted to 100 µM in Ca^{2+}-free HBSS and incubated for 24-48 h at 4°C. Oligomers were used at final concentration of 200 nM in microglial cultures.

$A\beta_{1-42}$ uptake assay: HMC3 microglial cells were seeded on 96-well plate (PerkinElmer) at 1×10^4 cells per well using an automated Multidrop dispenser (Thermo Scientific) and incubated for 24 hours at 37ºC in 5% CO_2. Then, cells were co-transfected with FKBP-

YFP and FRB-Lyn and or with Rhoa-YF (CA) and FRB-Lyn. For chemogenetic activation of Rhoa, cells were pre-treated with rapamycin (Sigma; 500 nM) for 15 min. Different non-transfected cultures were also pre-incubated with AZD 0530 (Src inhibitor; 500 nM) or vehicle (DMSO) for 15 min. Afterwards, cells were incubated with 10 µg/ml Aβ(1–42) HiLyte™ Fluor 555-labeled (Eurogentec) for 90 min at 37 °C in 5% CO_2. Cells were then thoroughly washed, fixed with 4% MP-paraformaldehyde (w/v), permeabilized with 0.1% (v/v) Triton X-100 (Sigma) for 30 min at room temperature and labelled with DAPI and HCS CellMask™ (Invitrogen).

Images of microglial cultures were acquired using IN Cell Analyzer 2000 microscope (GE Healthcare) using a large chip CCD Camera (binning 2X2) and a Nikon 20x/0.45 NA Plan Fluor objective. Images of $A\beta_{1-42}$, DAPI-stained nuclei, HCS CellMask™ and in some conditions transfected (YFP^+) cells were acquired using appropriate dichroics for TexasRed, DAPI, Cy5 and FITC channels, respectively. For $A\beta_{1-42}$ signal quantification, the CellProfiler (3.1.8) software was used. For nuclei segmentation, a global thresholding strategy was used followed by Otsu local thresholding. Clumped microglial nuclei were distinguished and individualized. Afterwards, microglial cells were segmented using the raw HCS CellMask™ image through a propagation algorithm based on the minimum cross entropy thresholding method applied to the HCS CellMask™ channel using segmented nuclei as start point and then spanning up to the edges of the labelled microglial plasma membrane. The mean fluorescent intensity of $A\beta_{1–42}$ HiLyte™ Fluor 555 in each microglial cell was retrieved and plotted for statistical evaluation.

QUANTIFICATION AND STATISTICAL ANALYSIS

A 95% confidence interval was used for statistical evaluation and $p < 0.05$ was considered statistically significant difference in all sampled groups. Experimental units in individual replicates were prior evaluated for Gaussian distribution using the D'Agostino & Pearson omnibus normality test. When comparing only 2 experimental groups Mann-Whitney test for data with non-normal distribution or unpaired Student t test with equal variance assumption for data with normal distribution was used. When comparing 3 or more groups with data without normal distribution the Kruskal-Wallis test followed by Dunn`s multiple comparation was used and One-way ANOVA followed by the Bonferroni multiple comparation test was used for data with normal distribution. Two-way ANOVA was used to determine significative differences between genotypes in the Sholl analysis of microglia in the brain and in live cell imaging experiments with microglia exposed to Aß oligomers. All imaging quantifications (cell cultures, FACS or mice tissue sections) were performed blinded. All statistical analyses were carried out using the Graph Pad Prism 6.0 software. Further statistical details are indicated in the figure legends.

DATA AND CODE AVAILABILITY

This study did not generate datasets or codes.

KEY RESOURCES TABLE

REAGENT or RESOURCE	SOURCE	IDENTIFIER
Antibodies		
Rhoa antibody	Abcam	Cat#ab86297; RID:AB_10675086
RhoA (67B9) antibody	Cell Signaling Technology	Cat#2117; RRID:AB_10693922
Active RhoA-GTP antibody	NewEast Biosciences	Cat#26904; RRID:AB_1961799
Src antibody [EPR5496]	Abcam	Cat#ab109381; RRID:AB_10865528
Amyloid beta precursor protein antibody [Y188]	Abcam	Cat#ab32136; RRID:AB_2289606
GFP antibody	Abcam	Cat#ab6673; RRID:AB_305643
Anti-NeuN antibody	Millipore	Cat#MAB377; RRID:AB_2298772
Phospho-Src Family (Tyr416) (D49G4) Rabbit mAb antibody	Cell Signaling Technology	Cat#6943; RRID:AB_10013641
Phospho-Src Family (Tyr416) Antibody	Cell Signaling Technology	Cat#2101; RRID:AB_331697
NF- κB p65 (L8F6) Mouse mAb antibody	Cell Signaling Technology	Cat#6956; RRID:AB_10828935
Csk (C74C1) Rabbit mAb antibody	Cell Signaling Technology	Cat#498; RRID:AB_2276592
Rabbit Anti-PSD95 Monoclonal Antibody, Unconjugated, Clone D74D3	Cell Signaling Technology	Cat#3409; RRID:AB_1264242
PSD95 Monoclonal Antibody (6G6-1C9)	Thermo Fisher Scientific	Cat#MA1-045; RRID:AB_325399
Anti Iba1, Rabbit antibody	Wako	Cat#019-19741; RRID:AB_839504
Mouse Anti-Glyceraldehyde-3-Phosphate Dehydrogenase (GAPDH) Antibody, Unconjugated	Hytest	Cat#5G4-9B3; RRID:AB_1616725
Mouse Anti-beta-Actin Monoclonal Antibody, Unconjugated, Clone AC-74	Sigma-Aldrich	Cat#A2228; RRID:AB_476697
Monoclonal Anti-Synaptophysin antibody produced in mouse	Sigma-Aldrich	Cat#S5768; RRID:AB_477523
Mouse Anti-beta-Amyloid Protein Monoclonal Antibody, Unconjugated, Clone BAM-10	Sigma-Aldrich	Cat#A5213; RRID:AB_476742
VGLUT 1 (vesicular glutamate transporter 1, BNPI, SLC17A7)	Synaptic Systems	Cat#135 303; RRID:AB_887875

antibody		
Anti-Synapsin 1 antibody	Synaptic Systems	Cat#106 011C5; RRID:AB_993033
Purified anti-mouse/rat β-Amyloid, 1-16 antibody	BioLegend	Cat#805707; RRID:AB_2734556
Purified anti-β-Amyloid, 1-16 antibody	BioLegend	Cat#803004; RRID:AB_2715854
Purified anti-β-Amyloid, 1-42 antibody	BioLegend	Cat#805509; RRID:AB_2783381
LAMP1, mAb (Ly1C6) antibody	Enzo Life Sciences	Cat#ADI-VAM-EN001; RRID:AB_10630197
Anti-Histone H3, CT, pan antibody	Millipore	Cat#07-690; RRID:AB_417398
PE anti-mouse CD45 antibody	BioLegend	Cat#103106; RRID:AB_312971
APC anti-mouse/human CD11b antibody	BioLegend	Cat#101212; RRID:AB_312795
Alexa Fluor® 647 anti-mouse/human CD11b antibody	BioLegend	Cat#101218; RRID:AB_389327
PerCP/Cyanine5.5 anti-mouse Ly-6C antibody	BioLegend	Cat#128012;RRID:AB_1659241
Goat Anti-Mouse IgG (H+L) Antibody, Alexa Fluor 568 Conjugated	Molecular Probes	Cat#A-11004; RRID:AB_2534072
Goat Anti-Rabbit IgG (H+L) Antibody, Alexa Fluor 568 Conjugated	Molecular Probes	Cat#A-11011; RRID:AB_143157
Goat anti-Mouse IgG (H+L) Secondary Antibody, Alexa Fluor® 594 conjugate	Thermo Fisher Scientific	Cat#A-11005; RRID:AB_2534073
Goat anti-Rabbit IgG (H+L) Secondary Antibody, Alexa Fluor® 594 conjugate	Thermo Fisher Scientific	Cat#A-11012; RRID:AB_2534079
Goat anti-Mouse IgG (H+L) Highly Cross-Adsorbed Secondary Antibody, Alexa Fluor Plus 647	Thermo Fisher Scientific	Cat#A32728; RRID:AB_2633277
Goat anti-Rabbit IgG (H+L) Cross-Adsorbed Secondary Antibody, Alexa Fluor 647	Thermo Fisher Scientific	Cat#A-21244; RRID:AB_2535812

Peroxidase-AffiniPure Donkey Anti-Rabbit IgG (H+L) (min X Bov,Ck,Gt,GP,Sy Hms,Hrs,Hu,Ms,Rat,Shp Sr Prot) antibody	Jackson ImmunoResearch Labs	Cat#711-035-152; RRID:AB_10015282
Peroxidase-AffiniPure Donkey Anti-Mouse IgG (H+L) (min X Bov,Ck,Gt,GP,Sy Hms,Hrs,Hu,Rb,Rat,Shp Sr Prot) antibody	Jackson ImmunoResearch Labs	Cat#715-035-151; RRID:AB_2340771
Adalimumab	Selleckchem	Cat#A2010
CD11b MicroBeads, human and mouse	Miltenyi Biotech	Cat#130-049-601
PE/Cy7 Annexin V	BioLegend	Cat#640950
PE/Cy7 anti-mouse Ki-67 antibody	BioLegend	Cat#652426; RRID:AB_2632694
Monoclonal Anti-beta-Amyloid antibody produced in mouse	Sigma-Aldrich	Cat#A5213; RRID:AB_476742
PE/Cy7 anti-mouse/human CD11b antibody	BioLegend	Cat#101215; RRID:AB_312798
PE/Cy7 anti-mouse CD192 (CCR2) Antibody	BioLegend	Cat#150611; RRID:AB_2616983
Bacterial and Virus Strains		
Subcloning Efficiency™ DH5α Competent Cells	Thermo Fisher Scientific	Cat#18265017
Chemicals, Peptides, and Recombinant Proteins		
Recombinant Murine GM-CSF	Peprotech	Cat#315-03
Recombinant Human TNF-α	Peprotech	Cat#300-01A
Recombinant Murine TNF-α	Peprotech	Cat#315-01A
Amyloid β Protein Fragment 1-42	Sigma-Aldrich	Cat#A9810; CAS Number 107761-42-2
Beta - Amyloid (1 - 42), HiLyte™ Fluor 555 - labeled, Human	AnaSpec, Inc	Cat#AS-60480-01
Lipopolysaccharide (LPS) from Escherichia coli 0111:B4	Sigma-Aldrich	Cat#L2630; MDL number MFCD00164401
Src Inhibitor-1	Sigma-Aldrich	Cat#S2075; CAS Number: 179248-59-0
Rapamycin	Sigma-Aldrich	Cat#R8781
18α-Glycyrrhetinic acid	Sigma-Aldrich	Cat#G8503; CAS Number 1449-05-4
Tamoxifen	Sigma-Aldrich	Cat#T5648; CAS Number 10540-29-1
Pomalidomide	Selleckchem	Cat#S1567; CAS Number 19171-19-8

Saracatinib (AZD0530)	Selleckchem	Cat#S1006; CAS Number 379231-04-6
Recombinant Murine M-CSF	Peprotech	Cat#315-02
Zombie Violet™ Fixable Viability Kit	BioLegend	Cat#423114
Methoxy-X04	Tocris	Cat#4920; CAS Number 863918-78-9
Critical Commercial Assays		
Amyloid beta 40 Mouse ELISA Kit	Thermo Fisher Scientific	Cat#KMB3481
Murine TNF-α Standard ABTS ELISA Development Kit	Peprotech	Cat#900-K54
Amyloid beta 42 Mouse ELISA Kit	Thermo Fisher Scientific	Cat#KMB3441
Pierce™ ECL Western Blotting Substrate	Thermo Fisher Scientific	Cat#32106
Thermo Scientific™ SuperSignal™ West Pico Chemiluminescent Substrate	Thermo Fisher Scientific	Cat#10481755
ABTS ELISA Buffer Kit	Peprotech	Cat#900-K00
Experimental Models: Cell Lines		
CHME3 cell line (distributed as HMC3 cells)	ATCC	Cat#CRL-3304; RRID:CVCL_II76
N9 cell line	Prof. Claudia Verderio, CNR Institute of Neuroscience, Cellular and Molecular Pharmacology, Milan, Italy	RRID:CVCL_0452
Experimental Models: Organisms/Strains		
Mouse: $Rhoa^{fl/fl}$:$Cx3cr1^{CreER+}$	This work	N/A
Mouse: TNF knock out	Prof. Rui Applelberg, Universtity of Porto	N/A
Mouse: B6;C3-Tg(APP695)3Dbo Tg(PSEN1)5Dbo/Mmjax (herein APP/PS1)	The Jackson Laboratory	RRID:MMRRC_041848-JAX
Mouse: B6.129P2(Cg)-$Cx3cr1^{tm2.1(cre/ERT2)Litt}$/WganJ (herein $Cx3cr1^{CreER-EYFP}$)	The Jackson Laboratory	Cat#JAX:021160; RRID:IMSR_JAX:021160
Mouse: $Rhoa^{tm1Jrel}$ (herein $Rhoa^{fl/fl}$)	MGI	MGI:4950374
Oligonucleotides		
Primers	See Table S1	N/A
Oligos for pSicoR cloning	See Table S1	N/A
shRNA oligos	See Table S1	N/A
Recombinant DNA		

pTriEx-RhoA FLARE.sc Biosensor Q63L	PMID:16547516	RRID:Addgene_12151
pRK5-myc-RhoA-Q63L	Gary Bokoch (unpublished)	RRID:Addgene_12964
pRK5-myc-RhoA-T19N	Gary Bokoch (unpublished)	RRID:Addgene_12963
pRK5-myc-RhoA-wt	Gary Bokoch (unpublished)	RRID:Addgene_12962
pUSE-RapR-Src-myc	PMID:20581846	RRID:Addgene_25933
pDisplay FLIPE-600n	PMID:15939876	RRID:Addgene_13545
pIκBα-miRFP703	PMID:27539380	RRID:Addgene_80005
psPAX2	Didier Trono (unpublished)	RRID:Addgene_12260
pMD2.G	Didier Trono (unpublished)	RRID:Addgene_12259
pUMVC	PMID:12649500	RRID:Addgene_8449
GFP-RelA	PMID:11533489	RRID:Addgene_23255
MSCV	PMID:20008935	RRID:Addgene_24828
pSicoR	PMID:15240889	RRID:Addgene_11579
YF-RhoA(CA)	PMID:15908919	RRID:Addgene_20153
YFP-FKBP (YF)	PMID:15908919	RRID:Addgene_20175
Lyn11-targeted FRB (LDR)	PMID:15908919	RRID:Addgene_20147
pCherry-FRB	PMID:20581846	RRID:Addgene_25920
mCherry-Lifeact-7	Michael Davidson (unpublished)	RRID:Addgene_54491
RhoC FLARE.sc mCer, mVenus - wt	PMID:24224016	RRID:Addgene_65071
Kras-Src FRET biosensor	PMID:18799748	RRID:Addgene_78302
Raichu-RhoA	Michiyuki Matsuda; PMID:12860967	N/A
pLNCX chick src Y416F	Joan Brugge (unpublished)	RRID:Addgene_13662
pLNCX chick src Y527F	Joan Brugge (unpublished)	RRID:Addgene_13660
pLNCX chick src	Joan Brugge (unpublished)	RRID:Addgene_13665
pTriEx-RhoA FLARE.sc Biosensor WT	PMID:16547516	RRID:Addgene_12150
pTriEx-RhoA FLARE.sc Biosensor T19N	PMID:16547516	RRID:Addgene_12152
pFRET-HSP33 cys	Ulrich Hammerling (unpublished)	RRID:Addgene_16076
Software and Algorithms		
Fiji	PMID:22743772	RRID:SCR_002285
GraphPad Prism	http://www.graphpad.com/	RRID:SCR_002798
Adobe Illustrator	http://www.adobe.com/products/illustrator.html	RRID:SCR_010279
Sholl analysis plugin for ImageJ	PMID:25264773 (distributed with Fiji; https://imagej.net/Downloads)	N/A
FlowJo	https://www.flowjo.com/solutions/flowjo	RRID:SCR_008520

References

ABD-EL-BASSET, E. & FEDOROFF, S. 1995. Effect of bacterial wall lipopolysaccharide (LPS) on morphology, motility, and cytoskeletal organization of microglia in cultures. *J Neurosci Res,* 41**,** 222-37.

ALBENSI, B. C., OLIVER, D. R., TOUPIN, J. & ODERO, G. 2007. Electrical stimulation protocols for hippocampal synaptic plasticity and neuronal hyper-excitability: are they effective or relevant? *Exp Neurol,* 204**,** 1-13.

ANDERSON, W. W. & COLLINGRIDGE, G. L. 2001. The LTP Program: a data acquisition program for on-line analysis of long-term potentiation and other synaptic events. *J Neurosci Methods,* 108**,** 71-83.

ARTHUR, W. T., PETCH, L. A. & BURRIDGE, K. 2000. Integrin engagement suppresses RhoA activity via a c-Src-dependent mechanism. *Curr Biol,* 10**,** 719-22.

ASKEW, K., LI, K., OLMOS-ALONSO, A., GARCIA-MORENO, F., LIANG, Y., RICHARDSON, P., TIPTON, T., CHAPMAN, M. A., RIECKEN, K., BECCARI, S., SIERRA, A., MOLNAR, Z., CRAGG, M. S., GARASCHUK, O., PERRY, V. H. & GOMEZ-NICOLA, D. 2017. Coupled Proliferation and Apoptosis Maintain the Rapid Turnover of Microglia in the Adult Brain. *Cell Rep,* 18**,** 391-405.

BIANCHI, R., KASTRISIANAKI, E., GIAMBANCO, I. & DONATO, R. 2011. S100B protein stimulates microglia migration via RAGE-dependent up-regulation of chemokine expression and release. *J Biol Chem,* 286**,** 7214-26.

BLOCK, M. L., ZECCA, L. & HONG, J. S. 2007. Microglia-mediated neurotoxicity: uncovering the molecular mechanisms. *Nat Rev Neurosci,* 8**,** 57-69.

BORCHELT, D. R., RATOVITSKI, T., VAN LARE, J., LEE, M. K., GONZALES, V., JENKINS, N. A., COPELAND, N. G., PRICE, D. L. & SISODIA, S. S. 1997. Accelerated amyloid deposition in the brains of transgenic mice coexpressing mutant presenilin 1 and amyloid precursor proteins. *Neuron,* 19**,** 939-45.

BORCHELT, D. R., THINAKARAN, G., ECKMAN, C. B., LEE, M. K., DAVENPORT, F., RATOVITSKY, T., PRADA, C. M., KIM, G., SEEKINS, S., YAGER, D., SLUNT, H. H., WANG, R., SEEGER, M., LEVEY, A. I., GANDY, S. E., COPELAND, N. G., JENKINS, N. A., PRICE, D. L., YOUNKIN, S. G. & SISODIA, S. S. 1996. Familial Alzheimer's disease-linked presenilin 1 variants elevate Abeta1-42/1-40 ratio in vitro and in vivo. *Neuron,* 17**,** 1005-13.

BROUNS, M. R., MATHESON, S. F. & SETTLEMAN, J. 2001. p190 RhoGAP is the principal Src substrate in brain and regulates axon outgrowth, guidance and fasciculation. *Nat Cell Biol,* 3**,** 361-7.

BROWN, G. C. & NEHER, J. J. 2014. Microglial phagocytosis of live neurons. *Nat Rev Neurosci,* 15**,** 209-16.

BUSTELO, X. R., SAUZEAU, V. & BERENJENO, I. M. 2007. GTP-binding proteins of the Rho/Rac family: regulation, effectors and functions in vivo. *Bioessays,* 29**,** 356-70.

CHAKRABARTY, P., CEBALLOS-DIAZ, C., BECCARD, A., JANUS, C., DICKSON, D., GOLDE, T. E. & DAS, P. 2010a. IFN-gamma promotes complement expression and attenuates amyloid plaque deposition in amyloid beta precursor protein transgenic mice. *J Immunol,* 184**,** 5333-43.

CHAKRABARTY, P., HERRING, A., CEBALLOS-DIAZ, C., DAS, P. & GOLDE, T. E. 2011. Hippocampal expression of murine TNFalpha results in attenuation of amyloid deposition in vivo. *Mol Neurodegener,* 6**,** 16.

CHAKRABARTY, P., JANSEN-WEST, K., BECCARD, A., CEBALLOS-DIAZ, C., LEVITES, Y., VERBEECK, C., ZUBAIR, A. C., DICKSON, D., GOLDE, T. E. & DAS, P. 2010b. Massive gliosis induced by interleukin-6 suppresses Abeta deposition in vivo: evidence against inflammation as a driving force for amyloid deposition. *FASEB J,* 24**,** 548-59.

CHARDIN, P., BOQUET, P., MADAULE, P., POPOFF, M. R., RUBIN, E. J. & GILL, D. M. 1989. The mammalian G protein rhoC is ADP-ribosylated by Clostridium botulinum exoenzyme C3 and affects actin microfilaments in Vero cells. *EMBO J,* 8**,** 1087-92.

CHEN, M., LIU, A., OUYANG, Y., HUANG, Y., CHAO, X. & PI, R. 2013. Fasudil and its analogs: a new powerful weapon in the long war against central nervous system disorders? *Expert Opin Investig Drugs,* 22**,** 537-50.

CHONG, C. M., AI, N. & LEE, S. M. 2017. ROCK in CNS: Different Roles of Isoforms and Therapeutic Target for Neurodegenerative Disorders. *Curr Drug Targets,* 18**,** 455-462.

CIRRITO, J. R., YAMADA, K. A., FINN, M. B., SLOVITER, R. S., BALES, K. R., MAY, P. C., SCHOEPP, D. D., PAUL, S. M., MENNERICK, S. & HOLTZMAN, D. M. 2005. Synaptic activity regulates interstitial fluid amyloid-beta levels in vivo. *Neuron,* 48**,** 913-22.

CROTTI, A. & RANSOHOFF, R. M. 2016. Microglial Physiology and Pathophysiology: Insights from Genome-wide Transcriptional Profiling. *Immunity,* 44**,** 505-515.

DECZKOWSKA, A., AMIT, I. & SCHWARTZ, M. 2018. Microglial immune checkpoint mechanisms. *Nat Neurosci,* 21**,** 779-786.

DEGEER, J. & LAMARCHE-VANE, N. 2013. Rho GTPases in neurodegeneration diseases. *Exp Cell Res,* 319**,** 2384-94.

DI CUNTO, F., IMARISIO, S., HIRSCH, E., BROCCOLI, V., BULFONE, A., MIGHELI, A., ATZORI, C., TURCO, E., TRIOLO, R., DOTTO, G. P., SILENGO, L. & ALTRUDA, F. 2000. Defective neurogenesis in citron kinase knockout mice by altered cytokinesis and massive apoptosis. *Neuron,* 28**,** 115-27.

DI FILIPPO, M., SARCHIELLI, P., PICCONI, B. & CALABRESI, P. 2008. Neuroinflammation and synaptic plasticity: theoretical basis for a novel, immune-centred, therapeutic approach to neurological disorders. *Trends Pharmacol Sci,* 29**,** 402-12.

DROPPELMANN, C. A., CAMPOS-MELO, D., VOLKENING, K. & STRONG, M. J. 2014. The emerging role of guanine nucleotide exchange factors in ALS and other neurodegenerative diseases. *Front Cell Neurosci,* 8**,** 282.

EKERT, J. O., GOULD, R. L., REYNOLDS, G. & HOWARD, R. J. 2018. TNF alpha inhibitors in Alzheimer's disease: A systematic review. *Int J Geriatr Psychiatry,* 33**,** 688-694.

ENNACEUR, A., MICHALIKOVA, S., BRADFORD, A. & AHMED, S. 2005. Detailed analysis of the behavior of Lister and Wistar rats in anxiety, object recognition and object location tasks. *Behav Brain Res,* 159**,** 247-66.

FERREIRA, T. A., BLACKMAN, A. V., OYRER, J., JAYABAL, S., CHUNG, A. J., WATT, A. J., SJOSTROM, P. J. & VAN MEYEL, D. J. 2014. Neuronal morphometry directly from bitmap images. *Nat Methods,* 11**,** 982-4.

FUGER, P., HEFENDEHL, J. K., VEERARAGHAVALU, K., WENDELN, A. C., SCHLOSSER, C., OBERMULLER, U., WEGENAST-BRAUN, B. M., NEHER, J. J., MARTUS, P., KOHSAKA, S., THUNEMANN, M., FEIL, R., SISODIA, S. S., SKODRAS, A. & JUCKER, M. 2017. Microglia turnover with aging and in an Alzheimer's model via long-term in vivo single-cell imaging. *Nat Neurosci,* 20**,** 1371-1376.

GINHOUX, F., GRETER, M., LEBOEUF, M., NANDI, S., SEE, P., GOKHAN, S., MEHLER, M. F., CONWAY, S. J., NG, L. G., STANLEY, E. R., SAMOKHVALOV, I. M. & MERAD, M. 2010. Fate mapping analysis reveals that adult microglia derive from primitive macrophages. *Science,* 330**,** 841-5.

GINHOUX, F. & GUILLIAMS, M. 2016. Tissue-Resident Macrophage Ontogeny and Homeostasis. *Immunity,* 44**,** 439-449.

GOLDMANN, T., WIEGHOFER, P., JORDAO, M. J., PRUTEK, F., HAGEMEYER, N., FRENZEL, K., AMANN, L., STASZEWSKI, O., KIERDORF, K., KRUEGER, M., LOCATELLI, G., HOCHGERNER, H., ZEISER, R., EPELMAN, S., GEISSMANN, F., PRILLER, J., ROSSI, F. M., BECHMANN, I., KERSCHENSTEINER, M., LINNARSSON, S., JUNG, S. & PRINZ, M. 2016. Origin, fate and dynamics of macrophages at central nervous system interfaces. *Nat Immunol,* 17**,** 797-805.

GOLDMANN, T., WIEGHOFER, P., MULLER, P. F., WOLF, Y., VAROL, D., YONA, S., BRENDECKE, S. M., KIERDORF, K., STASZEWSKI, O., DATTA, M., LUEDDE, T., HEIKENWALDER, M., JUNG, S. & PRINZ, M. 2013. A new type of microglia gene targeting shows TAK1 to be pivotal in CNS autoimmune inflammation. *Nat Neurosci,* 16**,** 1618-26.

GOMEZ-NICOLA, D., FRANSEN, N. L., SUZZI, S. & PERRY, V. H. 2013. Regulation of microglial proliferation during chronic neurodegeneration. *J Neurosci,* 33**,** 2481-93.

GOVEK, E. E., NEWEY, S. E. & VAN AELST, L. 2005. The role of the Rho GTPases in neuronal development. *Genes Dev,* 19**,** 1-49.

GREEN, T. P., FENNELL, M., WHITTAKER, R., CURWEN, J., JACOBS, V., ALLEN, J., LOGIE, A., HARGREAVES, J., HICKINSON, D. M., WILKINSON, R. W., ELVIN, P., BOYER, B., CARRAGHER, N., PLE, P. A., BERMINGHAM, A., HOLDGATE, G. A., WARD, W. H., HENNEQUIN, L. F., DAVIES, B. R. & COSTELLO, G. F. 2009. Preclinical anticancer activity of the potent, oral Src inhibitor AZD0530. *Mol Oncol,* 3**,** 248-61.

HERZOG, D., LOETSCHER, P., VAN HENGEL, J., KNUSEL, S., BRAKEBUSCH, C., TAYLOR, V., SUTER, U. & RELVAS, J. B. 2011. The small GTPase RhoA is required to maintain spinal cord neuroepithelium organization and the neural stem cell pool. *J Neurosci,* 31**,** 5120-30.

HODGE, R. G. & RIDLEY, A. J. 2016. Regulating Rho GTPases and their regulators. *Nat Rev Mol Cell Biol,* 17**,** 496-510.

HOFFMANN, A., HOFMANN, F., JUST, I., LEHNARDT, S., HANISCH, U. K., BRUCK, W., KETTENMANN, H., AHNERT-HILGER, G. & HOLTJE, M. 2008. Inhibition of Rho-dependent pathways by Clostridium botulinum C3 protein induces a proinflammatory profile in microglia. *Glia,* 56**,** 1162-75.

HONG, S., BEJA-GLASSER, V. F., NFONOYIM, B. M., FROUIN, A., LI, S., RAMAKRISHNAN, S., MERRY, K. M., SHI, Q., ROSENTHAL, A., BARRES, B. A., LEMERE, C. A., SELKOE, D. J. & STEVENS, B. 2016. Complement and microglia mediate early synapse loss in Alzheimer mouse models. *Science,* 352**,** 712-716.

HUVENEERS, S. & DANEN, E. H. 2009. Adhesion signaling - crosstalk between integrins, Src and Rho. *J Cell Sci,* 122**,** 1059-69.

INOUE, T., HEO, W. D., GRIMLEY, J. S., WANDLESS, T. J. & MEYER, T. 2005. An inducible translocation strategy to rapidly activate and inhibit small GTPase signaling pathways. *Nat Methods,* 2**,** 415-8.

JACKSON, B., PEYROLLIER, K., PEDERSEN, E., BASSE, A., KARLSSON, R., WANG, Z., LEFEVER, T., OCHSENBEIN, A. M., SCHMIDT, G., AKTORIES, K., STANLEY, A., QUONDAMATTEO, F., LADWEIN, M., ROTTNER, K., VAN HENGEL, J. & BRAKEBUSCH, C. 2011. RhoA is dispensable for skin development, but crucial for contraction and directed migration of keratinocytes. *Mol Biol Cell,* 22**,** 593-605.

JANABI, N., PEUDENIER, S., HERON, B., NG, K. H. & TARDIEU, M. 1995. Establishment of human microglial cell lines after transfection of primary cultures of embryonic microglial cells with the SV40 large T antigen. *Neurosci Lett,* 195**,** 105-8.

JIN, L. W., HORIUCHI, M., WULFF, H., LIU, X. B., CORTOPASSI, G. A., ERICKSON, J. D. & MAEZAWA, I. 2015. Dysregulation of glutamine transporter SNAT1 in Rett syndrome microglia: a mechanism for mitochondrial dysfunction and neurotoxicity. *J Neurosci,* 35**,** 2516-29.

JULIAN, L. & OLSON, M. F. 2014. Rho-associated coiled-coil containing kinases (ROCK): structure, regulation, and functions. *Small GTPases,* 5**,** e29846.

JUNG, S., ALIBERTI, J., GRAEMMEL, P., SUNSHINE, M. J., KREUTZBERG, G. W., SHER, A. & LITTMAN, D. R. 2000. Analysis of fractalkine receptor CX(3)CR1 function by targeted deletion and green fluorescent protein reporter gene insertion. *Mol Cell Biol,* 20**,** 4106-14.

KARGINOV, A. V., DING, F., KOTA, P., DOKHOLYAN, N. V. & HAHN, K. M. 2010. Engineered allosteric activation of kinases in living cells. *Nat Biotechnol,* 28**,** 743-7.

KAUFMAN, A. C., SALAZAR, S. V., HAAS, L. T., YANG, J., KOSTYLEV, M. A., JENG, A. T., ROBINSON, S. A., GUNTHER, E. C., VAN DYCK, C. H., NYGAARD, H. B. & STRITTMATTER, S. M. 2015. Fyn inhibition rescues established memory and synapse loss in Alzheimer mice. *Ann Neurol,* 77**,** 953-71.

KAUR, C. 1997. Effects of colchicine on amoeboid microglial cells in the postnatal rat brain. *Arch Histol Cytol,* 60**,** 453-62.

KIERDORF, K., ERNY, D., GOLDMANN, T., SANDER, V., SCHULZ, C., PERDIGUERO, E. G., WIEGHOFER, P., HEINRICH, A., RIEMKE, P., HOLSCHER, C., MULLER, D. N., LUCKOW, B., BROCKER, T., DEBOWSKI, K., FRITZ, G., OPDENAKKER, G., DIEFENBACH, A., BIBER, K., HEIKENWALDER, M., GEISSMANN, F., ROSENBAUER,

F. & PRINZ, M. 2013. Microglia emerge from erythromyeloid precursors via Pu.1- and Irf8-dependent pathways. *Nat Neurosci,* 16**,** 273-80.

KIM, D. C., KIM, S. H., JEONG, M. W., BAEK, N. I. & KIM, K. T. 2005. Effect of rottlerin, a PKC-delta inhibitor, on TLR-4-dependent activation of murine microglia. *Biochem Biophys Res Commun,* 337**,** 110-5.

LEGER, M., QUIEDEVILLE, A., BOUET, V., HAELEWYN, B., BOULOUARD, M., SCHUMANN-BARD, P. & FRERET, T. 2013. Object recognition test in mice. *Nat Protoc,* 8**,** 2531-7.

LESNE, S., ALI, C., GABRIEL, C., CROCI, N., MACKENZIE, E. T., GLABE, C. G., PLOTKINE, M., MARCHAND-VERRECCHIA, C., VIVIEN, D. & BUISSON, A. 2005. NMDA receptor activation inhibits alpha-secretase and promotes neuronal amyloid-beta production. *J Neurosci,* 25**,** 9367-77.

LOEGERING, D. J. & LENNARTZ, M. R. 2011. Protein kinase C and toll-like receptor signaling. *Enzyme Res,* 2011**,** 537821.

MAEZAWA, I. & JIN, L. W. 2010. Rett syndrome microglia damage dendrites and synapses by the elevated release of glutamate. *J Neurosci,* 30**,** 5346-56.

MEJIA-GARCIA, T. A., PORTUGAL, C. C., ENCARNACAO, T. G., PRADO, M. A. & PAES-DE-CARVALHO, R. 2013. Nitric oxide regulates AKT phosphorylation and nuclear translocation in cultured retinal cells. *Cell Signal,* 25**,** 2424-39.

MOHR, C., KOCH, G., JUST, I. & AKTORIES, K. 1992. ADP-ribosylation by Clostridium botulinum C3 exoenzyme increases steady-state GTPase activities of recombinant rhoA and rhoB proteins. *FEBS Lett,* 297**,** 95-9.

MOON, M. Y., KIM, H. J., LI, Y., KIM, J. G., JEON, Y. J., WON, H. Y., KIM, J. S., KWON, H. Y., CHOI, I. G., RO, E., JOE, E. H., CHOE, M., KWON, H. J., KIM, H. C., KIM, Y. S. & PARK, J. B. 2013. Involvement of small GTPase RhoA in the regulation of superoxide production in BV2 cells in response to fibrillar Abeta peptides. *Cell Signal,* 25**,** 1861-9.

MUELLER, B. K., MACK, H. & TEUSCH, N. 2005. Rho kinase, a promising drug target for neurological disorders. *Nat Rev Drug Discov,* 4**,** 387-98.

NADA, S., OKADA, M., MACAULEY, A., COOPER, J. A. & NAKAGAWA, H. 1991. Cloning of a complementary DNA for a protein-tyrosine kinase that specifically phosphorylates a negative regulatory site of p60c-src. *Nature,* 351**,** 69-72.

OHSAWA, K., IMAI, Y., KANAZAWA, H., SASAKI, Y. & KOHSAKA, S. 2000. Involvement of Iba1 in membrane ruffling and phagocytosis of macrophages/microglia. *J Cell Sci,* 113 (Pt 17)**,** 3073-84.

OKUMOTO, S., LOOGER, L. L., MICHEVA, K. D., REIMER, R. J., SMITH, S. J. & FROMMER, W. B. 2005. Detection of glutamate release from neurons by genetically encoded surface-displayed FRET nanosensors. *Proc Natl Acad Sci U S A,* 102**,** 8740-5.

OUYANG, M., SUN, J., CHIEN, S. & WANG, Y. 2008. Determination of hierarchical relationship of Src and Rac at subcellular locations with FRET biosensors. *Proc Natl Acad Sci U S A,* 105**,** 14353-8.

PALOP, J. J., CHIN, J. & MUCKE, L. 2006. A network dysfunction perspective on neurodegenerative diseases. *Nature,* 443**,** 768-73.

PARKHURST, C. N., YANG, G., NINAN, I., SAVAS, J. N., YATES, J. R., 3RD, LAFAILLE, J. J., HEMPSTEAD, B. L., LITTMAN, D. R. & GAN, W. B. 2013. Microglia promote learning-dependent synapse formation through brain-derived neurotrophic factor. *Cell,* 155**,** 1596-609.

PEDERSEN, E. & BRAKEBUSCH, C. 2012. Rho GTPase function in development: how in vivo models change our view. *Exp Cell Res,* 318**,** 1779-87.

PORTUGAL, C. C., SOCODATO, R., CANEDO, T., SILVA, C. M., MARTINS, T., COREIXAS, V. S., LOIOLA, E. C., GESS, B., ROHR, D., SANTIAGO, A. R., YOUNG, P., MINSHALL, R. D., PAES-DE-CARVALHO, R., AMBROSIO, A. F. & RELVAS, J. B. 2017. Caveolin-1-mediated internalization of the vitamin C transporter SVCT2 in microglia triggers an inflammatory phenotype. *Sci Signal,* 10.

PRINZ, M. & PRILLER, J. 2014. Microglia and brain macrophages in the molecular age: from origin to neuropsychiatric disease. *Nat Rev Neurosci,* 15**,** 300-12.

RATTAN, R., GIRI, S., SINGH, A. K. & SINGH, I. 2003. Rho a negatively regulates cytokine-mediated inducible nitric oxide synthase expression in brain-derived transformed cell lines: negative regulation of IKKα. *Free Radical Biology and Medicine,* 35**,** 1037-1050.

RICE, R. A., SPANGENBERG, E. E., YAMATE-MORGAN, H., LEE, R. J., ARORA, R. P., HERNANDEZ, M. X., TENNER, A. J., WEST, B. L. & GREEN, K. N. 2015. Elimination of Microglia Improves Functional Outcomes Following Extensive Neuronal Loss in the Hippocampus. *J Neurosci,* 35**,** 9977-89.

RIDLEY, A. J. 2015. Rho GTPase signalling in cell migration. *Curr Opin Cell Biol,* 36**,** 103-12.

RIENTO, K., GUASCH, R. M., GARG, R., JIN, B. & RIDLEY, A. J. 2003. RhoE binds to ROCK I and inhibits downstream signaling. *Mol Cell Biol,* 23**,** 4219-29.

RIENTO, K. & RIDLEY, A. J. 2003. Rocks: multifunctional kinases in cell behaviour. *Nat Rev Mol Cell Biol,* 4**,** 446-56.

RIGHI, M., MORI, L., DE LIBERO, G., SIRONI, M., BIONDI, A., MANTOVANI, A., DONINI, S. D. & RICCIARDI-CASTAGNOLI, P. 1989. Monokine production by microglial cell clones. *Eur J Immunol,* 19**,** 1443-8.

SCANNEVIN, R. H. & HUGANIR, R. L. 2000. Postsynaptic organization and regulation of excitatory synapses. *Nat Rev Neurosci,* 1**,** 133-41.

SCHULZ, C., GOMEZ PERDIGUERO, E., CHORRO, L., SZABO-ROGERS, H., CAGNARD, N., KIERDORF, K., PRINZ, M., WU, B., JACOBSEN, S. E., POLLARD, J. W., FRAMPTON, J., LIU, K. J. & GEISSMANN, F. 2012. A lineage of myeloid cells independent of Myb and hematopoietic stem cells. *Science,* 336**,** 86-90.

SELLERS, K. J., ELLIOTT, C., JACKSON, J., GHOSH, A., RIBE, E., ROJO, A. I., JAROSZ-GRIFFITHS, H. H., WATSON, I. A., XIA, W., SEMENOV, M., MORIN, P., HOOPER, N. M., PORTER, R., PRESTON, J., AL-SHAWI, R., BAILLIE, G., LOVESTONE, S., CUADRADO, A., HARTE, M., SIMONS, P., SRIVASTAVA, D. P. & KILLICK, R. 2018. Amyloid beta synaptotoxicity is Wnt-PCP dependent and blocked by fasudil. *Alzheimers Dement,* 14**,** 306-317.

SHCHERBAKOVA, D. M., BALOBAN, M., EMELYANOV, A. V., BRENOWITZ, M., GUO, P. & VERKHUSHA, V. V. 2016. Bright monomeric near-infrared fluorescent proteins as tags and biosensors for multiscale imaging. *Nat Commun,* 7**,** 12405.

SILVA, C. S., EIRA, J., RIBEIRO, C. A., OLIVEIRA, A., SOUSA, M. M., CARDOSO, I. & LIZ, M. A. 2017. Transthyretin neuroprotection in Alzheimer's disease is dependent on proteolysis. *Neurobiol Aging,* 59**,** 10-14.

SOCODATO, R., PORTUGAL, C. C., CANEDO, T., DOMITH, I., OLIVEIRA, N. A., PAES-DE-CARVALHO, R., RELVAS, J. B. & COSSENZA, M. 2015a. c-Src deactivation by the polyphenol 3-O-caffeoylquinic acid abrogates reactive oxygen species-mediated glutamate release from microglia and neuronal excitotoxicity. *Free Radic Biol Med,* 79**,** 45-55.

SOCODATO, R., PORTUGAL, C. C., DOMITH, I., OLIVEIRA, N. A., COREIXAS, V. S., LOIOLA, E. C., MARTINS, T., SANTIAGO, A. R., PAES-DE-CARVALHO, R., AMBROSIO, A. F. & RELVAS, J. B. 2015b. c-Src function is necessary and sufficient for triggering microglial cell activation. *Glia,* 63**,** 497-511.

SOCODATO, R., PORTUGAL, C. C., RODRIGUES, A., HENRIQUES, J., RODRIGUES, C., FIGUEIRA, C. & RELVAS, J. B. 2018. Redox tuning of Ca(2+) signaling in microglia drives glutamate release during hypoxia. *Free Radic Biol Med,* 118**,** 137-149.

SOCODATO, R., SANTIAGO, F. N., PORTUGAL, C. C., DOMINGUES, A. F., SANTIAGO, A. R., RELVAS, J. B., AMBRÓSIO, A. F. & PAES-DE-CARVALHO, R. 2012. Calcium-permeable AMPA Receptors trigger neuronal NOS activation to promote nerve cell death in an Src kinase-dependent fashion. *J Biol Chem***,** in press.

SPANGENBERG, E. E., LEE, R. J., NAJAFI, A. R., RICE, R. A., ELMORE, M. R., BLURTON-JONES, M., WEST, B. L. & GREEN, K. N. 2016. Eliminating microglia in Alzheimer's mice prevents neuronal loss without modulating amyloid-beta pathology. *Brain,* 139**,** 1265-81.

STANKIEWICZ, T. R. & LINSEMAN, D. A. 2014. Rho family GTPases: key players in neuronal development, neuronal survival, and neurodegeneration. *Front Cell Neurosci,* 8**,** 314.

TAKEUCHI, H., JIN, S., WANG, J., ZHANG, G., KAWANOKUCHI, J., KUNO, R., SONOBE, Y., MIZUNO, T. & SUZUMURA, A. 2006. Tumor necrosis factor-alpha induces neurotoxicity via glutamate release from hemichannels of activated microglia in an autocrine manner. *J Biol Chem,* 281**,** 21362-8.

TAKEUCHI, H., MIZOGUCHI, H., DOI, Y., JIN, S., NODA, M., LIANG, J., LI, H., ZHOU, Y., MORI, R., YASUOKA, S., LI, E., PARAJULI, B., KAWANOKUCHI, J., SONOBE, Y., SATO, J., YAMANAKA, K., SOBUE, G., MIZUNO, T. & SUZUMURA, A. 2011. Blockade of gap junction hemichannel suppresses disease progression in mouse models of amyotrophic lateral sclerosis and Alzheimer's disease. *PLoS One,* 6**,** e21108.

TAY, T. L., MAI, D., DAUTZENBERG, J., FERNANDEZ-KLETT, F., LIN, G., SAGAR, DATTA, M., DROUGARD, A., STEMPFL, T., ARDURA-FABREGAT, A., STASZEWSKI, O., MARGINEANU, A., SPORBERT, A., STEINMETZ, L. M., POSPISILIK, J. A., JUNG, S., PRILLER, J., GRUN, D., RONNEBERGER, O. & PRINZ, M. 2017. A new fate mapping system reveals context-dependent random or clonal expansion of microglia. *Nat Neurosci,* 20**,** 793-803.

THOMAS, R. M., SCHMEDT, C., NOVELLI, M., CHOI, B. K., SKOK, J., TARAKHOVSKY, A. & ROES, J. 2004. C-terminal SRC kinase controls acute inflammation and granulocyte adhesion. *Immunity,* 20**,** 181-91.

VENTURA, A., MEISSNER, A., DILLON, C. P., MCMANUS, M., SHARP, P. A., VAN PARIJS, L., JAENISCH, R. & JACKS, T. 2004. Cre-lox-regulated conditional RNA interference from transgenes. *Proc Natl Acad Sci U S A,* 101**,** 10380-5.

VIGIL, D. & DER, C. J. 2013. Inhibitors of the ROCK serine/threonine kinases: key effectors of the RhoA small GTPase. *Enzymes,* 33 Pt A**,** 193-212.

WALSH, D. M. & SELKOE, D. J. 2007. A beta oligomers - a decade of discovery. *J Neurochem,* 101**,** 1172-84.

WANG, L. & ZHENG, Y. 2007. Cell type-specific functions of Rho GTPases revealed by gene targeting in mice. *Trends Cell Biol,* 17**,** 58-64.

WANG, Y., CELLA, M., MALLINSON, K., ULRICH, J. D., YOUNG, K. L., ROBINETTE, M. L., GILFILLAN, S., KRISHNAN, G. M., SUDHAKAR, S., ZINSELMEYER, B. H., HOLTZMAN, D. M., CIRRITO, J. R. & COLONNA, M. 2015. TREM2 lipid sensing sustains the microglial response in an Alzheimer's disease model. *Cell,* 160**,** 1061-71.

WANG, Y., ULLAND, T. K., ULRICH, J. D., SONG, W., TZAFERIS, J. A., HOLE, J. T., YUAN, P., MAHAN, T. E., SHI, Y., GILFILLAN, S., CELLA, M., GRUTZENDLER, J., DEMATTOS, R. B., CIRRITO, J. R., HOLTZMAN, D. M. & COLONNA, M. 2016. TREM2-mediated early microglial response limits diffusion and toxicity of amyloid plaques. *J Exp Med,* 213**,** 667-75.

WEN, J., RIBEIRO, R. & ZHANG, Y. 2011. Specific PKC isoforms regulate LPS-stimulated iNOS induction in murine microglial cells. *J Neuroinflammation,* 8**,** 38.

WHEELER, A. P. & RIDLEY, A. J. 2004. Why three Rho proteins? RhoA, RhoB, RhoC, and cell motility. *Exp Cell Res,* 301**,** 43-9.

YONA, S., KIM, K. W., WOLF, Y., MILDNER, A., VAROL, D., BREKER, M., STRAUSS-AYALI, D., VIUKOV, S., GUILLIAMS, M., MISHARIN, A., HUME, D. A., PERLMAN, H., MALISSEN, B., ZELZER, E. & JUNG, S. 2013. Fate mapping reveals origins and dynamics of monocytes and tissue macrophages under homeostasis. *Immunity,* 38**,** 79-91.

YOSHIZAKI, H., OHBA, Y., KUROKAWA, K., ITOH, R. E., NAKAMURA, T., MOCHIZUKI, N., NAGASHIMA, K. & MATSUDA, M. 2003. Activity of Rho-family GTPases during cell division as visualized with FRET-based probes. *J Cell Biol,* 162**,** 223-32.

YU, Z., CHENG, G., WEN, X., WU, G. D., LEE, W. T. & PLEASURE, D. 2002. Tumor necrosis factor alpha increases neuronal vulnerability to excitotoxic necrosis by inducing expression of the AMPA-glutamate receptor subunit GluR1 via an acid sphingomyelinase- and NF-kappaB-dependent mechanism. *Neurobiol Dis,* 11**,** 199-213.

ZHOU, X. & ZHENG, Y. 2013. Cell type-specific signaling function of RhoA GTPase: lessons from mouse gene targeting. *J Biol Chem,* 288**,** 36179-88.

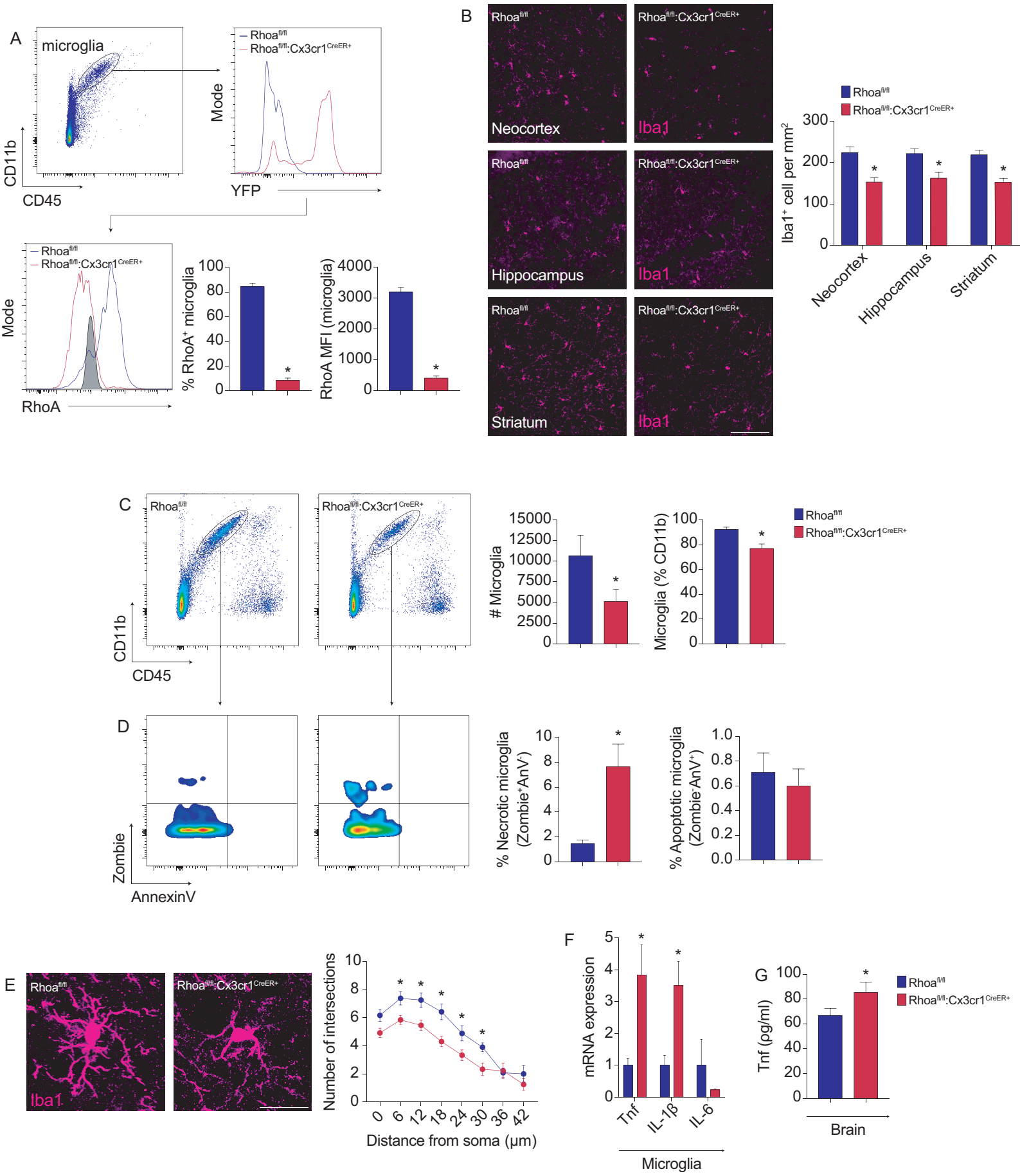
A
microglia
CD11b
CD45
Rhoa fl/fl
Rhoa fl/fl:Cx3cr1 CreER+
Mode
YFP
RhoA
% RhoA+ microglia
RhoA MFI (microglia)
B
Rhoa fl/fl
Rhoa fl/fl:Cx3cr1 CreER+
Neocortex
Hippocampus
Striatum
Iba1
Iba1+ cell per mm2
C
Microglia
Microglia (% CD11b)
D
Zombie
AnnexinV
% Necrotic microglia (Zombie+AnV+)
% Apoptotic microglia (Zombie-AnV+)
E
Number of intersections
Distance from soma (µm)
F
mRNA expression
Tnf
IL-1β
IL-6
Microglia
G
Tnf (pg/ml)
Brain

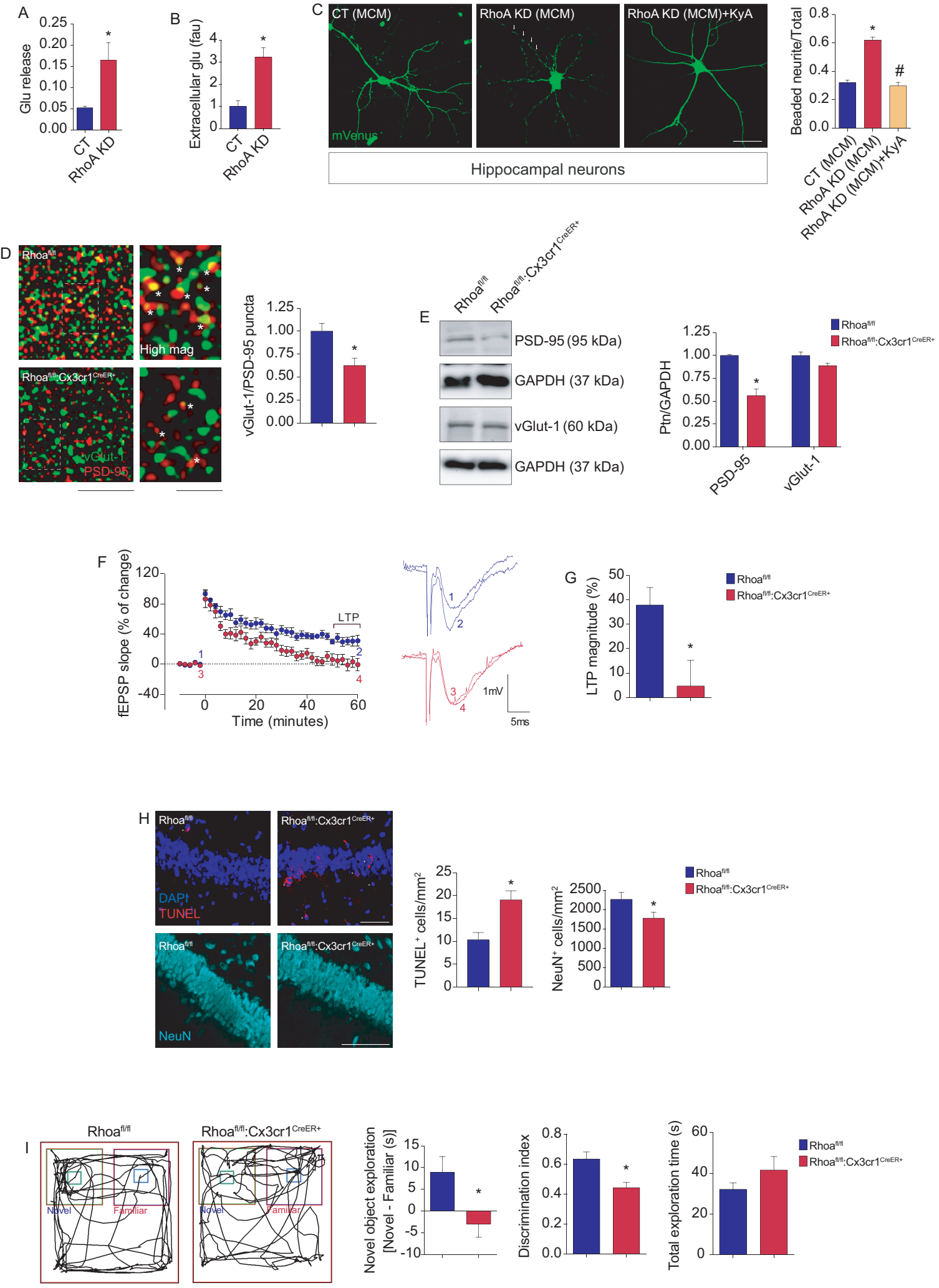
A
Glu release
CT
RhoA KD
B
Extracellular glu (fau)
CT
RhoA KD
C
CT (MCM)
RhoA KD (MCM)
RhoA KD (MCM)+KyA
mVenus
Hippocampal neurons
Beaded neurite/Total
CT (MCM)
RhoA KD (MCM)
RhoA KD (MCM)+KyA
D
Rhoa fl/fl
High mag
Rhoa fl/fl:Cx3cr1 CreER+
vGlut-1
PSD-95
vGlut-1/PSD-95 puncta
E
Rhoa fl/fl
Rhoa fl/fl:Cx3cr1 CreER+
PSD-95 (95 kDa)
GAPDH (37 kDa)
vGlut-1 (60 kDa)
GAPDH (37 kDa)
Ptn/GAPDH
PSD-95
vGlut-1
F
fEPSP slope (% of change)
LTP
Time (minutes)
1mV
5ms
G
LTP magnitude (%)
H
DAPI
TUNEL
NeuN
TUNEL+ cells/mm2
NeuN+ cells/mm2
I
Novel
Familiar
Novel object exploration [Novel - Familiar (s)]
Discrimination index
Total exploration time (s)

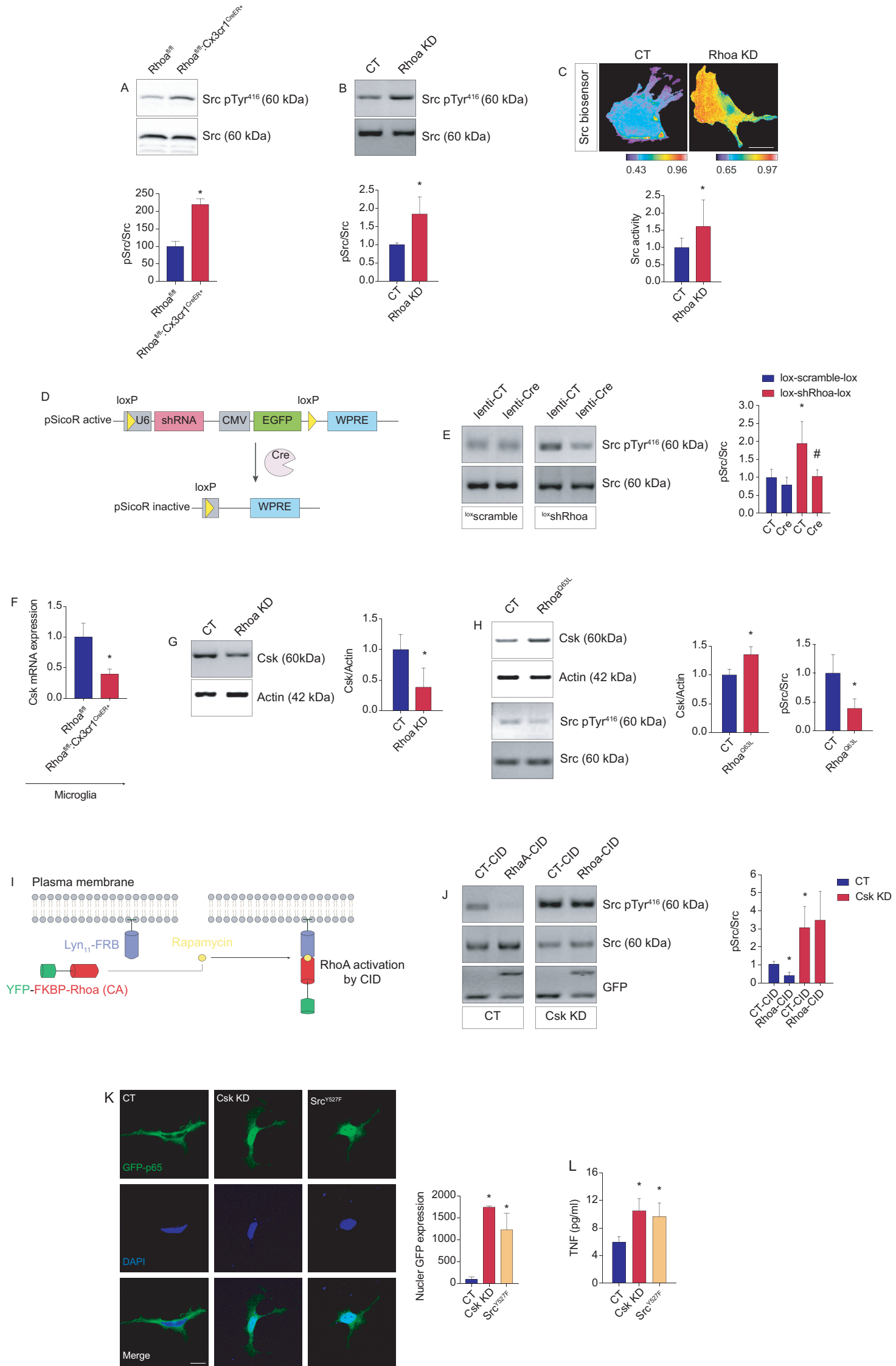
A
Rhoa fl/fl
Rhoa fl/fl:Cx3cr1 CreER+
Src pTyr416 (60 kDa)
Src (60 kDa)
pSrc/Src
B
CT
Rhoa KD
C
Src biosensor
0.43
0.96
0.65
0.97
Src activity
D
loxP
pSicoR active
U6
shRNA
CMV
EGFP
WPRE
Cre
pSicoR inactive
E
lenti-CT
lenti-Cre
loxscramble
loxshRhoa
lox-scramble-lox
lox-shRhoa-lox
F
Csk mRNA expression
Microglia
G
Csk (60kDa)
Actin (42 kDa)
Csk/Actin
H
RhoaQ63L
I
Plasma membrane
Lyn11-FRB
Rapamycin
YFP-FKBP-Rhoa (CA)
RhoA activation by CID
J
CT-CID
RhaA-CID
Rhoa-CID
Csk KD
GFP
K
Csk KD
SrcY527F
GFP-p65
DAPI
Merge
Nucler GFP expression
L
TNF (pg/ml)

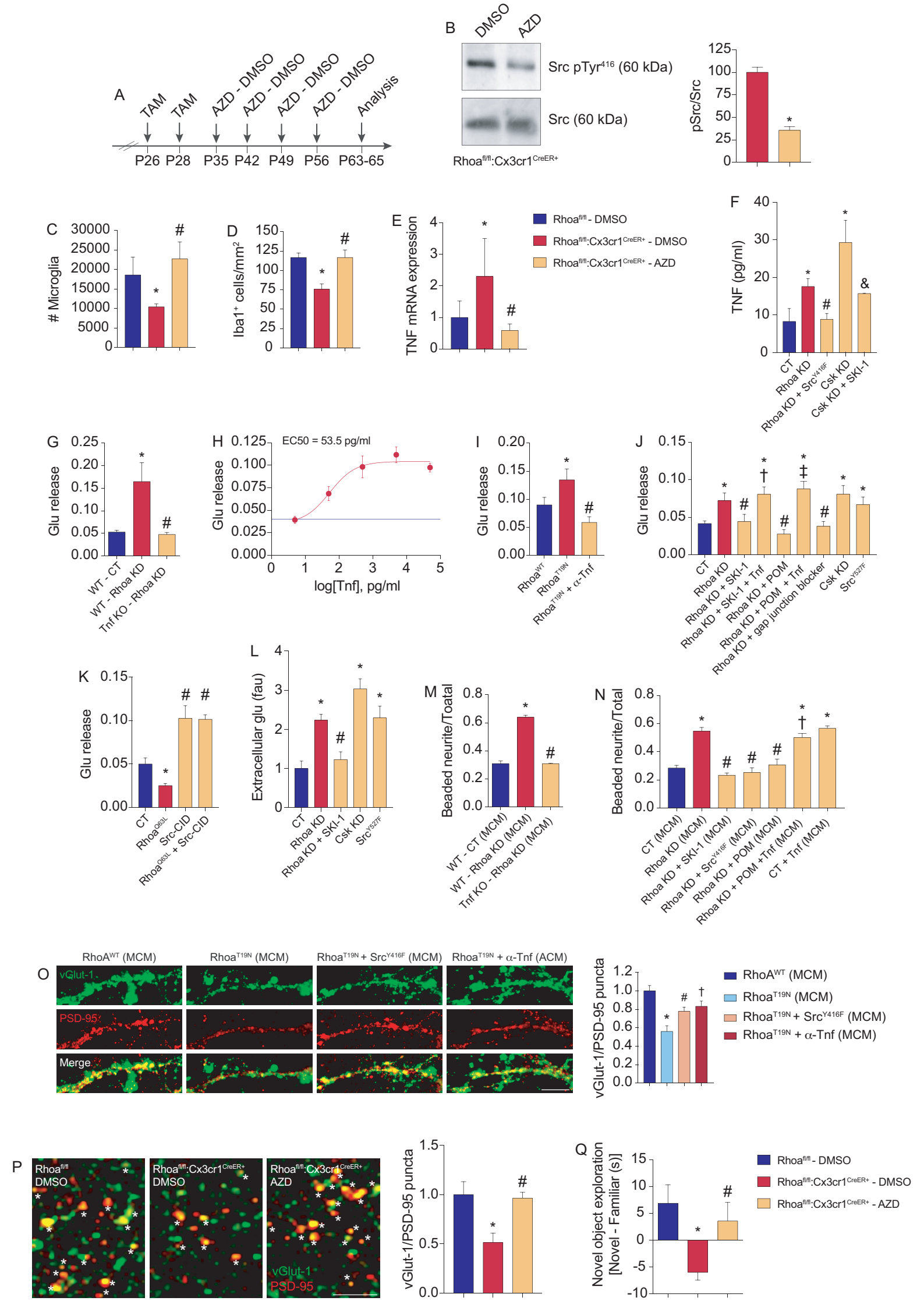
A
TAM
TAM
AZD - DMSO
AZD - DMSO
AZD - DMSO
AZD - DMSO
Analysis
P26 P28 P35 P42 P49 P56 P63-65
B
DMSO
AZD
Src pTyr416 (60 kDa)
Src (60 kDa)
Rhoafl/fl:Cx3cr1CreER+
pSrc/Src
C
Microglia
D
Iba1+ cells/mm2
E
TNF mRNA expression
Rhoafl/fl - DMSO
Rhoafl/fl:Cx3cr1CreER+ - DMSO
Rhoafl/fl:Cx3cr1CreER+ - AZD
F
TNF (pg/ml)
CT
Rhoa KD
Rhoa KD + SrcY416F
Csk KD
Csk KD + SKI-1
G
Glu release
WT - CT
WT - Rhoa KD
Tnf KO - Rhoa KD
H
EC50 = 53.5 pg/ml
Glu release
log[Tnf], pg/ml
I
Glu release
RhoaWT
RhoaT19N
RhoaT19N + α-Tnf
J
Glu release
CT
Rhoa KD
Rhoa KD + SKI-1
Rhoa KD + SKI-1 + Tnf
Rhoa KD + POM
Rhoa KD + POM + Tnf
Rhoa KD + gap junction blocker
Csk KD
SrcY527F
K
Glu release
CT
RhoaQ63L
Src-CID
RhoaQ63L + Src-CID
L
Extracellular glu (fau)
CT
Rhoa KD
Rhoa KD + SKI-1
Csk KD
SrcY527F
M
Beaded neurite/Toatal
WT - CT (MCM)
WT - Rhoa KD (MCM)
Tnf KO - Rhoa KD (MCM)
N
Beaded neurite/Total
CT (MCM)
Rhoa KD (MCM)
Rhoa KD + SKI-1 (MCM)
Rhoa KD + SrcY416F (MCM)
Rhoa KD + POM (MCM)
Rhoa KD + POM +Tnf (MCM)
CT + Tnf (MCM)
O
RhoAWT (MCM)
RhoaT19N (MCM)
RhoaT19N + SrcY416F (MCM)
RhoaT19N + α-Tnf (ACM)
vGlut-1
PSD-95
Merge
vGlut-1/PSD-95 puncta
RhoAWT (MCM)
RhoaT19N (MCM)
RhoaT19N + SrcY416F (MCM)
RhoaT19N + α-Tnf (MCM)
P
Rhoafl/fl
DMSO
Rhoafl/fl:Cx3cr1CreER+
DMSO
Rhoafl/fl:Cx3cr1CreER+
AZD
vGlut-1
PSD-95
vGlut-1/PSD-95 puncta
Q
Novel object exploration
[Novel - Familiar (s)]
Rhoafl/fl - DMSO
Rhoafl/fl:Cx3cr1CreER+ - DMSO
Rhoafl/fl:Cx3cr1CreER+ - AZD

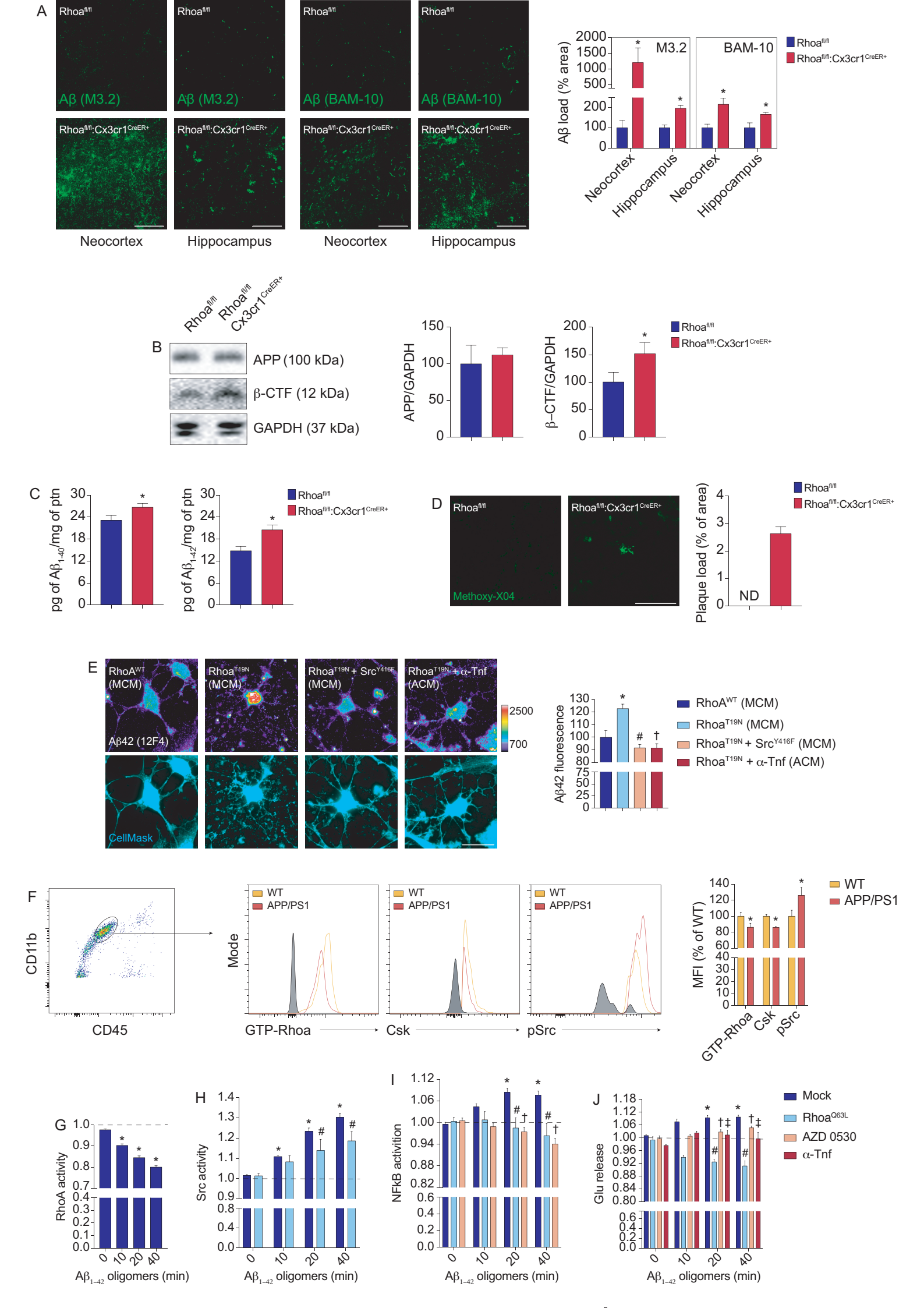
A
Rhoa fl/fl
Aβ (M3.2)
Aβ (BAM-10)
Rhoa fl/fl:Cx3cr1 CreER+
Neocortex
Hippocampus
Aβ load (% area)
M3.2
BAM-10
B
Rhoa fl/fl
Rhoa fl/fl Cx3cr1 CreER+
APP (100 kDa)
β-CTF (12 kDa)
GAPDH (37 kDa)
APP/GAPDH
β–CTF/GAPDH
C
pg of Aβ1-40/mg of ptn
pg of Aβ1-42/mg of ptn
D
Methoxy-X04
Plaque load (% of area)
ND
E
RhoA WT (MCM)
Rhoa T19N (MCM)
Rhoa T19N + Src Y416F (MCM)
Rhoa T19N + α-Tnf (ACM)
Aβ42 (12F4)
CellMask
Aβ42 fluorescence
RhoA WT (MCM)
Rhoa T19N (MCM)
Rhoa T19N + Src Y416F (MCM)
Rhoa T19N + α-Tnf (ACM)
F
CD11b
CD45
WT
APP/PS1
Mode
GTP-Rhoa
Csk
pSrc
MFI (% of WT)
G
RhoA activity
H
Src activity
I
NFkB activition
J
Glu release
Mock
Rhoa Q63L
AZD 0530
α-Tnf
Aβ1–42 oligomers (min)

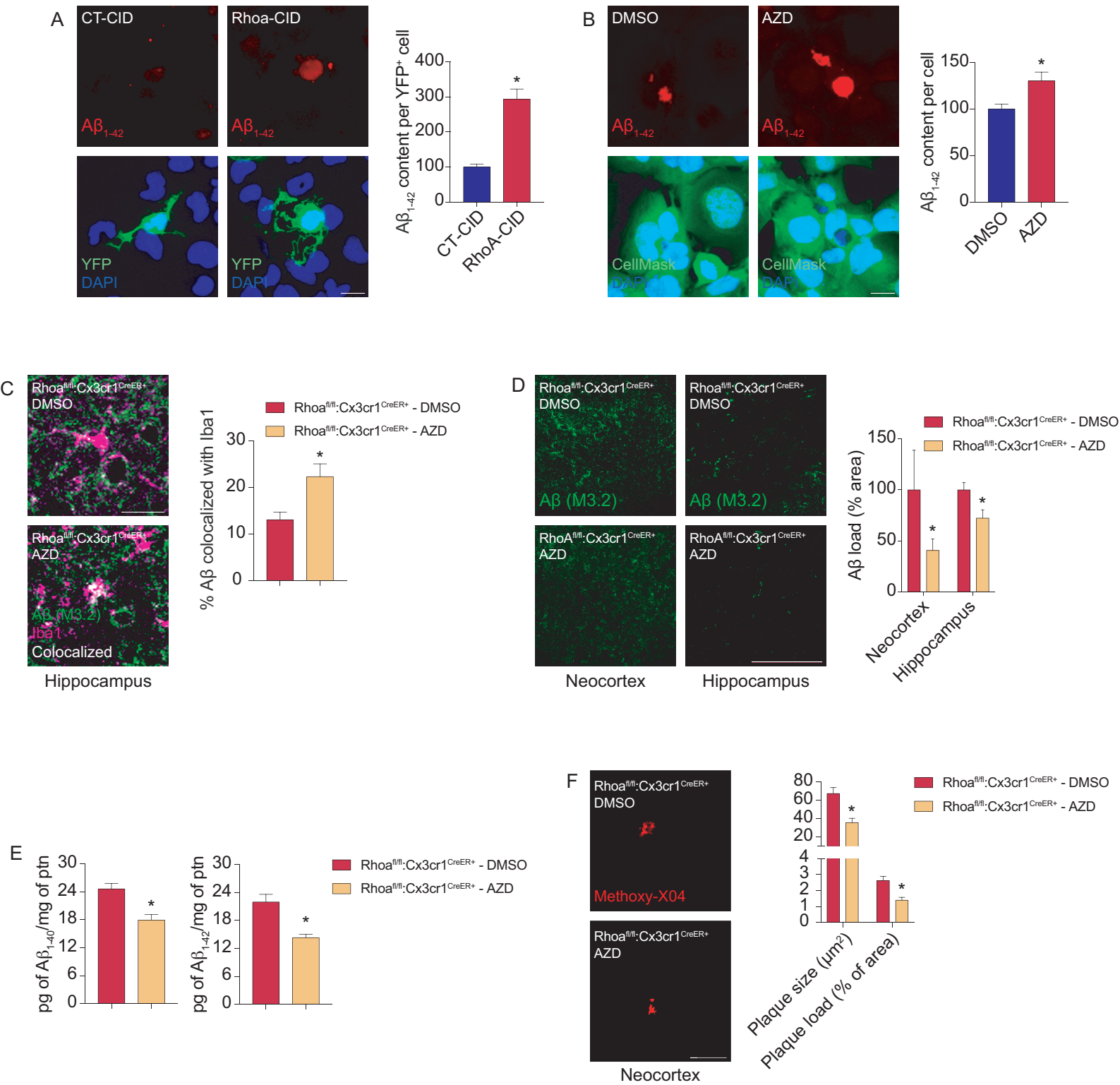
A
CT-CID
Rhoa-CID
Aβ1-42
YFP
DAPI
Aβ1-42 content per YFP+ cell
400
300
200
100
0
CT-CID
RhoA-CID
B
DMSO
AZD
CellMask
DAPI
Aβ1-42 content per cell
150
100
50
C
Rhoafl/fl:Cx3cr1CreER+
DMSO
AZD
Aβ (M3.2)
Iba1
Colocalized
Hippocampus
% Aβ colocalized with Iba1
30
20
10
Rhoafl/fl:Cx3cr1CreER+ - DMSO
Rhoafl/fl:Cx3cr1CreER+ - AZD
D
RhoAfl/fl:Cx3cr1CreER+
Neocortex
Aβ load (% area)
Plaque size (μm2)
Plaque load (% of area)
E
pg of Aβ1-40/mg of ptn
pg of Aβ1-42/mg of ptn
F
Methoxy-X04